HIGH FORCE MAGNETIC TWEEZERS FOR MOLECULAR MANIPULATION INSIDE LIVING CELLS

Anthony de Vries

De promotiecommissie:

Prof. dr. ir. A. Bliek	Universiteit Twente, voorzitter
Prof. dr. J. Greve	Universiteit Twente, promoter
dr.ir. J.S. Kanger	Universiteit Twente
prof.dr. V. Subramaniam	Universiteit Twente
prof.dr. C.G. Figdor	Universiteit Twente
prof.dr. G. Reiss	Universität Bielefeld
prof.dr. M.J. Peters	Universiteit Twente
prof.dr. R. van Driel	Universiteit van Amsterdam

Acknowledgement

This research was financially supported by NWO Earth and Life Sciences. It was performed in collaboration with the Swammerdam Institute for Life Sciences, University of Amsterdam.

ISBN 90-9018799-5

HIGH FORCE MAGNETIC TWEEZERS FOR MOLECULAR MANIPULATION INSIDE LIVING CELLS

PROEFSCHRIFT

ter verkrijging van
de graad van doctor aan de Universiteit Twente,
op gezag van de rector magnificus,
prof. dr. F.A. van Vught,
volgens besluit van het College voor Promoties
in het openbaar te verdedigen
op woensdag 10 november 2004 om 15.00 uur

door

Anthony Henk Bernard de Vries

geboren op 26 mei 1972

te Gent, België

Dit proefschrift is goedgekeurd door

De promoter:	prof. dr. J. Greve
De assistent promotor:	dr. ir. J.S. Kanger

To my family

Contents

1. Introduction

1.1. Biological background

Living cells form a very interesting, but also very challenging research subject for biologists and biophysicists. Cells are the building blocks of all organisms, and we have long come to the stage that better understanding of the functioning of the organism as a whole, requires detailed knowledge of the internal molecular processes of the cells that compose it.

It has become clear that cells are extremely complex systems, composed of a multitude of organelles with specific functions. Examples of these organelles are the nucleus, containing the genetic material in the form of chromatin and regulating gene expression, the mitochondria producing the chemical energy for the cell, and the endoplasmic reticulum and Golgi apparatus that are involved in

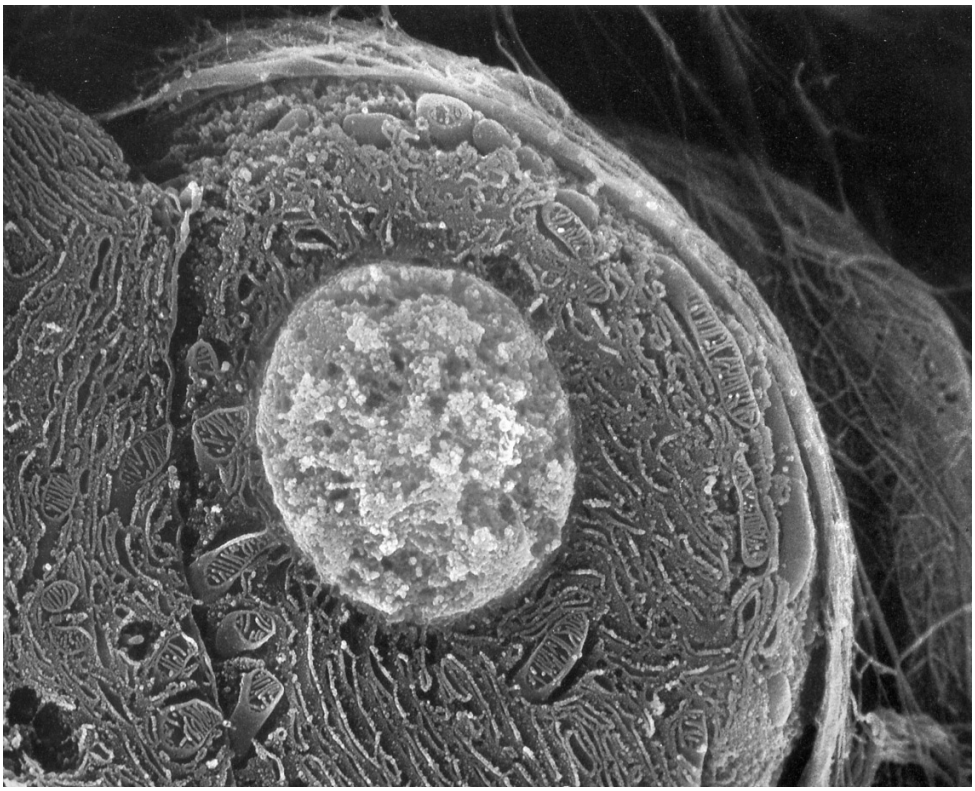

Figure 1.1 Electron micrograph of a lymph node cell [1]. The cell has a diameter of 14 μm. Clearly visible are the nucleus and numerous mitochondria.

processes like protein synthesis and transportation. (See Figure 1.1; produced by [1]) All organelles are embedded in the cytoplasm. There a cytoskeleton gives structural support to the cell, but also facilitates intracellular transport, and movement of (parts of) the cell as a whole. The cell can perform amazingly complex transformations like cell division (meiosis and mitosis) where chromosomes are condensed, aligned and in the case of meiosis paired up with their counterpart, and pulled apart so as to equally divide them between the two new cells.
All of these systems and processes are governed by intracellular molecular interactions. Detailed knowledge of these interactions is therefore essential for understanding how the cell functions, both in the normal and in the pathological state. The latter will also facilitate the rational design of drugs and therapies for a multitude of diseases.

The problem however, is that there are no suitable methods for doing spatially resolved measurements with molecular resolution that are fit to study these molecular interactions directly within a living cell. Therefore, one is forced to use model systems to try to gain more understanding of these molecular processes.

Single molecule techniques like optical tweezers [2] and atomic force microscopy [3] have been used extensively to study these model systems, by carefully manipulating the positioning of the molecules, and/or exerting forces on molecular constructs. Using these techniques for example the velocity at which an RNA polymerase transcribes a piece of DNA, and the force necessary to stall this process have been determined [4,5]. Also assembly and unravelling of DNA nucleosomes [6,7] and kinesin movement along microtubules [8] have been studied.

These experiments have produced amazing results, but one has to take into account that all of them were obtained in-vitro in very simple environments. It is unclear if the acquired results are still valid or relevant in the complex environment inside the cell. Furthermore, most organelles and cellular processes are so complex that it is simply impossible to create model systems for them. It is therefore inevitable that future experiments have to take place inside the living cells themselves.

In this thesis we take a first step towards the development of methods and instrumentation to start probing the inside of a single living cell, with the goal to eventually be able to perform single molecule experiments, like the ones described above, inside the cell itself. Doing such single molecule experiments however, is a goal that lies very far in the future. For now, we will concentrate on

probing larger structures, namely the structural properties of the cytoskeleton and the inside of the nucleus, by exerting force on it using a small probe.

The cytoskeleton is an extremely dynamic structure that plays a major role in many cellular processes. There is data about the viscoelastic properties of the skeleton, but the results vary as wildly as the techniques used to measure it. Using in vivo manipulation of the probe, we will try to determine unknown quantities like the homogeneity and isotropism of the viscoelastic properties of the cytoskeleton while embedded in the cytoplasm.
Trying to enter the nucleus, we will venture into unknown country. It is astonishing that practically nothing is known about structural properties of the nucleus, while at the same time it is assumed that it plays a major role in gene regulation, and is thus of extremely high interest to current cell research. This is probably the best illustration of the need for the in vivo manipulation tool we are going to develop.

1.2. Demands on in vivo nano-manipulation:

We will focus on building an instrument that can perform in vivo nano-manipulation. To this end a probe, on which forces can be applied, will have to be introduced into the cell. The techniques that may be used in an in vivo nano-manipulation instrument should ideally comply with the following set of criteria:
Suitable for living cells, causing no or very limited cell damage, so that the cell stays alive.

- Very small probe comparable in size to the organelles or complexes to be studied, to be able to localize manipulation on the molecules or organelles.
- Force exertion should be exclusively on the probe, so that the environment (the cell) is affected as little as possible.
- Ability to exert *directed* forces in 3D.
- Force amplitude in the biological relevant pico-Newton regime
- Detection of the position or displacement of probes and targets at nanometre accuracy.
- Probe surface should be easy to modify allowing the study of specific molecular interactions.

Using this set of criteria, the possible techniques for nano-manipulation will be discussed in the next section, so that a choice for one of them can be made.

1.3. Exerting force on a probe

Clearly the most important feature of an in vivo nano-manipulator is that it can exert a force on a probe. The choice of a force transduction mechanism is limited to optical, mechanical, electrical, or magnetic means.

Optical force is used in optical tweezers [2] that can capture beads in a strongly focussed laser beam. Optical tweezers can produce quite high forces (10-100 pN), but only with relatively large beads (>1μm) and at very high laser power (~1W). The method also allows for nanometre accurate bead position detection, by measuring the deflection of the laser beam caused by the bead. For intracellular work, optical tweezers have a definite disadvantage that they are not very selective. The size of the optical tweezers is governed by optical diffraction, usually giving a measuring volume of 0.2 μm^3. Optical tweezers will trap anything with a refractive index that is different from the environment, meaning that in a cell it will also trap organelles and even molecules. This problem becomes worse for smaller beads and higher powers, as the difference between bead and organelle diminishes.

Systems using mechanical forces like the AFM or micropipettes can produce very high forces, easily in the nN range. But the recurring problem is how to get the system into the cell. In any scenario, during application of force a needle of some sort is penetrating into the cell up to several micrometres. The applied force using such a needle is of course not limited to the tip. The complete surface area of the needle that is in contact with the cell will apply a (shear) force.

Potentially also an electrical force could be used. This technique has been used to manipulate complete cells, by a process called dielectropheresis [9]. The biggest problem in using electric forces is the selectivity. The whole cell is filled with electrically charged molecules and organelles. That is the reason why electrical forces can be used to manipulate complete cells, but at the same time it also leads to severe limitations in the use for exerting force on a small probe at a specific location.

Using magnetism currently allows for exerting high force on ferromagnetic probes (nN on μm size beads). More importantly magnetic force transduction is extremely selective for the probe, as cells have very little (ferro)magnetic content. Also magnetic fields do not seriously harm cells.

Table 1.1 gives an approximate indication of the advantages and disadvantage of the different techniques of exerting force, relative to each other. Choosing from the possible techniques, the use of magnetic forces clearly has the most potential,

especially when using very small probes. In the next section, the use of magnetic forces for manipulation will be further investigated.

Table 1.1 Advantages of the different force transduction mechanisms for use inside living cells.

	Probe size	Force	Selectivity	Detection	Cell damage
Optical	-	+	-	++	-
Mechanical	-	++	--	+	--
Electrical	-	-	--	-	--
Magnetic	+	+	++	-	+

1.4. Magnetic Tweezers

Instruments using magnetic forces for manipulation are generally called magnetic tweezers, even though for most of them the term 'tweezers' is a bit of a misnomer, as they cannot hold a particle at a specific location. Looking in detail at the current magnetic tweezers that are used, they can be divided into three groups based of the configuration of the magnetic poles:

- Single magnetic poles, meant for exerting a magnetic force in one direction.
- Multiple poles, typically four to eight magnetic poles, designed to exert force in multiple directions.
- Dual poles, designed to exert magnetic torque, but very little force.

Magnetic tweezers that have been used for exerting force in cells are all single pole systems that can only exert force in one direction [10]. These systems have achieved very high magnetic force on the magnetic probe, but because this force is exerted in one direction, true manipulation of the probe would only be possible by rotating the cell in respect to the magnetic pole. (This has not been done).
A handful of multi-pole tweezers exist that can also exert force in multiple directions [11]. These manipulators however are extremely weak, even when using very large beads (5 μm), and thus useless for intra-cellular manipulation.
The third group of magnetic tweezers are typically used in in-vitro single molecule research. Their main function is not to exert a magnetic force, but to exert magnetic *torque*. Because of the capability to rotate magnetic beads, these systems are typically used for research on super-coiling of DNA and related proteins [12].

A pair of magnetic tweezers capable of doing in vivo nano-manipulation will need to combine the high forces on small beads needed for intracellular work, with the possibility of changing the amplitude and direction of the magnetic force to allow complete manipulation.

1.5. Current status of cellular manipulation

Current cell nano-manipulation can be split up into experiments done in the cell cytoplasm, where a probe is inserted into the cell itself, and experiments on the cell membrane, where the probe is located outside the cell. No manipulation experiments have been performed on material inside the nucleus (except for laser microirradiation [13])

Cell membrane

Optical Tweezers have typically been used for tracking and manipulating of molecules embedded in the cell membrane. A micrometre sized bead is held in the optical tweezers outside the cell. It is coupled directly, or with the use of a (DNA) spacer to the molecule of interest in the membrane. In this way either forces can be applied onto the molecule, or its diffusion through the membrane can be followed [14]. When the cells are very thin, then also atomic force microscopy can be used. The outer membrane can then be imaged, but also the stiffness of the membrane and the structures directly underneath can be probed, yielding partial information of the cell interior. [15,16]

Cytoplasm

Micropipettes have been used to measure forces applied to chromosomes when they are aligned in the cell during metaphase. To this end, a small micropipette was poked into the cell, and used to move chromosomes (Figure 1.2). From measuring deflection of the needle and/or chromosomes, force information can be extracted. [17] The disadvantage of this method is clearly that the pipette is still quite big, and thus will influence much more than just the targeted chromosome.

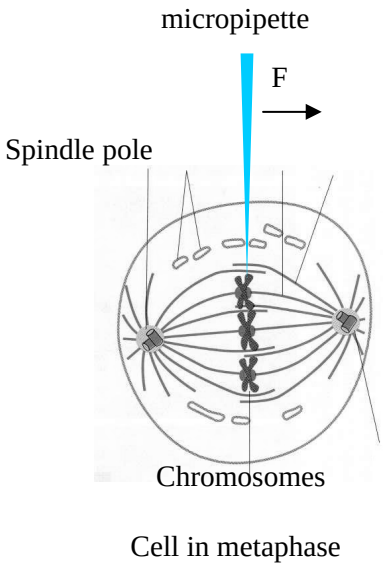

Figure 1.2 Use of micropipettes for micro manipulation

Optical tweezers have been used for intracellular experiments, where injected beads of 1 and 3 µm diameter have been oscillated by the trap, and their response monitored yielding information about the mechanical properties of the environment around the bead [18].

It is not always necessary to apply a force to yield information of the interior of the cell. In stead of applying a force as shown in the optical tweezers experiment described above,

one can also use the Brownian motion of particles itself. Although no specific manipulation is performed, it has the advantage that very small particles can be used. This heat driven spontaneous movement is influenced by the surrounding medium. Monitoring of the diffusion of such particles thus yield structural information about the environment [19].

As already indicated earlier, magnetic tweezers have been used successfully for exerting forces on probes in the cell interior. These tweezers are able to achieve high forces on probes located deep inside the cell, while being very selective for the probe. Experiments using this technique have focussed on measuring the viscoelastic properties of the cell cytoplasm [10,20,21]. Because the magnetic tweezers that have been used for these experiments can only pull in one direction, they can however not be used for controlled manipulation

None of the current manipulation methods in use today complies on sufficient points with the criteria listed, and thus a new instrument has to be developed, which was the goal of this thesis.

1.6. Goal of this thesis

In this thesis magnetic tweezers suitable for nano-manipulation inside living cells will be developed. The thesis needs to provide a proof-of-principle for doing in vivo manipulation. Questions to be answered are how the magnetic field should be generated, and which configuration is best suited for the instrument. The theoretical and practical limitations concerning the achievable force related to the size of the probe will have to be investigated to predict how far this technique can be further developed. Ultimately, the system will have to be tested by actually performing magnetic manipulation inside living cells.

The magnetic tweezers in vivo nano-manipulator that will be developed needs to combine the high forces on small beads needed for intracellular work, with the possibility of changing the amplitude and direction of the magnetic force to allow complete manipulation. It will be shown in chapter 2 that this requires a microscopic multi-pole magnetic system, between which the cell is positioned, as shown in (Figure 1.3)

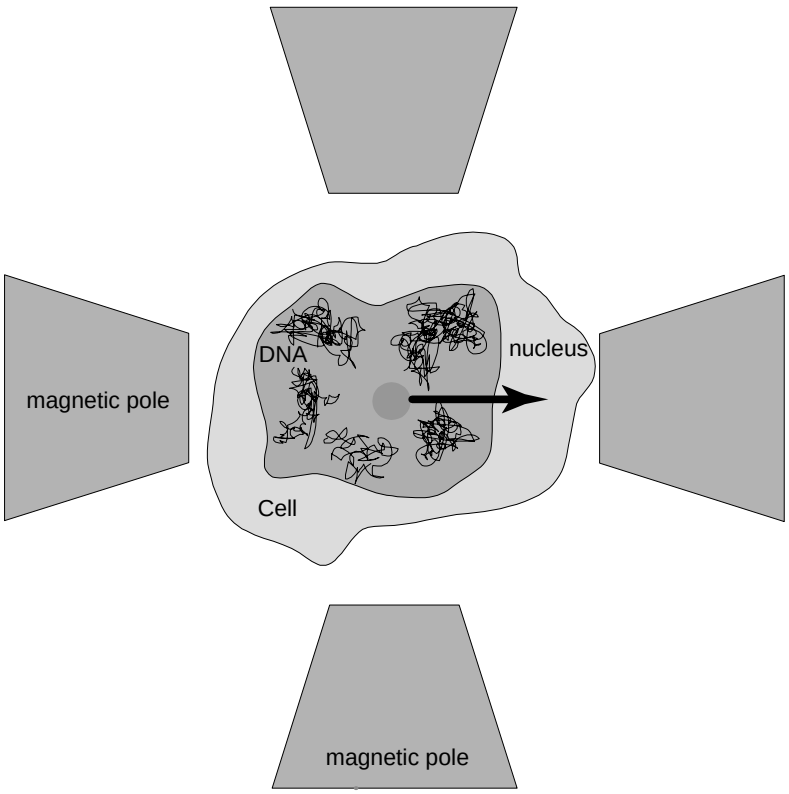

Figure 1.3 approximate concept of in-vivo magnetic tweezers; a cell is placed between multiple poles allowing to exert high directed magnetic forces on a magnetic bead inserted into the cell nucleus.

1.7. Outline

In the following chapters, the development of the magnetic tweezers will be described. First, in chapter 2 the theory behind the magnetic tweezers is discussed. The magnetic configuration of the tweezers is described, and predictions are made on the achievable forces. Chapter 3 then describes in detail how the magnetic tweezers that were designed are produced. Unexpectedly, the actual fabrication of the tweezers turned out to be one of the biggest challenges in this project! Chapter 4 then characterizes the resulting magnetic tweezers, and compares the achieved force to the theoretical one derived in chapter 2. In Chapter 5, the magnetic tweezers is put to the test, by performing manipulation experiments inside living cells.
In the last chapter, conclusions are drawn about the instrument, how it may be improved, and how much potential this system has for the future.

1.8. References

1 L. Nilsson, 1992, **Scientific Europe** pag. 393. *Foundation Scientific Europe, Maastricht, Netherlands. ISBN 90-73035-06-6/CIP*.

2 K. Svoboda, C.F. Schmidt, B.J. Schnapp, S.M. Block, 1993,**Direct Observation Of Kinesin Stepping By Optical Trapping Interferometry**, *Nature*, 365, 721-727

3 M.B. Viani, T.E. Schaffer, A. Chand, M. Rief, H.E. Gaub, P.K. Hansma, 1999, **Small cantilevers for force spectroscopy of single molecules**, *J. Appl. Phys*, 86, 2258-2262.

4 R.J.Ravenport, G.J.L.Wuite, R.Landick, C.Bustamente, **Single Molecule Study of Transcriptional pausing and arrest by E.Coli RNA polymerase**, *Science*, 287, p.2497-2500

5 M.D. Wang, M.J. Schnitzer, H. Yin, R. Landick, S.M. Block, **Force and velocity measured for single molecule of RNA polymerase,** *Science*, 282:902-907

6 M.L. Bennink, L.H. Pope, S.H. Leuba, B.G. de Grooth, J.Greve, 2001. **Single Chromatin Fibre Assembly Using Optical Tweezers**. *Single molecules*, 2, 91-97

7 M.L. Bennink, S.H. Leuba, G. Leno, J. Zlatanova, B.G. de Grooth, J.Greve. 2001. **Unfolding individual nucleosomes by stretching single chromatin fibers with optical tweezers**. *Nature structural biology*, 8(7), 606-610

8 J.Howard, A.J. Hudspeth, R.D. Vale, 1989, **Movement Of Microtubules By Single Kinesin Molecules**, *Nature*, 342, 154-158

9 H. Morgan, M.P. Hughes, N.G. Green, **Separation of submicron particles by dielectropheresis**, *Biophysical Journal*, 77:516

10 W. Feneberg, M. Westphal, E. Sackmann. 2001 **Dictyostelium cells' cytoplasm as an active viscoplastic body** *European Biophysics Journal with Biophysics letters*. 30:284-294

11 H. Huang, C.Y. Dong, H-S Kwon, J.D. Sutin, R.D. Kamm, P.T.C. So. 2002, **Three dimensional cellular deformation analysis with a two photon magnetic manipulator workstation,** *Biophysical Journal*, 82:2211-2223

12 C. Gosse and V. Croquette. 2002, **Magnetic Tweezers: Micromanipulation and Force Measurement at the Molecular Level**, *Biophysical Journal*, 82:3314-3329

13 H. Liang, T.Y. Do, S. Kasravi, P. Aurasteh, A. Nguyen, A. Huang, Z.F. Wang, M.W. Berns, 2000, **Chromosomes are target sites for photodynamic therapy as demonstrated by subcellular laser**

microirradiation, *Journal Of Photochemistry And Photobiology B-Biology*, 54 (2-3): 175-184

14 I.M Peters, Y. van. Kooyk, S.J. vanVliet, B.G. de. Grooth, C.G. Figdor, J. Greve. 1999. **3D Single-Particle Tracking and Optical Trap Measurements on Adhesion Proteins**. *Cytometry*, 36:189-194. ISSN 0196-4763.

15 C.A.J. Putman, K.O. van der Werf, B.G. de Grooth, N.F. van Hulst, J. Greve. 1994 **Tapping mode atomic-force microscopy in liquid**, *Applied Physics Letter* 64 (18): 2454-2456

16 C. Rotsch, K. Jacobson, M. Radmacher, 1999 **Dimensional and mechanical dynamics of active and stable edges in motile fibroblasts investigated by using atomic force microscopy** *PNAS*

17 R.V. Skibbens, E.D. Salmon. 1997, **Micromanipulation of chromosomes in mitotic vertebrate tissue cells: Tension controls the state of kinetochore movement** *Experimental Cell Research* 325:314-324.

18 A.Caspi, R. Granek, M. Elbaum. 2002, **Diffusion and directed motion in cellular transport.** *Physical Review E* 66 (1)

19 Y.Tseng, T.P. Kole, D. Wirtz, 2002, **Micromechanical mapping of live cells by multiple-particle-tracking microrheology** *Biophysical Journal*. 83:3162

20 A.R. Bausch, W. Möller, E. Sackmann, 1999, **Measurement of local viscosity and forces in living cells by magnetic tweezers**, *Biophysical Journal*, 76:573-579

21 P.A. Valberg, H.A. Feldman, 1987. **Magnetic particle motions within living cells. Measurement of cytoplasmic viscosity and motile assay**. *Biophys. J.* 52:551-69

2. Designing the magnetic setup

2.1. Introduction

In this chapter, the theoretical aspects of magnetic tweezers are described. First a short overview of the relevant fundamentals of magnetic theory is given. After that, we describe the design criteria of a pair tweezers for biological nano-manipulation purposes. From there the potential of the possible configurations is shown, going from a simple single pole, to multiple poles and tweezers arrays.

2.2. Theory on magnetism

2.2.1. Forces on a magnetic particle

Placing a magnetic particle with dipole moment $\vec{m}$ in a magnetic field $\vec{H}$ with flux density $\vec{B}$, two forces can be distinguished. First, a magnetic particle will always try to align itself with the external magnetic field (Figure 2.1). The torque τ exerted depends on the magnetisation of the particle and the magnetic flux density.

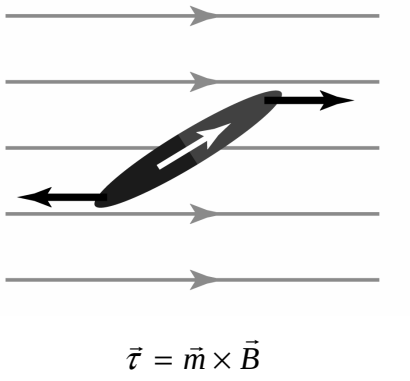

$$\vec{\tau} = \vec{m} \times \vec{B}$$

Figure 2.1 Magnetic torque

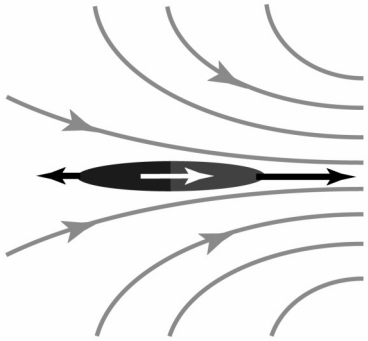

$$F_x = \nabla \left(\vec{m} \cdot \vec{B} \right)$$

Figure 2.2 Magnetic translation force

Second, in a field with a gradient in the magnetic flux density, the particle will feel a translational force *F* in the direction of the highest flux density (Figure 2.2).

The components of the magnetic force on a dipole are given by [1]

$$F_x = \vec{m} \cdot \frac{d\vec{B}}{dx} \tag{2.1}$$

When the magnetic dipole is a constant, the gradient can be moved forward in the equation, resulting in [2]:

$$\vec{F} = \nabla\left(\vec{m} \cdot \vec{B}\right) \tag{2.2}$$

Assuming that either the particle or its magnetic dipole moment is free to rotate, the vector product reduces to a scalar product, and the force is proportional to the amplitude of the magnetic moment of the particle and to the gradient in the magnetic flux density:

$$\vec{F} = \left|\vec{m}\right| \nabla \left|\vec{B}\right| \tag{2.3}$$

Most traditional magnetic tweezers focus on the torque created by a magnetic field to rotate a particle, and produce very little translational force. In these cases, the used fields are relatively homogenous. In contrast, our goal is to exert translational forces to the particles, which requires very large field gradients combined with magnetic particles exhibiting high magnetisation.

2.2.2. Trapping a particle

Knowing how to produce a force on a particle, the next question is whether it is possible to produce a stable magnetic trap to hold the particle at one spot.

Already in 1842 Samuel Earnshaw proved what is now called Earnshaw's Theorem [3] which states that no static system governed by inverse square laws (e.g. electric, magnetic or gravitational field) can possess the local energy minimum that would be necessary if a particle is to have a stable location.

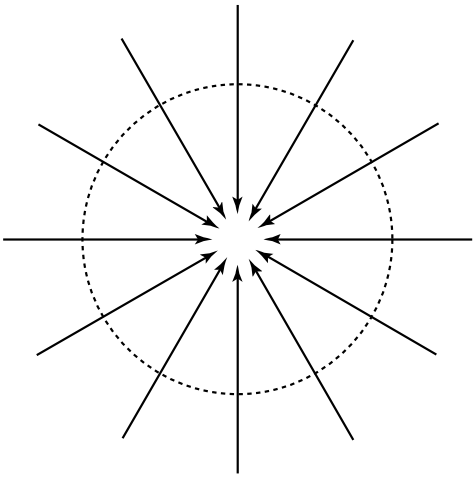

Figure 2.3 Force vectors configuration needed for a stable trap

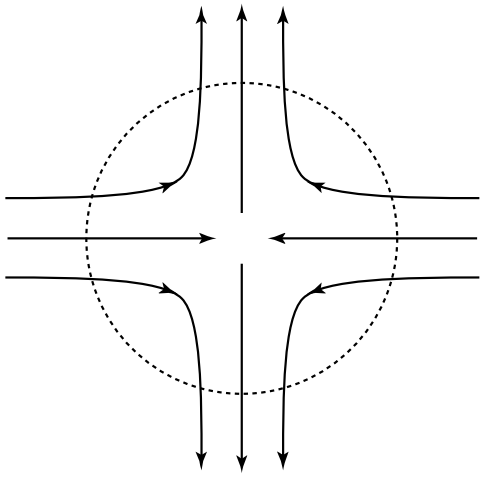

Figure 2.4 Saddle point is the only source free configuration

A stable trap would require an unoccupied point in space where the force vector everywhere on the surface of the infinitesimal sphere surrounding the point is directed inward (Figure 2.3). But according to Gauss's Law, the integral of the force vector over any closed surface equals the charge contained within the surface. Because there is no charge at the centre, this situation can simply not exist. Aside from a situation with no force at all, the only other converging force situation that can exist is a so-called saddle point (Figure 2.4) Here the 'trap' only exist in one dimension, but is reversed in the other dimension, so that it still satisfies Gauss's Law.

A stable magnetic trap would thus need to circumvent the conditions of Earnshaw's Theorem. This can be done by trapping diamagnetic or superconducting materials that do not follow the inverse force law. However, diamagnetism is an extremely small effect, and super conductance does not occur at room temperature. Both are therefore not usable for magnetic tweezers experiments in living cells. Because of this impossibility to make a static magnetic trap, the magnetic tweezers will have to rely on active feedback for positional control.

2.2.3. Magnetic saturation

In working with ferromagnetic materials, we will encounter the phenomena of magnetic saturation (Figure 2.5). When a ferromagnetic material is placed in an external magnetic field, microscopic magnetic domains will grow and eventually align themselves with this field, producing the enormous magnetisation boost that these materials are known for. When all domains are fully aligned with the external field, the magnetisation will not further increase with increasing external magnetic field, and the material is said to be saturated.

Ferromagnetic materials will be used to transport magnetic flux from an electromagnet to the area of interest. The saturation of the used material will therefore give an upper limit to the amount of flux that can be delivered. This shows that the choice of the material is very important. Materials showing the highest magnetic saturation are iron, cobalt and their alloys, with a saturation induction around two tesla.

The size of the magnetic domains in these materials is typically in the order of micrometres. Designing structures with the same size, can lead to situations were the material consist of a single domain. In that case a macroscopic calculation of magnetic behaviour doesn't hold, as a single domain is by definition saturated independent on external magnetic field, and can only change size and direction.

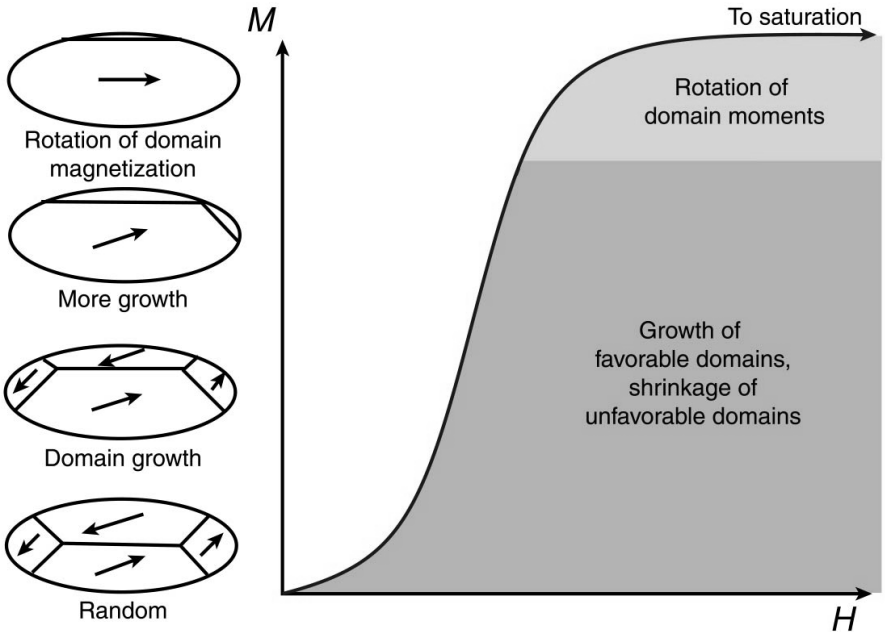

Figure 2.5 Magnetic saturation. The pictures on the left indicate the magnetic domain structure corresponding to the magnetisation. At an applied external field of *H*=0 A/m the domains are randomly orientated (bottom picture). Increasing the applied field, favourable domains start to grow at the expense of unfavourable domains. When the domains cannot grow further, they rotate to align themselves with the external field. When all domains are aligned with the external field, the material is fully saturated.

2.3. Design of the magnetic tweezers

2.3.1. Design criteria

Dimensions of the tweezers

The magnetic tweezers proposed are designed to perform nano-manipulation inside single living cells. We have focused on making an instrument for manipulation of DNA and proteins inside the nucleus of HeLa cells. This means that the area of interest for our tweezers is roughly the size of a cell. Therefore, the work area needs a minimal spacing of 20 micrometres to allow for one cell (typical dimensions 10~20 μm) to be positioned between the poles.

The tweezers will also have to be incorporated in a microscope, where the objective is restricting space around the substrate.

Required force

Presently it is not clear how much force is required to manipulate small particles in a cell or how much force would be required to, for example, deform chromatin inside a cell.
From in-vitro experiments on molecules like RNA polymerase [4] and kinesin [5] we do know that a force in the order of 10 pN is needed for molecular manipulation. It is not clear how these forces will relate to in vivo forces where the environment is far more complex.
We plan to produce these forces with particles that are as small as possible to limit disturbances to other parts of the cell. To be able to move the particle to different positions in the cell, the forces should be as homogenous as possible across the area of interest. To be able to function as a pair of tweezers, the force direction and amplitude should also be readily controllable.

Magnetic probe requirements

The particles used as probes should each be so small that they do not interfere with the system under investigation. Typical proteins that will be investigated are in the order of 10 nm in size, marking a lower limit of the size of the probe. Depending on the environment, larger beads can be used (50 to 200 nm). To be able to achieve a sufficiently large magnetic moment in the smallest volume, the probes need to be composed of a material that is easily magnetized, and has a very high volume magnetisation. To be able to assess magnetic force without needing to calibrate every particle, the magnitude of the magnetic moment should have a narrow distribution.
To prevent magnetic clustering of particles, the probes should be paramagnetic, and they should be stable in aqueous environments. Clearly, the probe needs to be biocompatible, and it should be possible to functionalize the probe by attaching appropriate molecules.

Biocompatibility of the materials

Working with living biological samples imposes several restraints on our choice of materials. First, the magnetic structures should be resistant to an aqueous environment, if it will be submerged in the same medium as the cells. Second, they also have to be biocompatible. For any magnetic structures, this means that they should be non-toxic for the cells. For the sample area, this also includes factors like cell adhesion to the substrate.

Timescale of a typical experiment

The timescale on which experiments take place, will of course depend on the speed at which the particle moves through the cell. This speed v at which a particle with diameter d moves through a viscous medium can be described by:

$$\vec{v} = \frac{\vec{F}}{\gamma} \quad with \quad \gamma = 3\pi\eta d \quad (spherical\ particles) \tag{2.4}$$

Where F is the force on the particle, γ the viscous drag and η the viscosity.
Assuming the particle or its dipole moment is free to rotate, we can fill equation (2.4) into equation (2.3). A homogeneously magnetized spherical particle will then move at a speed v in the direction of the magnetic gradient:

$$\vec{v} = \frac{d^2 M_{particle} \nabla \left| \vec{B} \right|}{18\eta} \tag{2.5}$$

Where $M_{particle}$ is the volume magnetization of the particle.

The reported values of measured internal cell viscosity range from as high as 10^4~10^5 Pa·s [6], to 10^2~10^3 Pa·s [7,8,9] down to 5~10 Pa·s [10]. Part of the problem is that viscosity is a term that is not readily applicable to a heterogeneous environment like a cell. The inside of the cell, consisting of cytoskeleton,

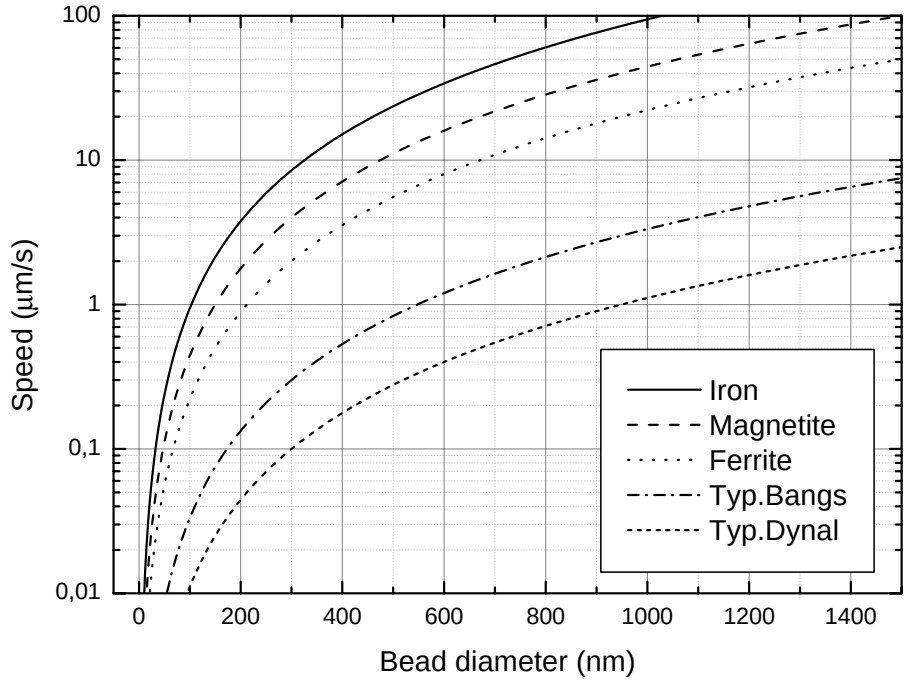

Figure 2.6 Speed of a bead in a medium of 10 Pa·s depending of diameter and material. A gradient in the magnetic flux density of 10 kT/m is assumed. Volume magnetization of the various iron oxides, as well as the typical beads from Bangs and Dynal (containing only a fraction of iron oxides) are shown.

organelles and cytoplasm creates a very complex viscoelastic environment. Differences in the way the viscosity is measured (twist or shear forces), in the type of cells that are investigated, and in the size and shape of the probe, are responsible for large deviations in the reported values.

Smaller beads will experience a lower apparent viscosity because they pass more easily through the cytoskeleton. Considering that the beads used in this magnetic tweezers will be relatively small (<μm) compared to the probes used in the viscosity experiments, the reported value of 10 Pa·s will be used for the cell viscosity. Using an order of magnitude value for the gradient in the flux density (10^4 T/m) then allows predicting speeds for different bead diameter and material types, as done in Figure 2.6. Clearly, even for quite small beads, the particle speed at high magnetic force is easily in the order 1 μm/s. This means that a feedback system with 10 nm accuracy will need a bandwidth in the kHz range.

2.3.2. Functional Design

In the design of the magnetic tweezers, one can distinguish three functions:

- Generation of the magnetic flux.
- Transport of the flux to the area of interest
- Producing the required gradient in the flux density.

In the following sections, these functions will be handled in more detail.

2.4. Flux generation

Magnetic flux can be generated either by using a permanent magnet, or an electromagnet. A permanent magnet has the advantage that it is small and powerful, and it requires no external sources. The problem however, is that the field on the probe is not controllable other then by (re)moving the magnet itself. Therefore, permanent magnets are ill suited for a manipulation instrument where fast and flexible feedback is required. As the time scale criterion requires a kHz bandwidth for the feedback, permanent magnets are clearly out of the question for this magnetic tweezers.

Therefore, electromagnets will be used to generate the magnetic flux. Space restrictions caused by the objective of the microscope force us either to make the electromagnet on a micrometre scale close to the sample area, or to place the electromagnets far away from the substrate and couple the flux to the poles.
Macroscopic electromagnets are the most obvious choice. They are flexible, easy to produce and powerful enough.
In contrast, the possibility of manufacturing a complete micrometre-scale electromagnet on a substrate, with flux orientation along the substrate had only

just been demonstrated at the start of the project [11]. In our case, the 10mm long solenoid with 92 windings would be required to sustain a current density of 10^3 A/mm^2 to satisfy the absolute minimum flux requirements, requiring special cooling arrangements. In addition, the achieved magnetisation saturation was only 0.8 T, limiting the maximum achievable force. From a practical point of view, we also have to consider the conditions under which the substrates containing the magnetic structures would have to be used in a biological environment. The substrates will need to withstand aggressive cleaning if used multiple times, and should not be damaged easily. Therefore, it is not practical to place difficult to manufacture micrometre-scale electromagnets on the substrates.
Because of the reason give above, macroscopic electromagnets are clearly preferred, and were selected for generating the flux in our magnetic tweezers.

2.5. Flux transport

When the electromagnets are placed far away from the sample area, the generated flux will have to be transported toward the area of interest. Designing the magnetic circuit, we need to keep in mind that magnetic field lines always form closed loops.
Because of this, it is surprisingly difficult to transport flux to the tip of a single pole. Air has a magnetic reluctance five orders of magnitude higher than ferromagnetic material. As the flux flows along the path of lowest reluctance, there is no tendency for the field lines to extend towards the extremities of the pole, as this also means a longer path through the air.
Including a second pole, produces a magnetic path of lower reluctance, driving the flux towards the pole tips, making saturation possible with relatively little effort (see Figure 2.7).

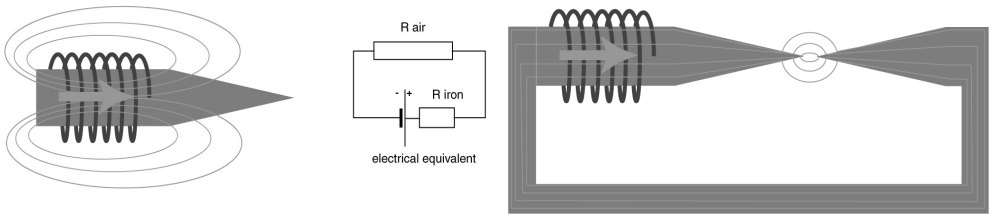

Figure 2.7 In a single pole, it is unfavorable to saturate the extremity of the pole, due to the high reluctance on the air. Extending the magnetic circuit so as to include a second pole, produces a smaller air gap which lowers the reluctance for this path, thereby increasing the flux. Included in the picture, is the electrical analog in air, where magnetic flux corresponds to electrical current, magnetic reluctance to resistance, and the magneto motive force (number of coils times current) to the voltage.

2.6. Producing a gradient in the magnetic flux density

2.6.1. Gradient produced by a single pole

We start by evaluating the magnetic field gradient resulting from a single uniformly magnetized parabolic shaped pole. For such a system, the resulting field can be calculated analytically.

Because there are no electrical currents, the scalar magnetic potential φ_m is used for calculating the magnetic field $\vec{H}$:

$$\vec{H} = -\nabla \varphi_m \tag{2.6}$$

Assuming that the magnetization $\vec{M}$ of the pole is constant and uniform under all conditions, an effective magnetic surface charge $\sigma_m = \vec{n} \cdot \vec{M}$ can be defined, with $\vec{n}$ the normal to the surface of the pole.

The scalar magnetic potential is then given by [12]:

$$\varphi_m = \frac{1}{4\pi} \int \frac{\sigma_m}{\xi} dA \tag{2.7}$$

Where ξ is the distance to the surface element *dA* of the pole and z the distance to the pole extremity along the axis of the paraboloid (see Figure 2.8).

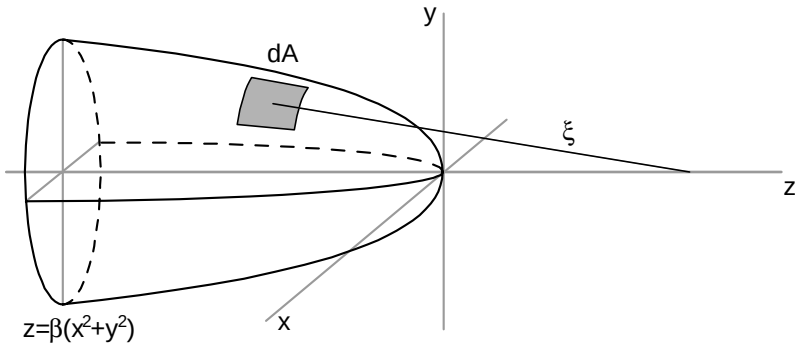

Figure 2.8 Parabolic pole tip

The integration extends over the whole pole surface, described by the quadratic equation $z=\beta R^2$ with $R^2=x^2+y^2$. The surface charge is equal to $\sigma_m=M\cos\alpha$, with $\tan\alpha=-2\beta R$ the tangent to the paraboloid, with *M* the amplitude of the magnetisation. Evaluation of the integral and subsequent differentiation to *z* yields

the following expression for the magnetic field outside the magnetic material and along the paraboloid axis (R=0):

$$H_z(z) = -\frac{\partial \varphi_m(z)}{\partial z} = \frac{M}{(4\beta z + 1)} \tag{2.8}$$

The expression for the gradient in the magnetic flux density outside of the

$$\frac{\partial B_z(z)}{\partial z} = \mu_0 \frac{\partial H(z)}{\partial z} = \frac{4\mu_0 M\beta}{(4\beta z + 1)^2} \tag{2.9}$$

magnetic pole (permeability $\mu=\mu_0$) then follows from:
with $\mu_0=4\pi\ 10^{-7}$ *Tm/A* the vacuum permeability. This equation has been used to evaluate $\partial B_z/\partial z$ for different pole sizes as shown in Figure 2.9. For the magnetisation *M* a value of 1430 kA/m is assumed, corresponding to a bulk saturation magnetization of cobalt, one of the candidates materials to use for the poles.
The optimum curvature for a given distance, follows from the condition $\partial F_z/\partial\beta=0$ which yields $\beta=1/4z$. Inserting this into equation (2.9) gives:
This is the maximum attainable gradient for an optimal diameter relative to the

$$\frac{\partial B_z(z)}{\partial z} = \frac{\mu_0 M}{4z} \tag{2.10}$$

distance from the tip, as is shown in Figure 2.9 by the straight dotted line.

From the one-pole approximation, we can expect a magnetic field gradient of 30 (typical) to 45 (optimum) kT/m at 10 µm distance from the pole tip. With this value for the gradient in the magnetic field, we can now estimate the maximum magnetic force on a uniform magnetized magnetic spherical particle (magnetized in the z-direction) using:

$$F_z(z) = m_{bead}\frac{\partial B(z)}{\partial z} \quad with \quad m_{bead} = \tfrac{1}{6}\pi d_{bead}^3 M_{bead} \tag{2.11}$$

with m_{bead} the saturation magnetisation, d_{bead} the diameter and M_{bead} the volume magnetisation of the attracted bead. Figure 2.10 shows the magnetic force on a bead as a function of the diameter of the bead as calculated with equation (2.11). The materials typically used in commercially available (para)magnetic beads are shown. The graph illustrates the enormous force potential of the magnetic tweezers compared to e.g. optical tweezers, where pico-Newton forces can be achieved with beads as small as 50 nm. Stall force measurements on single DNA

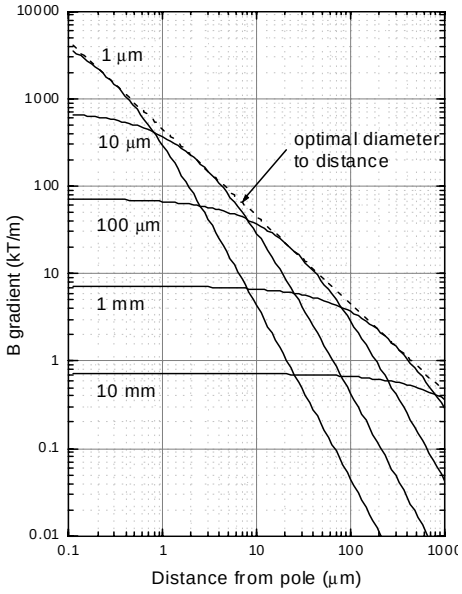

Figure 2.9 The gradient in the magnetic flux density produced by a single saturated magnetic pole, as a function of the distance from this pole. Shown are curves for several pole diameters for a given distance, marking the maximum boundary.

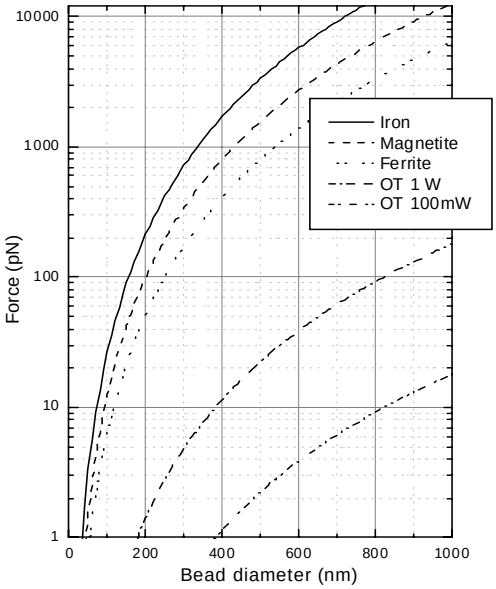

Figure 2.10 Magnetic force on a bead as a function of the bead diameter. The magnetic flux gradient is assumed to be 30 kT/m. Curves are shown for the typical bead materials (iron and its oxides). For comparison, also the forces exerted by Optical Tweezers on polystyrene beads at 100 and 1000 mW laser power are shown.

polymerase molecules as discussed in chapter one, would need beads of 100nm diameter to produce the required force (~15 pN).

2.6.2. Gradient produced by multiple poles

The single pole calculations give an indication of the dimensions of the required poles and beads. However, there are some omissions in the single pole approximation. It does not consider how to achieve magnetic saturation of the pole, nor does it address how to control the amplitude and direction of the magnetic force.

Directional control over the force on a bead becomes possible with multiple poles that can attract a bead. The structures will have to be designed in such a way that the poles can produce attracting forces in both positive and negative direction of the axes of movement. We will restrict ourselves to magnetic tweezers that can exert forces in two dimensions. This means that a minimum of three poles is necessary, where the poles are rotationally arranged at 120 degrees intervals.

Increasing the number of poles to four, with poles along the axis of a Cartesian coordinate system in the manipulation plane, gives a system where magnetic force and the corresponding movement of a bead are easier to control.

Using the optimized parabolic shaped poles, as assumed in the single pole simulation to create such a multiple pole, yields a situation where the poles are exactly touching each other, short-circuiting the magnetic structure, making the single pole calculations invalid.

To simulate the magnetic field in multiple pole configurations we resort to numerical calculations using a finite element method. All simulations were performed using Femlab from Comsol AB, which is an extension running on top of MathWorks Matlab.
Although the structures proposed are three dimensional by nature, most simulations have been performed in two-dimensional space to limit the complexity of the model. Especially with non-linear components like magnetic saturation, this already strains a personal computer to its limits. Because there are no special features in the third dimension, a 2D simulation will give useful results for situations where the poles are high compared to the distance between the pole tips. Decreasing the height, edge effects will start to play a role. This influence will be further investigated in section 2.6.4 later in this chapter.

Figure 2.11 shows one of the geometries used in the simulations. The centre area with the four magnetic poles is to scale. The distance between the pole tips is 20 micrometre, and the width 8 micrometre. The edges of the poles are rounded to one micrometre radius. To calculate the resulting field it is necessary to include the macroscopic yoke and coils around the poles. As these are many centimetres large in reality, they have not been reproduced to scale in the model, in order to reduce the complexity of the model and corresponding calculation times. To include these structures in the model, without compromising the model due to flux leakage outside the pole tips, a modified air layer is positioned in between the “feet” of the pole tips on the yoke. The relative permeability of this layer is artificially set to 0.1, which allows to reduce the length scale of the air by a factor of 10, which is sufficient to remove excessive flux leakage.

The pole tips are only a few micrometres in size, which is in the same order of the typical magnetic domain size for the used materials. That means that in practice the tips might consist of a single magnetic domain. Therefore, two types of simulations have been performed simulating single domain at the pole tip and multiple domain (bulk) behaviour.

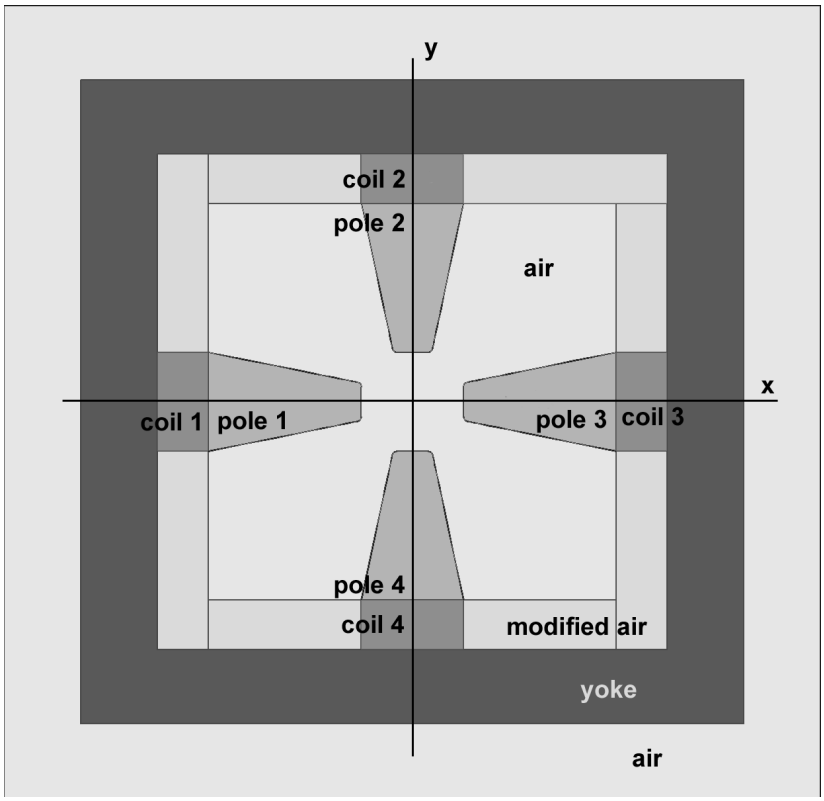

Figure 2.11 Geometry used to simulate pole structure. The poles are 8 μm wide. The space between the poles is 20 μm wide.

Magnetic domain behaviour, and thus the behaviour of a single domain in the tip of the magnetic pole, is very difficult to simulate accurately, and takes specialized software. It also requires very well defined layers, as domains may be pinned by structural defect, particularly nonmagnetic inclusions, voids or precipitates of a nonmagnetic phase. The magnetic hardness of the layer can serve as an indication for the amount of domain wall pinning. Considering the crudeness of the possible deposition techniques coupled to the relatively high (>> μm) structures proposed, it will be useless to try to exactly predict the behaviour of a single domain in the pole tip.
Therefore, a fixed magnetisation is assumed at the pole to simulate a fixed single domain oriented in the proper direction. This gives an estimate to what extent domain behaviour can have an influence on bulk simulations.

For a multi domain material, the magnetic flux is produced in the coil region outside the pole tips, simulated by applying a corresponding magnetisation at that region.
The pole region is described using a non-linear magnetic permeability to simulate the saturation of the material (Figure 2.12). The relative permeability of the pole is described using the following mathematical function:

$$\mu_r^{\ pole}(r) = \frac{\mu_{r,start} - \mu_{r,end}}{1 + e^{d\mu_r (B(r) - B_{sat})}} + \mu_{r,end} \qquad (2.12)$$

It starts at a high permeability $\mu_{r,\ start}$ and reaching the saturation induction B_{sat} quickly drops down to the final permeability $\mu_{r,\ end}$. For all simulations, the saturation B_{sat} is assumed to be 1.8 tesla.
The speed at which the permeability drops can be adjusted with the $d\mu_r$ parameter. The $d\mu_r$ parameter is set to 10 T^{-1}. Varying this parameter was found to have very little influence on the results.

Different combinations of coil current were investigated. To produce a magnetic force towards pole 1, a magnetic gradient from the remainder of the poles into pole 1 has to be produced. This is done by applying an outward flux flowing out

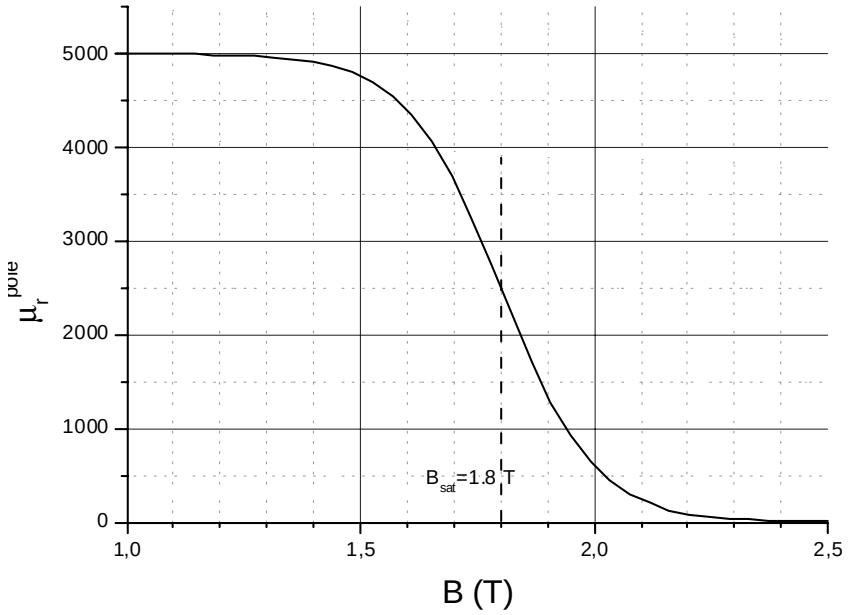

Figure 2.12 Plot of the mathematical function used to simulate the non-linear permeability of ferromagnetic materials. The function starts at high permeability $\mu_{r,\ start}$=5000, and reaching the saturation induction B_{sat} =1.8 T then drops quickly to a value of $\mu_{r,\ end}$=1 simulating saturation.

of pole 1, combined with an inward flux for the other poles. (or vice versa).
All the coils can be driven at the same current ("equal coil currents"). Alternatively the coil current can be distributed so that the total incoming and outgoing flux that are produced by the coils is equal ("balanced coil currents") corresponding to a multi-domain behaviour where only a single pole is saturated. The flux generated by the coil is introduced into the model by setting a fixed magnetization of given amplitude and direction into the coil region indicated in Figure 2.11.

Combining these possibilities produces four different magnetisation configurations which have all been simulated for the three and four pole configurations. The input parameters for the Femlab models are listed in Table 2.1 through Table 2.4.

Table 2.1 Simulation parameters for the four-pole simulations "remote coils"

		Equal coil currents		Balanced coil currents	
	μ_r	M_x	M_y	M_x	M_y
Coil 1	1	M_0	0	M_0	0
Coil 2	1	0	M_0	0	0.33 M_0
Coil 3	1	M_0	0	0.33 M_0	0
Coil 4	1	0	$-M_0$	0	-0.33 M_0
Pole 1 – 4	μ_r^{pole}	-	-	-	-
Air	1	-	-	-	-
Modified air	0.1	-	-	-	-
Yoke	5000	-	-	-	-

With M_0 = 1430 kA/m, μ_r^{pole} given by eq. (2.12)

Table 2.2 Simulation parameters for the four-pole simulations "fixed magnetization in pole"

		Equal coil currents		Balanced coil currents	
	μ_r	M_x	M_y	M_x	M_y
Coil & pole 1	1	M_0	0	M_0	0
Coil & pole 2	1	0	M_0	0	0.33 M_0
Coil & pole 3	1	M_0	0	0.33 M_0	0
Coil & pole 4	1	0	$-M_0$	0	-0.33 M_0
Air	1	-	-	-	-
Modified air	0.1	-	-	-	-
Yoke	5000	-	-	-	-

With M_0 = 1430 kA/m

Table 2.3 Simulation parameters for the three-pole simulations "remote coils"

		Equal coil currents		Balanced coil currents	
	μ_r	M_x	M_y	M_x	M_y
Coil 1	1	M_0	0	M_0	0
Coil 2	1	0.5 M_0	0.866 M_0	0.25 M_0	0.433 M_0
Coil 3	1	0.5 M_0	-0.866 M_0	0.25 M_0	-0.433 M_0
Pole 1 – 3	μ_r^{pole}	-	-	-	-
Air	1	-	-	-	-
Modified air	0.1	-	-	-	-
Yoke	5000	-	-	-	-

With M_0 = 1430 kA/m, μ_r^{pole} given by eq. (2.12)

Table 2.4 Simulation parameters for the three-pole simulations "fixed magnetization in pole"

		Equal coil currents		Balanced coil currents	
	μ_r	M_x	M_y	M_x	M_y
Coil & pole 1	1	M_0	0	M_0	0
Coil & pole 2	1	0.5 M_0	0.866 M_0	0.25 M_0	0.433 M_0
Coil & pole 3	1	0.5 M_0	-0.866 M_0	0.25 M_0	-0.433 M_0
Air	1	-	-	-	-
Modified air	0.1	-	-	-	-
Yoke	5000	-	-	-	-

With M_0 = 1430 kA/m

The simulations in Femlab produce a magnetic flux distribution map. Typical results are shown for a four-pole structure (Figure 2.13) as well as for a three-pole structure (Figure 2.14). All simulations were performed with an incoming flux from the left pole where the other poles transport the flux away again. This configuration will produce a magnetic gradient and force to the left (negative x direction).

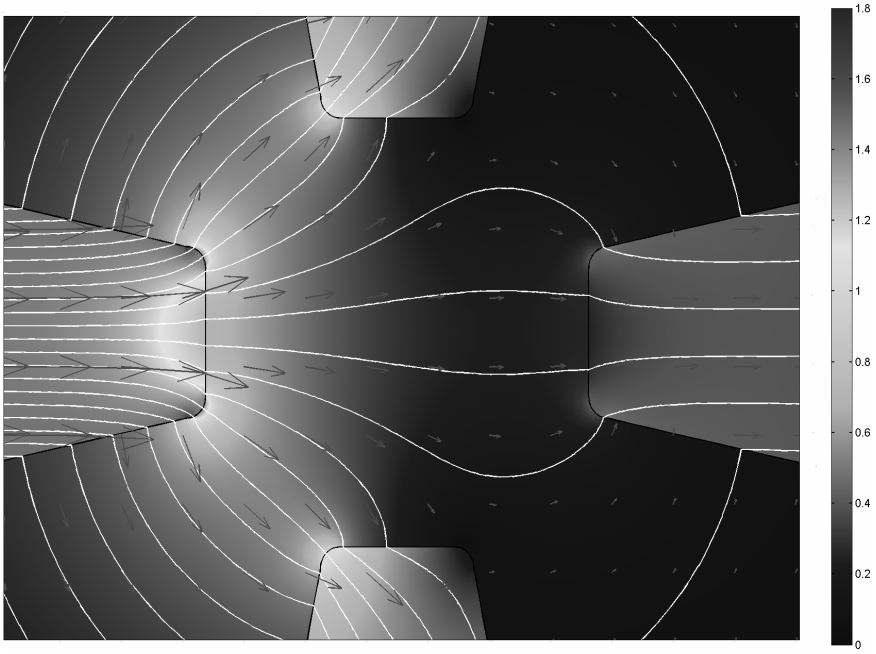

Figure 2.13 Typical B field lines (white lines) for a four-pole structure. (Shown is the "balanced coil currents" "remote coils" configuration) Vectors indicate the local flux density and direction. In addition, the colour map indicates the flux density.

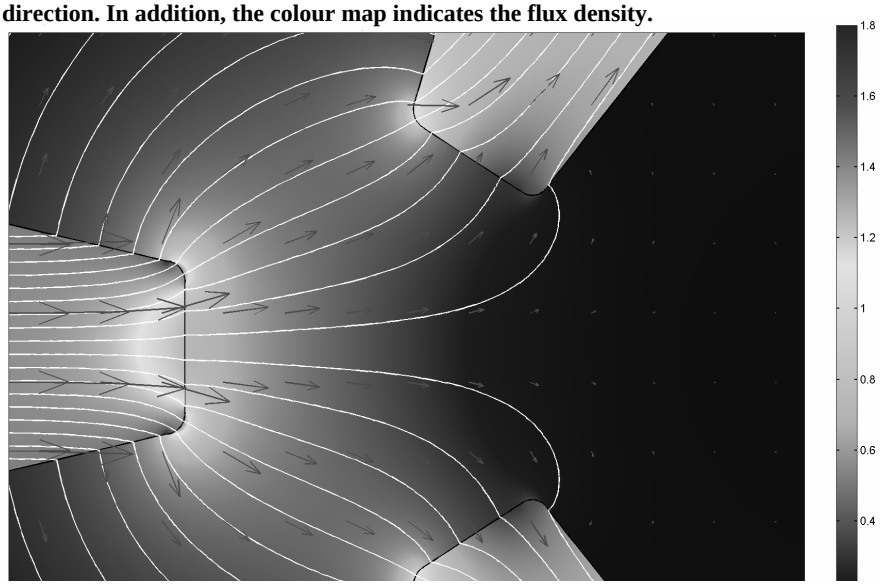

Figure 2.14 Typical B field lines for a three pole structure. (Shown is the "balanced coil currents" "remote coils" configuration). Vectors indicate the local flux density and direction. In addition, the colour map indicates the flux density.

The results are shown in Table 2.5 and Table 2.6. The magnetic flux gradients are given at the centre of the tweezers (0µm), and closer (-5µm) and further (+5µm) away along the axis of the attracting pole.

Table 2.5 Field gradients in four-pole configuration

	Flux density gradient (kT/m)					
	Equal coil currents			Balanced coil currents		
	-5 µm	0 µm	+5 µm	-5 µm	0 µm	+5 µm
Fixed magnetisation at tip	-86	-52	20	-72	-34	-2
Remote coils	-72	-37	-3	-49	-25	-2

Table 2.6 Field gradients in three pole configuration

	Flux density gradient (kT/m)					
	Equal coil currents			Balanced coil currents		
	-5 µm	0 µm	+5 µm	-5 µm	0 µm	+5 µm
Fixed magnetisation at tip	-78	-66	-74	-72	-45	-44
Remote coils	-52	-41	-43	-40	-31	-31

It is interesting to see that the ratios between the values at different distances in the four situations remain mostly the same, and primarily the amplitude changes. The highest forces are achieved with a fixed magnetisation at the tip at equal coil currents. This corresponds to single domain poles. The values listed for that configuration are very close to the absolute theoretical limit to the flux density gradient. This limit is found by simply taking the flux density of a saturated pole (1.8 T) and reducing it linearly to zero over a distance of 20 micrometres, yielding a gradient of 90 kT/m.
The reason that this value is not reached for the multi domain simulation, can be seen in Figure 2.13. The magnetic field lines already start to diverge before they reach the end of the tip, lowering the magnetic flux density significantly before it leaves the pole tip.

The multi-domain setup shows a higher force when driven at equal coil currents. More total flux is generated, and the two opposite poles help pull flux through the almost saturated single pole.

We will use the lowest of the values from these simulations in our further investigations. When we compare these values to the single pole results, it is clear that actually, these multi pole values are not low at all! Figure 2.15 shows the gradient along the x-axis for the four and three multi domain poles driven at

balanced coil current. For comparison, the gradient obtained for a single saturated parabolic pole with 5 μm tip radius is shown as well.

When comparing the structures, it is obvious that while the four-pole structure can produce the highest force, actually the three-pole structure is preferable. It shows a more homogeneous force distribution, especially in the -5 to +5 μm range.

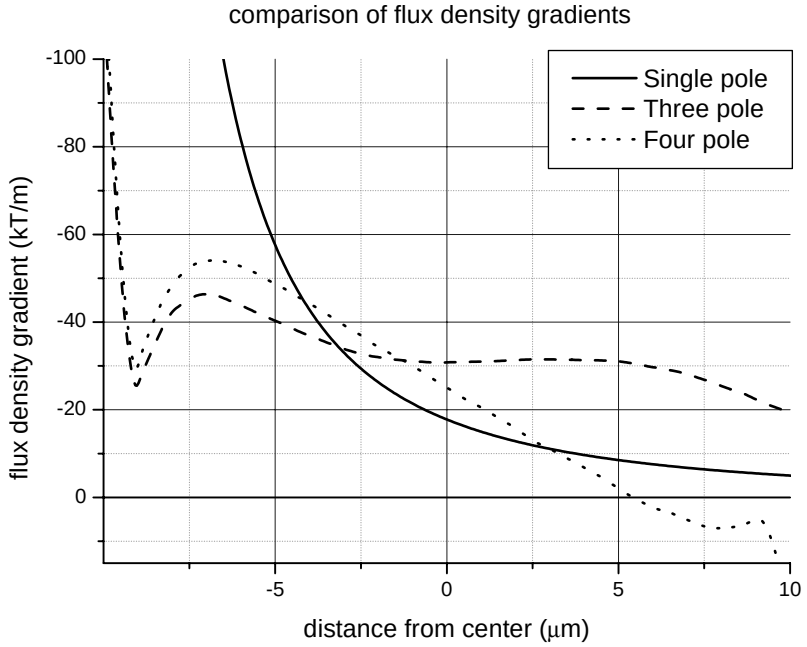

Figure 2.15 Comparison between the magnetic flux density produced by different pole configurations.

We will further investigate the homogeneity of the three and four pole geometries extending over the whole area of interest in the magnetic tweezers. Figure 2.16 shows the deviation of the x-component of the gradient in the magnetic flux density compared to its value at the centre of the tweezers. The irregularities in the contour lines are caused by the finite mesh of the simulation. Figure 2.17 compares the y-component of the gradient to the x-component, indicating how homogenous the direction of the gradient is. In an ideal case, the y-component is very small compared to the x-component. Such ideal situation is not necessary however. A feedback system can automatically compensate for such deviations. And as the deviations are static, these maps can also be used to produce a feed forward system to compensate.

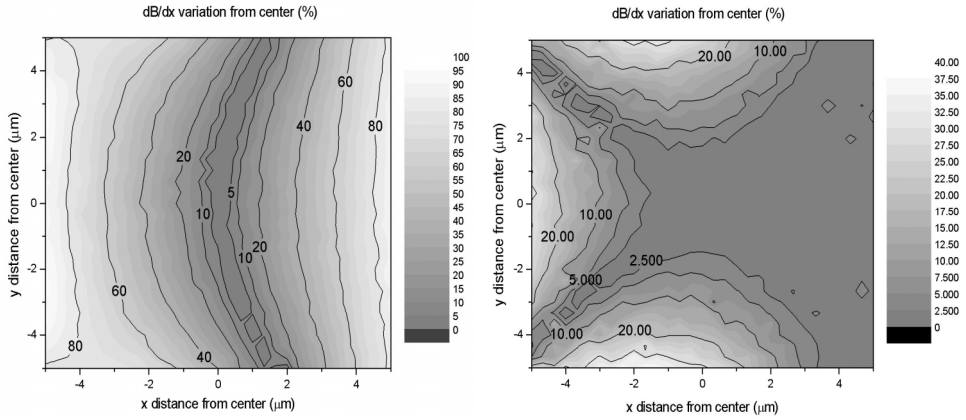

Figure 2.16 The absolute variation in the gradient in the magnetic flux density in the x direction, relative to the gradient in the center of the poles. The plot on the left shows a four-pole configuration and the plot to the right a three-pole configuration. Both have been calculated assuming multiple domain behavior and magnetic saturation. The three-pole configuration clearly shows a far greater homogeneity in the gradient, and thus force on a bead.

Large deviations in amplitude will only slow down the controlling systems. Directional deviations however can cause complete loss of control. This will happen when the orthogonal component becomes larger than the required force direction. This means that all areas in Figure 2.17 that are above 100% indicate areas where control is lost. This of course holds for all directions, so for the four-pole configurations, the area of control is diamond shape area extending to 3 μm

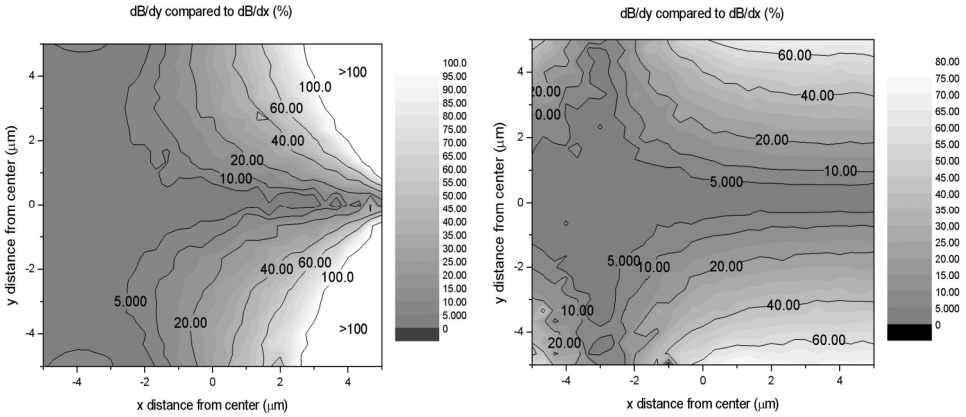

Figure 2.17 The absolute variation in the gradient in the magnetic flux density in the x direction relative to the corresponding gradient in the y direction. The plot on the left shows a four-pole configuration and the plot to the right a three-pole configuration. Both have been calculated assuming multiple domain behavior and magnetic saturation.

from the centre, while the three-pole system is controllable over the complete area of interest.

From the simulations, it is clear that a four-pole structure has limited use. It can reach higher forces close to its attracting pole, but actual tweezers need to be strong over the complete area of interest. Therefore, it can only be used for systems where the manipulation is limited to a small region of approximately 2 µm around the centre. The feedback system is easy to implement, as the four poles correspond directly to plus and minus direction of the x and y axes.

The three-pole structure in contrast, has a homogenous force amplitude (max 20% deviation) and direction (max 60% deviation) over the entire area of interest and can be used in almost the complete area between the poles. Unfortunately, the necessary feedback system is much more complicated, as we have a system with one-directional movement over three axes.

2.6.3. Pole diameter

For a single parabolic pole, it was already seen that the radius of the pole tip strongly influences the force that can be expected. It is interesting to investigate the influence of the width of the poles in a multi pole configuration. The four-pole structure used in the previous simulations has been recalculated with pole widths ranging from 4 to 12 µm. The simulation was done assuming multi domain behaviour and magnetic saturation, which is the case that should most be influenced by different pole width. Figure 2.18 shows the gradient in the flux density along the line from the attracting pole through the centre towards the opposite pole for different widths. The main area of interest (centre ten micrometres) is remarkably insensitive to the pole width at the tip. Clearly, the influence and positioning of the poles to each other is more important, than the exact shape of the individual poles. Only very close to the pole tips effects are visible. We can conclude that in thinking about structures with multiple poles, we need to think in term of average flux input and output, and not so much pole shape.

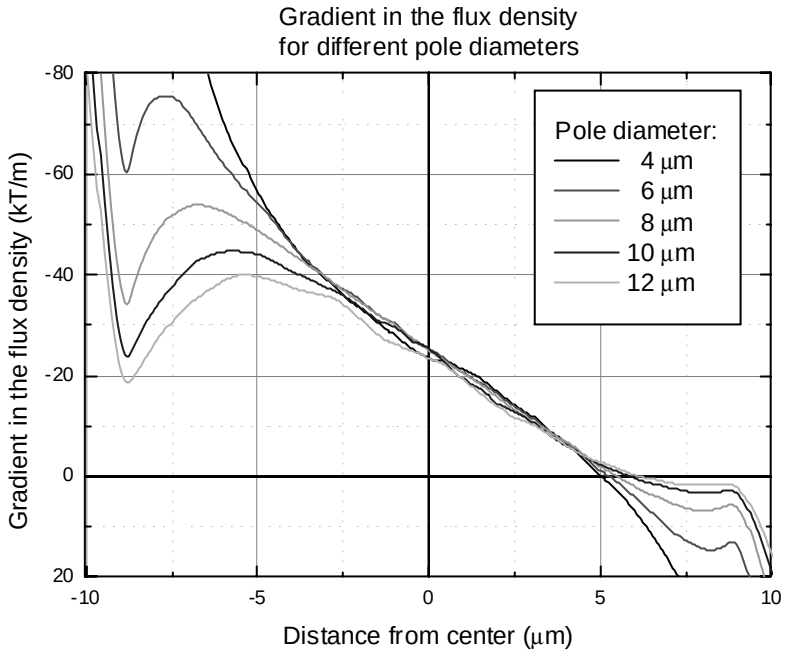

Figure 2.18 Gradient in the flux density in a four-pole configuration, calculated for different widths of the poles. The simulation assumes multi domain behavior and magnetic saturation. Clearly the center 10 micrometres which is the area of interest is hardly affected by pole diameter.

2.6.4. 2D compared to 3D

So far, we assumed in our simulations that the poles are high compared to the distance between them. In this section, this situation will be referred to as *thick* poles. In such case, a two-dimensional simulation will give similar results to a simulation including all three-dimensions. However, when the pole height is around or lower than the distance between the pole tips (*thin* poles), the field lines will spread out into the third dimension. This will lower the flux density, and thus the gradient in between the poles.

This spreading of field lines has been simulated using a 2D cross section in the *vertical direction*, spanning from one pole to another (x-axis) and in height (z-axis). Also full 3D simulations have been performed, but those are only possible using a very coarse mesh. Results of both calculations are shown in Figure 2.19.

The ratio of the 3D field gradient, describing thin poles, divided by the previous 2D prediction, that is valid for thick poles, is plotted for three different pole heights. The gradient is measured in the centre between the poles, with a pole separation of 20 μm. On the horizontal axis the height of the measurement position above the centre plane is shown. The points calculated in 3D confirm the lines produced in the vertical cross section. For a pole height of 5 μm the field gradient in the centre has dropped a factor 3 compared to the 2D calculation.

Obviously, elevating above the sample plane (moving to the right in graph), the field strength rapidly diminishes. However, within the thickness of the poles (shaded areas in Figure 2.19) the field is relatively homogeneous (within 10%).

Figure 2.20 shows the ratio between the magnetic field gradient predictions for thin and thick poles as a function of the pole thickness. As in the previous graph, the ratio is calculated using a full 3D simulation, and a 2D vertical cross section. The values coincide, validating the use of a cross section to calculate the ratio.
For poles higher than 25 micrometre, the poles can be assumed thick, and the 2D simulations from the previous sections are valid. For lower poles, a scaling factor has to be included, which can be read from the graph.

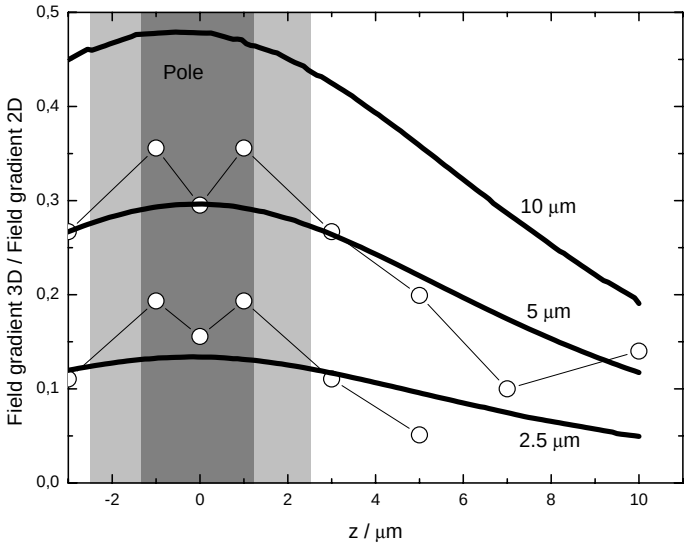

Figure 2.19 Ratio of the flux density gradient at the center of the poles, predicted by 3D and 2D simulations, shown for different pole heights. The horizontal axis indicates the height above the poles center. The broken lines with circles are derived from a full 3D simulation. The continuous lines are produced by calculating a vertical cross section in 2D. The shaded areas indicate pole thicknesses of 2.5 and 5 μm.

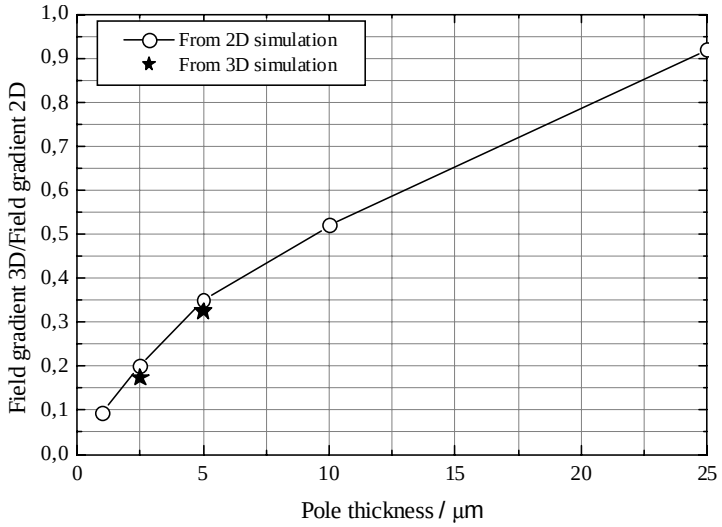

Figure 2.20 Influence of the pole thickness on the magnetic gradient, compared to the situation with unlimited pole thickness. The fractions are calculated from a full 3D simulation, as well as from a 2D cross section simulation.

From these two graphs, it can be seen that it is not necessary to simulate the pole configurations in 3D for thin poles. It is sufficient to calculate the gradient in 2D and apply a scaling factor depending on the pole thickness as plotted in Figure 2.20.

2.6.5. Pole arrays

The single three-pole tweezers geometry can be extended to an array of three poles. Rectangles of 10x20 micrometre are placed at 120 degrees angles to each other, creating a hexagonal array (see Figure 2.21). At each corner, a three-pole structure like already investigated will arise. Placing the array in a *homogenous* magnetic field, the field lines will be disturbed and follow the hexagonal structure, thereby creating the desired field gradients. Figure 2.21 shows a simulation with such a grid. With an external flux density of 0.35 tesla, local saturation can be achieved in the poles giving similar gradients as in the single three-pole geometry.

Generating such a strong field over a relatively large distance requires electromagnets that are far more powerful than the single three and four pole geometries. In addition, to be able to rotate this field along the pole tips requires the use of six electromagnets. This makes practical realization far more difficult.

An advantage of an array of poles can be that it is easier to prepare a biological experiment. With a large number of manipulation locations, it is easier to place an object between poles, for example by simply growing cells on the surface. One can then simply choose a cell that grew conveniently between a set of poles. Also damaging the pole tips is not as disastrous as with the single pole set.
Another possibility would be to do multiple tweezers experiments at once. This is of course only possible in experiments were force can be applied without active feedback, as one cannot control the array poles independent from each other.

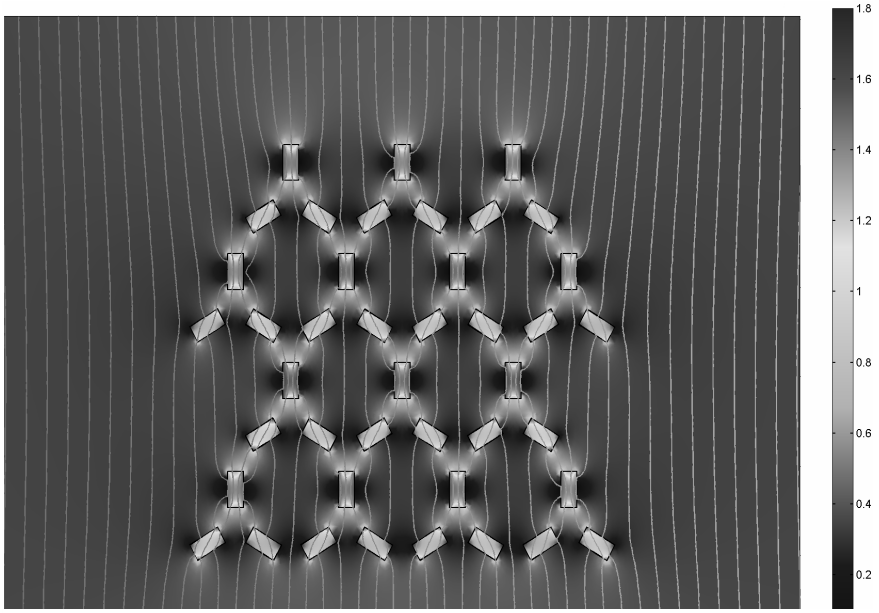

Figure 2.21 Array of triple poles

2.7. Conclusions

In this chapter, we have shown that to produce magnetic tweezers that can perform controlled manipulation inside a cell, we need to produce a gradient in the magnetic flux that is controllable in amplitude and direction. To produce sufficient force this gradient has to be achieved using micrometre scale magnetic structures. The magnetic flux flowing though these structures will be generated by remotely placed macroscopic electromagnets. The flux gradient at the sample area can then be controlled by changing the currents through the electromagnets.

Figure 2.22 shows a schematic of the complete design. It is not yet clear whether homogeneity of the force over the sample, or easy control of direction is most important. Therefore, substrates with both four- and three-pole configurations will be produced. The pole thickness has a large influence on the achieved magnetic gradient. From the simulations discussed in section 2.6.4 the effect of low pole thickness can be predicted. Poles with thickness of 5 μm will experience a magnetic gradient that is reduced by a factor 3 compared to the 2D simulations.
Finally, the force achieved by the tweezers will depend on both the gradient in the flux density, and the magnetic particle manipulated by it. Table 2.7 predicts the force on a range of typical particles, assuming a gradient in the flux density of 30 kT/m, which would be typical for a three-pole configuration as calculated in the 2D simulations. Also included is the force at 10 kT/m, which corresponds to the same three pole configuration, but corrected for a pole height of 5 μm.

Table 2.7 Expected force for typical beads at 30 and 10 kT/m flux density gradient

Bead	diameter	Vol. Magnetisation	Force @ 30kT/m	Force @ 10kT/m
	(μm)	(kA/m)	(pN)	(pN)
Dynal M280	2,80	11,5	3963	1321
Dynal M450	4,50	20,6	29472	9824
Dynal MyOne	1,05	28,4	516	172
Immunicon	0,50	800	1570	523
Bangs	0,35	64,9	44	15
Bangs	0,30	50,8	22	7
Immunicon	0,15	800	42	14
100% iron 150 nm	0,15	1700	90	30
100% iron 100 nm	0,10	1700	27	9
100% iron 50 nm	0,05	1700	3	1

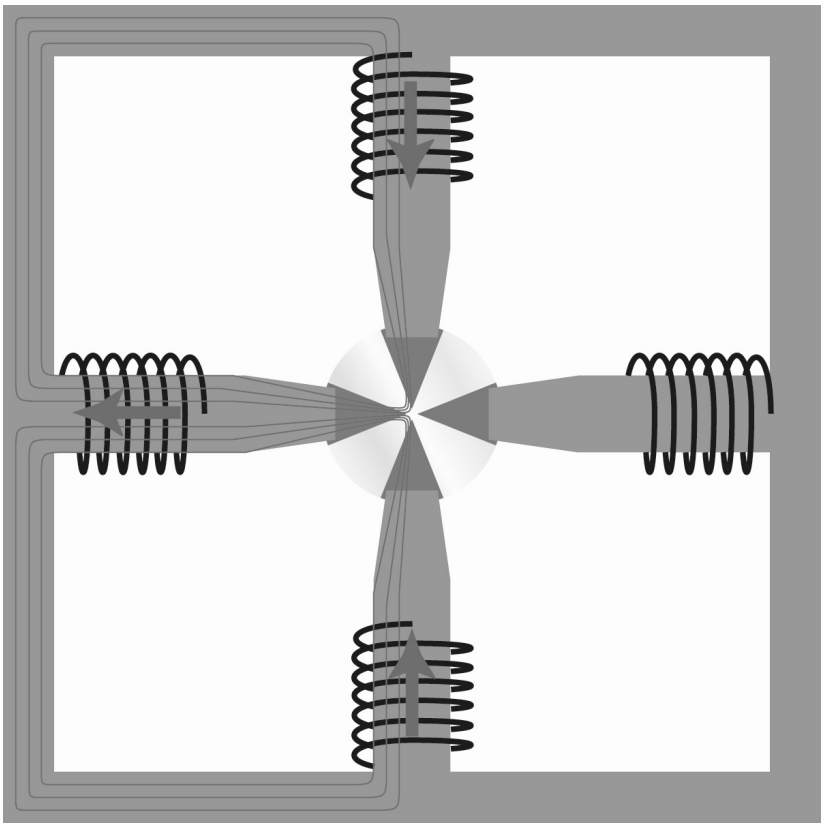

Figure 2.22 Final concept of the magnetic tweezers. The substrate with the microscopic magnetic structure producing the gradient in the magnetic flux density lies at the centre. The flux is generated with remotely placed macroscopic electromagnets. The surrounding circuit is necessary for conducting field lines, to complete the loop. The flux gradient in the area of interest can be changed simply by changing the current flowing through the electromagnets

2.8. References

1 R.M. Rose, L.A. Shepard, J. Wulff, 1966, **Structure and properties of materials, Vol. 4: Electronic properties**. *John Wiley & Sons, Inc. London*. p.184

2 J.D. Jackson, 1975. **Classical Electrodynamics**. *Wiley, New York*. 2nd ed, p.185

3 W. Earnshaw, 1842. **On the nature of the molecular forces which regulate the constitution of the luminferous ether.** *Trans. Camb. Phil. Soc.*, 7:97-112

4 M.D. Wang., M.J. Schnitzer, H.Yin, R. Landick, J.Gelles, S.M. Block. 1998. **Force and Velocity measured for single molecules of RNA polymerase**. *Science* 282:902-907

5 J. Howard, A.J. Hudspeth, R.D. Vale. 1989. **Movement of microtubles by single kinesin molecules.** *Nature* 342(6246): 154-158.

6 M. Sato, T.Z. Wong, D.T. Brown, R.D. Allen. 1984. **Rheological properties of living cytoplasm: Preliminary investigation of squid axoplasm (Loligo pealei)**. *Cell Motil.* 4:7-23

7 M.A. Tsai, R.S. Frank, R.E. Waugh, 1994. **Passive mechanical behavior of human neutrophils: effect of cytochalasin B**. *Biophys. J.* 66:2166-2172

8 P.A. Valberg, H.A. Feldman, 1987. **Magnetic particle motions within living cells. Measurement of cytoplasmic viscosity and motile assay**. *Biophys. J.* 52:551-69.

9 A.R. Bausch, F. Ziemann, A.A. Boulbitch, K. Jacobsen, E. Sackmann. 1998. **Local measurements of viscoelastic parameters of adherent cell surfaces by magnetic bead microrheometry**. *Biophys. J.* 75:2038-2049.

10 N. Wang, J.P. Butler, D.E. Ingber. 1993.**Mechanotransduction across the cell surface and through the cytoskeleton**. *Science*. 260:1124-1127.

11 R. Ruythooren, E. Beyne, J.P. Celis, J. de Boeck. 2002. **Integrated High Frequency Inductors Using Amorphous Electrodeposited Co-P Core**. *IEEE Trans. On Magnetics* 38:3498-3500

12 M.H. Nayfeh, M.K. Brussel, 1985, **Electricity and magnetism**, chapter 9, *J. Wiley*, New York (NY).

3. Magnetic Tweezers Implementation

3.1. Introduction

In chapter 0 it was concluded that the magnetic part of the tweezers will consist of a microscopic part, consisting of pole tips that create the right magnetic field geometry at the sample area, and a macroscopic part consisting of the magnetic yoke and coils for creating a magnetic circuit and generating flux. An optical microscope system is needed to visualize the experiment to follow the movement of the magnetic probe relative to its surroundings. In this chapter, the fabrication of the pole tips will be described, as well as the macroscopic yoke, electromagnets and amplifier needed to bring the magnetic flux to the pole tips.

3.2. Fabrication of the pole tips

The fabrication of microscopic pole tips that satisfy the design criteria as described in section 3.2.1 appeared not to be straightforward. In the following sections several fabrication methods that were used are described. Finally, in section 3.2.7 a newly developed method is reported that resulted in pole tips satisfying the design criteria.

3.2.1. Design criteria

The constraints resulting from the biological application and the requirement for high field gradient, give the design rules for the magnetic structures.

1. The working area must be optically transparent allowing the use of (fluorescence) microscopy to visualize the experiments.
2. For proper live-cell attachment and biocompatibility in general, a clean surface is required.
3. The poles should have a spacing of 20 μm to produce the highest magnetic gradient while leaving enough space to accommodate a cell.
4. To preserve the desired magnetic field geometry, the magnetic poles have to be firmly attached to the substrate.
5. The magnetic poles should be as high as possible, without obstructing the optical pathway.
6. Magnetic materials to be used should be resistant to aqueous media, have a high magnetic saturation and preferably a low coercive force.

The first two criteria can be satisfied using glass or plastic as a substrate material.

Part of this chapter is based on: A.H. B. de Vries, J.S. Kanger, B.E. Krenn, R. van Driel. 2004. Patterned Electroplating of Micrometer Scale Magnetic Structures on Glass Substrates. Journal Of Microelectromechanical Systems, Vol. 13, No. 3; 391-395

Criterion 4 is extremely important. The very high field gradients that are produced not only exert a force on the tiny magnetic probe, but between the poles as well. Because this force scales with the volume of the object, the forces on the poles are extremely high considering the size. Preliminary test with poles welded at 5 mm from the tip to a common yoke, showed severe lateral oscillation. To preserve the desired geometry, the magnetic poles need to be fixed firmly to the substrate over their entire length.

In order to obtain maximum field gradients, the poles should be at least as high as the spacing between the poles (20 μm) to limit side effects and achieve maximum force (see section 2.6.4). However, the poles should not be so high that there is obstruction of the optical pathway when using a high Numerical Aperture (N.A) objective. With a pole spacing of 20 microns, and a water immersion objective with a high N.A. of typically 1.2, this corresponds to a maximum pole height of 5 micrometre.

The optimal pole height thus depends on whether optical resolution or magnetic force has priority. From the previous chapter we have seen that a 5 μm high pole reaches 30% of the maximum gradient, while a 10 μm high pole achieves 50%. However, where the 5 μm poles would allow an NA of 1.2 for a water immersion objective, the 10μm would reduce the effective N.A. in the direction of the poles to 0.95 (Figure 3.1).

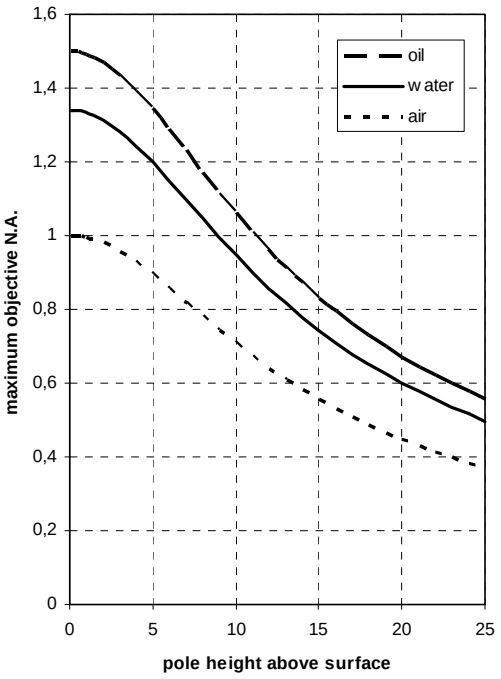

Figure 3.1 Maximum achievable numerical aperture for which the poles are not obstructing the optical pathway.

In the following sections, several fabrication methods will be described and the results will be discussed with respect to the design criteria described above.

3.2.2. Laser cutting from thin sheet.

A straight forward approach for making the pole tips is to cut them from thin sheet of the required magnetic material. The material with the highest magnetic saturation is 50/50 cobalt/iron alloy showing a maximum magnetic saturation of 2.35 T. Commercially available sheets (Vacoflux 50, supplied by VAC vacuumschmelze) have thicknesses down to 50 or 25 μm.

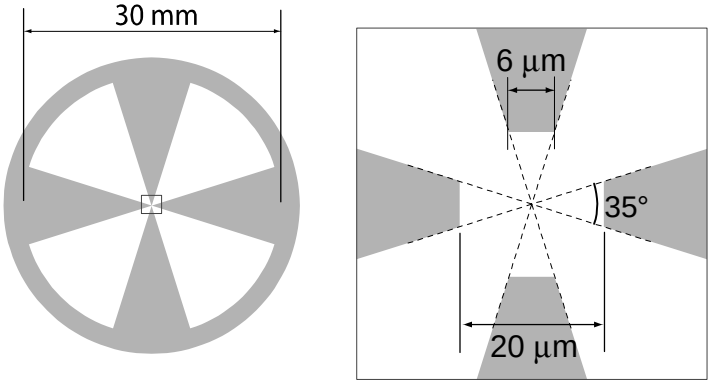

Figure 3.2 Blueprint for cutting poles from sheet material using a laser.

To prevent the pole tips from bending towards each other by magnetic force, they need to be glued to a glass substrate while in the correct position. To avoid having to assemble a set of poles under a microscope, we cut the poles using a CO_2 laser leaving a supporting ring attached to the ends (Figure 3.2). In this way the extremities of the pole tips are spatially fixed, and a glass cover slid (170μm thick, 24mm diameter) can be glued to the pole set. The ring is then removed

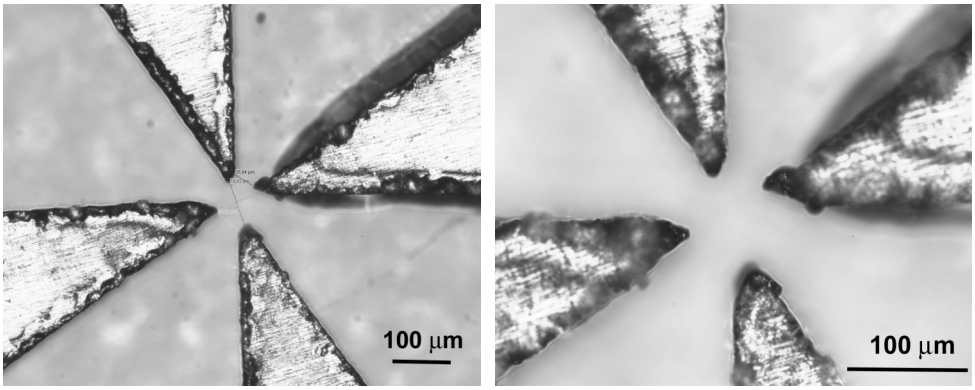

Figure 3.3 Magnetic pole tips produced by laser cutting Vacoflux 50 sheet of 25 μm thickness. The spacing between the pole tips is 100 μm

leaving four isolated pole tips. Figure 3.3 shows typical pole tips produced in this way.

The poles have rough edges, and the tip shapes are ill defined. Furthermore, the tips have very different sizes and shapes, and are at best 30 μm wide. The spacing between the poles is 100 μm, which is almost five times larger than anticipated. The size of the laser spot is 10 μm, but this does not directly translate into a cutting accuracy of the same size. The material properties and the thickness of the sample will also influence the cutting accuracy. Although the cutting laser had been realigned especially to prepare these samples, it turned out to be impossible to achieve smaller tip spacing.

Another problem is the gluing of the poles to the substrate. The cyanoacrylate glue used has a very low consistency, allowing it to form a very thin layer between metal and glass by capillary forces. However, the spreading of the glue is difficult to control, so that typically at the tips of the poles, in the proximity of the other poles, the glue will leak out from under the metal, spreading over the sample area (Figure 3.4). This gives an optically perturbed picture, and raises the cell outside the magnetic field.

The conclusion of these experiments is that the laser cutting that was available to us, cannot reach the desired accuracy. In addition fixating the poles to the glass substrates in a reproducible manner is problematic at best. Furthermore, the thickness control is limited to the sheet thickness that is commercially available. For these reasons, a more flexible technology was chosen: micromachining.

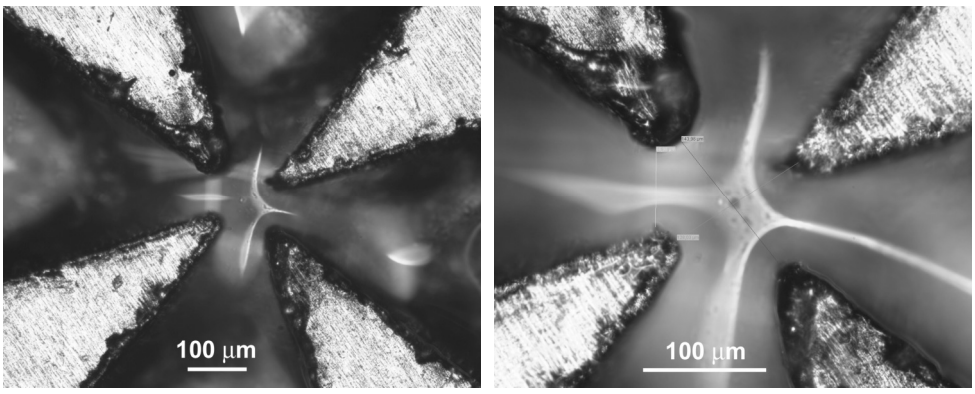

Figure 3.4 Typical problem when gluing tips on the substrate is glue spreading onto the sample area

3.2.3. Micromachining

Deposition techniques

Typical deposition techniques for micro patterning metallic layers include evaporation and sputtering. While well controlled, these techniques are predominantly meant to produce layer thicknesses in the nanometre range, and they are ill-suited to produce layers many micro metres high. For these thicknesses, electroplating will be used.

Electroplating is the process of producing a metallic coating on a surface of on object by the action of electric current. The deposition of the coating is achieved by negatively charging the object to be coated and immersing it into a solution which contains a salt of the metal to be deposited. In other words, the object to be plated is made the cathode of an electrolytic cell. The metal ions of the salt are positively charged and are thus attracted to the object. The negatively charged object provides electrons to reduce the ions to metallic form. In its simplest form the reaction of a metal salt *M* in aqueous medium at the cathode follows the equation:

$$M^{n+} + n\,e^{-} \Rightarrow M \tag{3.1}$$

In case the object to be electroplated is not metallic, first a thin conductive 'seed layer' is applied, on which electroplating can take place. In our case, a glass substrate would require the use of such a seed layer.

The anode material can be the metal to be deposited, in which case the electrode reaction is simply the opposite of the cathode reaction, and metal ions are continuously supplied.
Alternatively, the anode can be an inert material and the anodic reaction is oxygen evolution. In this case, the plating solution will eventually be depleted of metal ions.

Micro patterning using electroplating

While electroplating is normally done on complete unobstructed surfaces, it can also be grown in a pattern using '*through mask*' deposition. [1] With this method, a removable mask is applied over a seed-layer that restricts the plating process to the desired pattern. The height that can be achieved depends on the type of photo resist used and ranges from 0.4µm to 12µm for removable resists, up to 40µm to 260 µm for the epoxy type photo resist (SU 8-2100 MicroChem). Such a patterned mask can lead to a non-uniform current distribution, and thus to non-linear grow speed and consequently height (see Figure 3.5).

IBM developed a variation on this procedure called '*Damascene'*. In this case, a dielectric is first patterned with a resist layer, after which a seed-layer is deposited. The subsequent electro deposition is carried on until the grown layer completely overfills the whole mask. Then a planarization step is introduced, which removes all the deposited material above the mask, leaving only the small structures. A big advantage is the uniform height of all the electroplated structures, but it is a very complicated process [1,2,3]

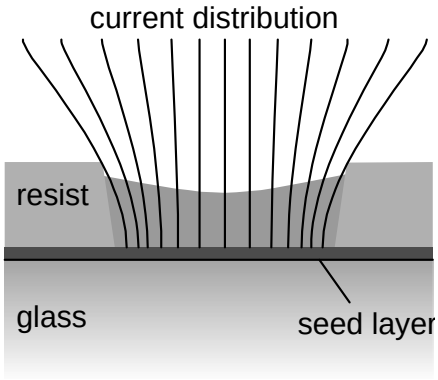

Figure 3.5 'Through mask' electroplating can lead to non-uniform current distribution, producing electroplated structures of uneven height.

Electroless plating

An alternative electro deposition technique is electroless plating. Here the seed layer and deposited material function as a catalyst for the electrochemical reactions. There is no power supply or electrode necessary, as the required electron supply comes from the bath itself. Electroless plating has the advantage over electroplating, that it produces layers of uniform thickness when plated through a mask. Electroless plating is, however, an extremely slow process, (typically one micrometre per hour) which makes it rather cumbersome for the fabrication of high structures, while also requiring very high chemical stability of the mask to be used.

3.2.4. Magnetic Material for electroplating

Electroplating alloys is quite complicated, because of the different potentials of the metals. Therefore, we will not use the magnetically optimal 50/50 Co-Fe alloy, but start producing poles that consist of a single metal. Iron has the highest saturation magnetisation at 2.1 T, but is ill suited in a biological environment because of the high corrosion. Cobalt has the second highest saturation magnetisation at 1.85 T. It is much more corrosion resistant, and extremely hard, and therefore a good choice for the poles.
The simulations in the previous chapter were also performed using the saturation magnetisation of cobalt.

From the considerations above, it was decided to use micro patterned electroplating of cobalt poles on glass substrates. In the next sections (3.2.5

through 3.2.7) results obtained by different procedures for this patterning are described.

3.2.5. 'Through mask' electroplating

Procedure

The first micron scale magnetic poles were manufactured using 'through mask' electroplating. Starting from glass substrates, after which a patterning mask applied, the magnetic material is deposited using electroplating to produce the proper geometry. Figure 3.6 shows the complete procedure. Because glass has a high electrical resistance, first a thin conducting seed layer is deposited (b). Then the patterning mask is applied (c) and the poles are electroplated through this mask (d), after which the resist mask (e) and seed layer can be removed (f).

Seed layer deposition

Standard microscope cover slides (Menzel-Gläser 170 μm thickness, 24 mm diameter) were rinsed with ethanol followed by a 5 minutes treatment in oxygen plasma (Nanotech plasmaprep 100). Then the electroplating seed layer is deposited. Copper is generally considered the preferred material for a seed layer. Like most metals, it does not adhere well to glass, and thus an additional adhesion layer of titanium or chromium is required. Sputtering is performed in a custom-built apparatus (UT-Sputterke) at a background pressure of 2×10^{-7} mbar, using argon at 6.6×10^{-3} mbar as sputter gas. First, a 10 nm titanium layer is deposited, followed by a 200 nm layer of copper. (Figure 3.6b)

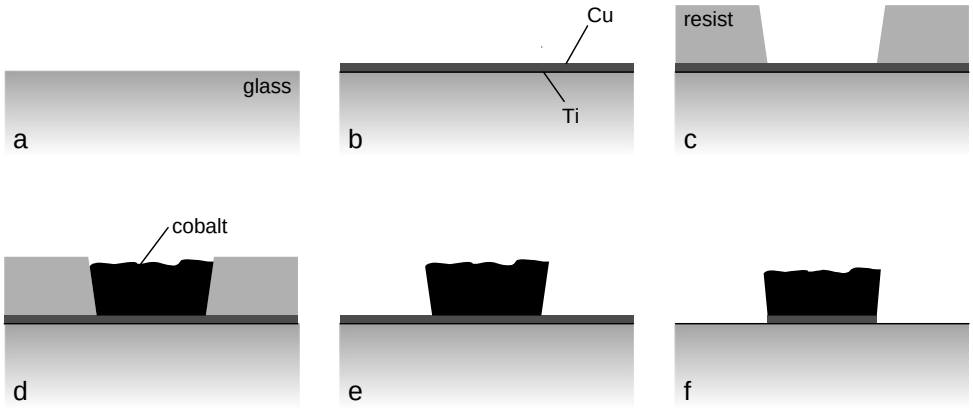

Figure 3.6 Through mask electroplating of cobalt poles. A copper seed layer (with titanium adhesion layer) is deposited on a microscope glass substrate. The photoresist mask is deposited and developed, after which the cobalt can be electroplated on the exposed seedlayer. After the photoresist has been removed, the copper is etched away.

Micro pattern Mask

The mask for the poles is applied using photolithography. Standard HMDS procedure is used to remove adsorbed water from the substrate surface. Next, Olin-908/35 positive resist is spin-coated at 3000 rpm for 20 seconds producing a 4.5 μm thick layer. The resist is soft-baked at 95°C for 5 minutes to remove the solvents. Exposure is performed using a Karl Süss Mask aligner MA55 (UV source rated at 9 mW/cm^2) for 22 seconds.

Normally this is followed by a hard-bake at 120°C for 5 minutes after which the photo resist is developed. However, with these very thin samples, an immediate hard-bake is too rough causing nitrogen, generated during the exposure, to develop gas bubbles in the resist affecting the accuracy of the lithography process. This is solved by either, starting the hard-bake at 70°C and gradually (10°C/min) increasing the temperature to 120°C, or adding a delay time of 10 to 20 minutes before the hard-bake, to let the nitrogen diffuse out of the exposed resist. The resist is then developed for a total of 75 seconds.

Figure 3.7 shows the developed photo resist mask at this point in the procedure. Comparing the top and bottom images shows that the walls are not completely straight, but have a slight slope. The distance between the opposing poles at the top is 19.5 μm and at the bottom 22.5 μm. This means that the walls have a 12° slope, which is typical for the positive resist used here. This is not a problem for the functioning of the magnetic poles.

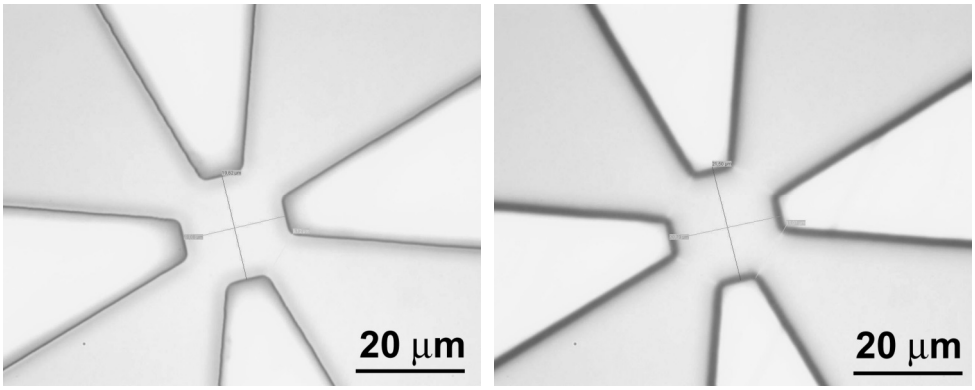

Figure 3.7 Microscope images of the developed photo resist mask, focused on the top (left) and the bottom of the resist layer (right). The edges show a slight slope, typical for this type of resist.

Electroplating the poles

At this point, we have a glass substrate with the electroplating seed layer, covered by a patterned photo resist mask (Figure 3.6c). The magnetic structures can now be grown on the exposed parts of the seed layers. The electroplating bath used for these samples is an aqueous solution that consists of 60 g/l $CoCl_2 \cdot 6H_2O$ supplying the cobalt ions and 3.5 g/l SDS to lower the surface tension, and thus prevent pitting. The anode is a cobalt rod of 99.9% purity. Standard electroplating bath conditions (pH 3.5, temperature 60°C) [4] were used.

To achieve a good bonding of the cobalt to the copper it is important to have a clean surface. With a copper seed layer, this can be achieved by reverse-plating for several seconds just prior to the electroplating. This simply means supplying a reversed current, thereby dissolving the upper layer of copper atoms, creating a fresh clean copper layer for the subsequent electroplating of the cobalt.

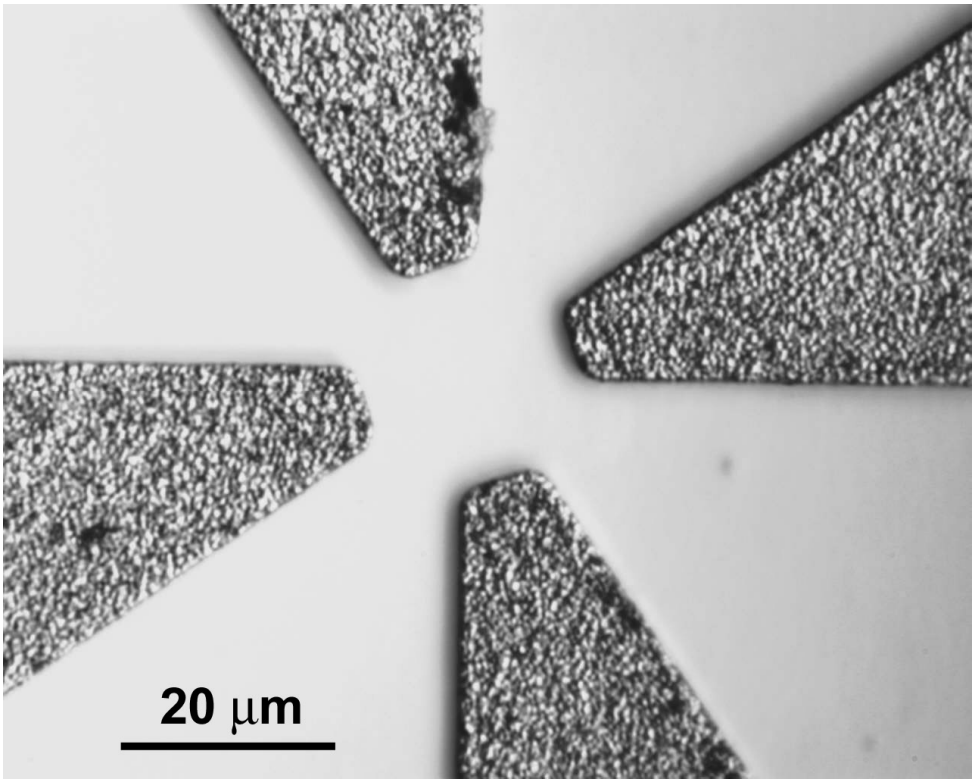

Figure 3.8 Electroplated cobalt layer directly after the photo resist has been removed. The poles show a grain structure typical for electroplated material.

A current density of 25 mA/cm^2 was found to produce optimal cobalt layers, yielding a grow speed of 0.6 µm per minute. Lower current densities leave more time for recontamination of the surface, producing a partial blockage of the electroplating process. Higher current densities produce hydrogen gas bubbles at the cathode, resulting in pitting (tiny holes in the cobalt layer) due to hydrogen bubbles sticking at the surface. Figure 3.8 shows electroplated cobalt poles produced with this procedure. The poles have nicely filled the mask, and show neither gaps, nor pitting. The surface shows a grain structure with a roughness of 500nm, which is typical for materials electroplated under these conditions [4].

Removal of mask and seed layer

After electroplating the cobalt layer, the photo resist layer is washed off using acetone.

To complete the pole set, only the copper seed layer needs to be removed to produce a transparent sample. An etching solution consisting of hydrochloric acid and hydrogen peroxide (1: HCl 37%, 1: H_2O_2 30%, 6: H_2O) is used. It etches both cobalt and copper at comparable speed, but as the copper layer is thin compared to the cobalt layer, the process can simply be stopped when the copper is completely gone. The acid concentration is adjusted to provide a 20 second etching time to remove the 200 nm copper layer, providing enough time to remove the substrate from the solution and rinse it before affecting the cobalt layer too much. The titanium layer cannot be etched away, but at 10nm thickness, it is still optically transparent.

Internal stress

When increasing the height of the electroplated structures, internal stress was apparent at heights above one micrometre. Frequently the poles would lift from the surface, and even curl up completely. This was solved by adding a high concentration of boric acid (60 g/l H_3BO_3) to the electroplating bath (while keeping the pH at 3.5). Boric acid had been added to prevent pitting and to control the properties of the cobalt layer but showed the unexpected side effect of drastically lowering

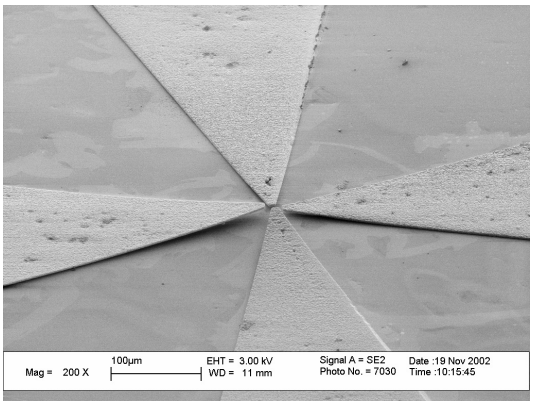

Figure 3.9 Example of high internal stress leading to lifting of the pole tips.

stress of the plated cobalt layers. The pH, temperature and boric acid concentration can be varied to change the phase composition (and thus magnetic properties) of the electroplated cobalt layer [5]. (See section 4.2.2 for analysis of the magnetic properties of the cobalt layers)

Discussion

Producing the poles with micromachining shows a very big improvement to the earlier macroscopic methods. The electroplated poles have the desired accuracy and spacing. They show a very well defined shape, and are easily reproducible. Furthermore the poles are fixed well to the glass substrate right until the tips. These results are indeed very encouraging; therefore micromachining is chosen to manufacture the magnetic pole substrates.

Before this method for producing the poles can be used in biological experiments, some problems have to be solved though:
While most of the copper seed layer is etched away, there is of course still the layer underneath the cobalt poles. At the side of the poles therefore, a small band of copper is exposed, enabling copper ions to dissolve into the surrounding medium. This appeared to be severe enough to poison cells. While copper poisoning is very well know it was not expected that this small exposure would have such a dramatic effect [6].
The titanium layer is giving both biological and technical difficulties. The titanium is inhibiting cell adhesion to the surface of the glass substrate. Further, it also gives problems in detecting fluorescence in the microscope. Fluorescent particles that were clearly visible on a normal glass substrate were completely invisible when placed on the titanium coated substrates. The transmission of the titanium layer was measured to be between 38 tot 40% for wavelengths of 400 to 700 nm.
To solve these problems, the copper seed layer needs to be replaced by a more biocompatible material. The most likely candidate would be platinum. At the same time, the titanium adhesion layer needs to be removed from the glass surface. Removing the titanium at the end of the process is difficult. Titanium is very hard to etch, and all possible etching solutions will etch cobalt or glass much faster.

In order to circumvent these problems, an alternative procedure using a lift-off mask is used. In this way, there is no direct contact between the seed layer and the glass in areas not covered by the poles.

3.2.6. Electroplating using a Lift-off mask

The so-called 'lift-off' technique avoids the need to etch the seed layer after electroplating the cobalt poles, by patterning the seed layer before electroplating the magnetic structures (Figure 3.10). Two separate patterned masks are applied to the substrate during the complete process. These masks need to be aligned at

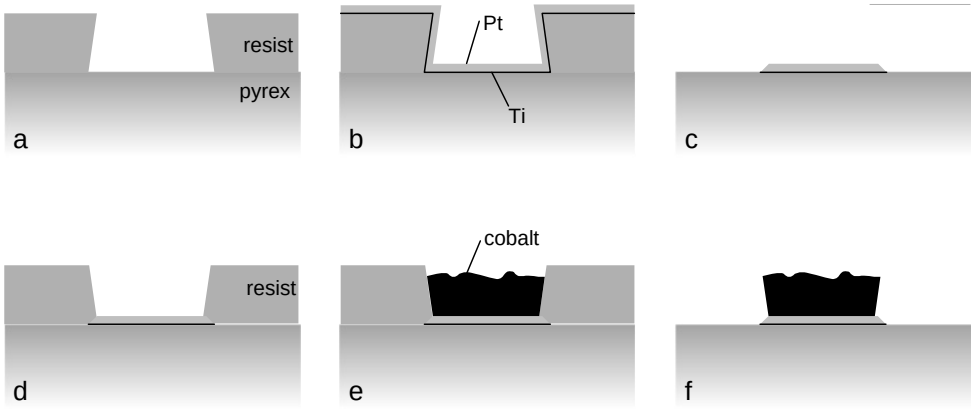

Figure 3.10 Lift-off technique: A patterned mask is applied on the glass substrate(a). The deposition of the seed layer takes place through this mask (b). The excess seed layer on top of the mask is lifted off the substrate when removing this mask, leaving a patterned seed layer (c). A new mask is applied through which the electroplating can takes place(e).

micrometre accuracy by the mask aligner. To do this, two alignment areas are needed at the sample, requiring the use of 3" or 4" glass wafers. Several pole structures are produced on one wafer, and are later separated by sawing.
The glass wafer (Pyrex) is cleaned similar to the previous method using ethanol and oxygen plasma. A photo resist mask is then applied to the glass substrate before the deposition of the seed layer. To ease the lift-off process, this resist needs an overhang creating a 'shadow' underneath (Figure 3.10a), minimizing the sidewall thickness of the seed layer deposited afterwards. Ideally, the seed layer does not coat the wall at all, but that depends on directionality of the deposition process. Evaporation is better suited than sputtering in this respect.

The overhang of the resist is created using Olin Ti-35ES image reversal resist (Figure 3.11). The resist is spin-coated for 40 seconds at 3000 rpm creating a 3.5 μm thick layer, and baked for 5 minutes at 95°C to remove the solvents. The resist is then exposed for 18 seconds using an inverted mask, i.e. the parts of the resist that need to remain are exposed (a). A delay time of 20 minutes is needed to let the nitrogen diffuse out of the exposed resist. At this point, the resist is still behaving like normal positive resist, and can be developed as such (b). The 'image reversal' is performed by baking the resist at 120°C for 5 minutes, cross-

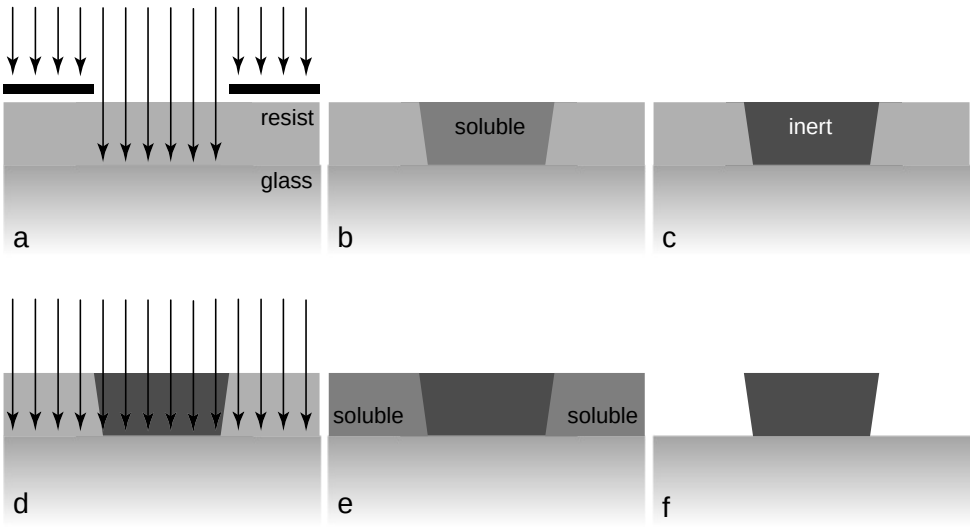

Figure 3.11 Image reversal resist. The resist is exposed using an inverted mask (a). At this point, the resist behaves like normal positive resist with the typical positive sidewalls (b). The 'reversal bake' cross-links the exposed area while the unexposed area remains photoactive (c). Using a flood exposure without mask (d) the remaining resist is made soluble in developer (e). After developing the area's exposed in the first step remain with the desired undercut.

linking the exposed area, making it insoluble in the developer (c). The resist is now exposed without a mask (flood exposure) for 45 seconds (d) to make the remaining resist soluble to the developer. This resist is developed for a total of 90 seconds, and only the cross-linked areas remain.

Next, the electroplating seed layer is deposited. First, a 10 nm titanium adhesion layer is sputtered, followed by a 200 nm layer of platinum (Figure 3.10b). Platinum was used instead of copper, for biocompatibility reasons. The lift-off of the resist and surplus seed layer is performed by rinsing with acetone, and optionally ultrasonic cleaning, leaving a patterned seed layer on the wafer.

From this point, the procedure is similar to 'through mask' electroplating. A new mask is applied, followed by the electroplating of the cobalt poles through this mask, as described previously on page 46 to 47. Using platinum in stead of copper does introduce a change to the surface cleaning prior to plating. Due to the different electrochemical properties, platinum cannot be reverse plated. Therefore, a different method was used. Just before plating, the wafer is treated in oxygen plasma for 30 seconds, which is sufficient to clean the surface. This treatment also strips 500 nm of photo resist, which is tolerable.

Electroplating using a patterned seed layer does introduce a very big problem though. The patterned seed layer consists of the areas where the poles will be electroplated, and of lines connecting these areas to the power supply (Figure 3.12). The final photo resist mask restricts plating the pole areas only. Because the seed layer is very thin, the electrical resistance of the layer is quite high. The electrical resistance measured from one side of the wafer to the opposite side was 30 Ω. The pole structures have an extremely high aspect ratio. While the tips are only 8 μm wide and 20 μm apart, the total triangle composing one pole is 1.3 cm in length. The supply lines connecting opposing poles are some 5 cm. Because of these distances, the resistance between opposing poles can reach 15 Ω. With an electroplating current density of 25 mA/cm^2 this means that voltage differences in the same order as the electroplating voltage appear.

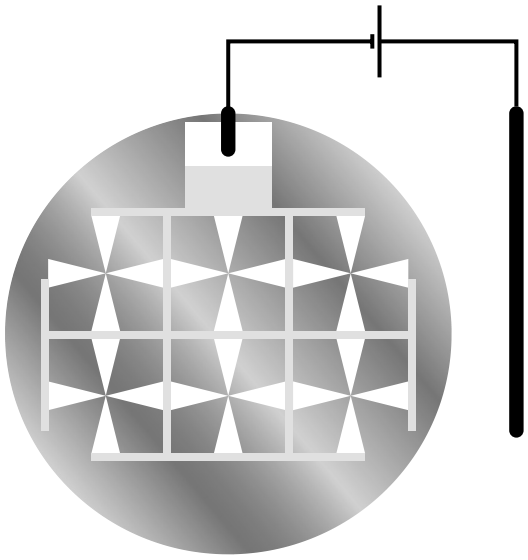

Figure 3.12 Schema of electroplating using patterned seed layer. Six fore-pole structures are shown. Connecting lines supply electrons from the power supply.

Figure 3.13 shows the result of these voltage differences. The resulting electroplating deposition speed differed by two orders of magnitude over the complete pole set, meaning that the pole closest to the power supply grew extremely high, while the opposite pole is hardly plating at all. The left and right poles had symmetric supply lines, and therefore have equal deposition speed.

The ‘through mask’ electroplating procedure did not show this problem for two reasons. First, because the complete substrate was covered with a seed layer, the cross area of the ‘supply line’ is greatly increased, lowering the electrical resistance drastically. Secondly, because the seed layer extended between the poles, the connection between them was very short, nullifying the voltage difference between opposing poles. While a small global deposition speed difference was observed for ‘through mask’ deposition (less than 25%), the local difference at the pole tips was non-existing.
This problem could be solved by developing a method that combines the advantages of the ‘lift-off’ and the ‘through mask’ techniques.

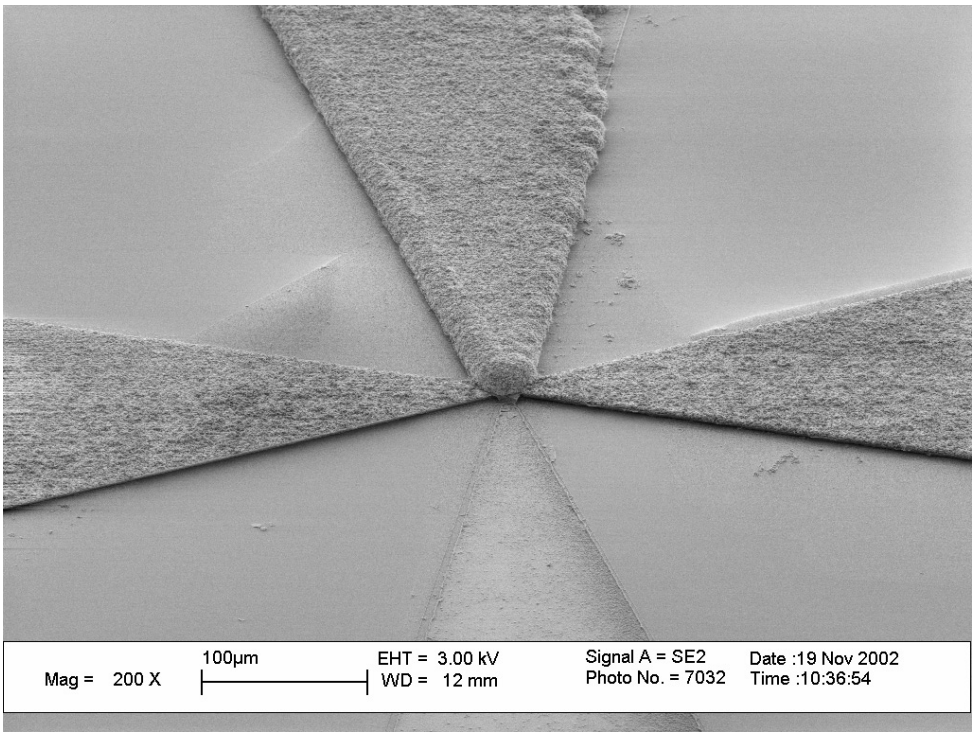

Figure 3.13 Variation in electroplating deposition speed on the seperate poles due to ohmic resistance differences. (SEM image)

3.2.7. Delayed lift-off electroplating

To solve the problem of deposition speed differences, a completely new procedure for patterned electroplating had to be developed. The advantages of lift-off have to be combined with those of 'through mask' electroplating. The developed procedure is a variation on normal lift-off, where the lift-off step is not performed after the seed layer deposition, but as the last step of the complete procedure. Hence the name: 'delayed lift-off electroplating'.

Figure 3.14 illustrates the important steps in the 'delayed lift-off electroplating' procedure. The first two steps are similar to normal lift-off described on page 50. First a patterned lift-off mask (Olin Ti-35ES, 3.5 µm thickness) is applied on the glass substrate (a) and then the 10 nm titanium adhesion layer, and 200 nm platinum seed-layer are sputtered (b). In contrast to normal lift-off, the resist and surplus seed-layer is not removed! The second mask of positive resist (Olin 908/35, 5 µm thickness) is applied on top of the seed layer and lift-off resist.

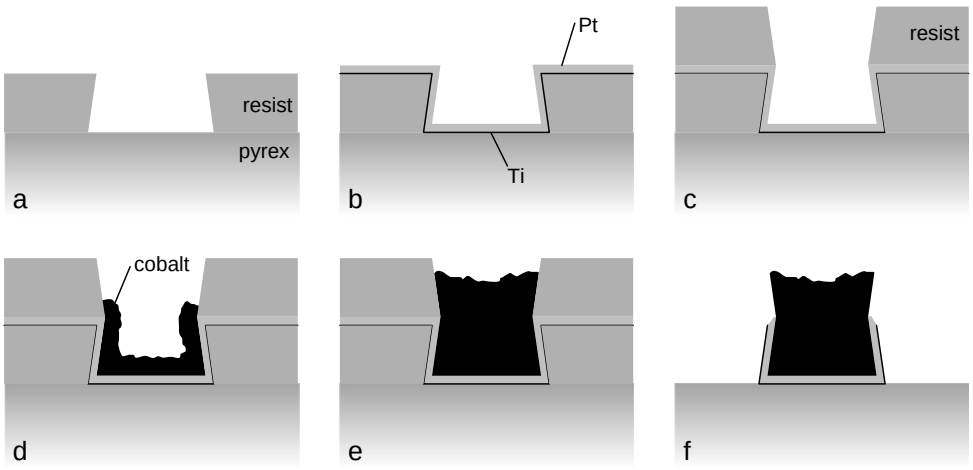

Figure 3.14 'Delayed lift-off' electroplating. This is a variation of the traditional lift-off technique. In stead of performing the lift-off directly after deposition of the seed layer, the lift-off is performed as the last step in the procedure. This ensures that the seed layer is continuous over the complete wafer, while still restricting electroplating to the pole area.

Because the sputtering also coated the wall of the lift-off resist, the wafer has a continuous seed-layer over the whole area, eliminating the problems of potential differences during electroplating. The second resist mask restricts the electroplating to the pole areas (Figure 3.14c).

Before the prepared wafer is electroplated, the surface needs to be cleaned. As noted before, reverse plating is not possible for platinum, so oxygen plasma cleaning is used. Care should be taken to keep the wafer very cool, as the sandwich of photo resist, seed layer and photo resist is prone to crackle when exposed to more than 60°C. Especially the seed layer at the edges of the lift-off resist will break off, destroying the homogeneity of the seed layer. Therefore, oxygen plasma cleaning was performed in the 'Tepla 300E' at low power (250W) for 1 minute. This ensured sufficient low substrate temperature, while still cleaning the surface adequately for the plating process.

The cobalt structures are now electroplated. Due to the presence of the seed layer at the side walls of the first resist layer, a typical cup structure will be produced for thin layers (Figure 3.14d). This effect decreases when the layer grows thicker, or when the sidewalls are close to each other (e). For our purposes, only the pole extremities are interesting. At that point, this cup shape will not be prominent. If it ever does become a problem, the cup effect can be circumvented by having the second resist layer slightly overlap the first layer, thereby also coating the sidewalls.

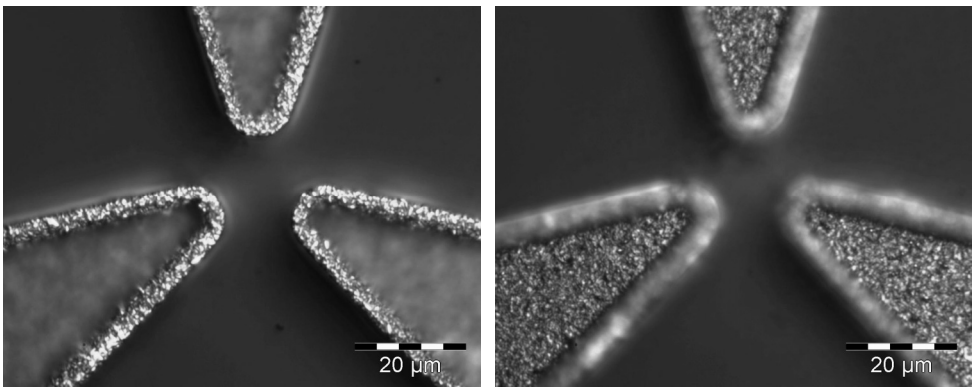

Figure 3.15 Cobalt poles produced with 'delayed lift-off' electroplating. These specific poles are only 4µm thick, and thus show the cup like features. The image on the left is focused on the top of the cup edges, while the image on the right is focused on the bulk of the poles. The cup edges do not interfere with the magnetic field, and these poles are therefore well suited to our experiments

At the last step in the procedure, the lift-off is finally performed (Figure 3.14f).The wafer is submerged in acetone, and placed in an ultrasonic bath to remove the excess seed layer and photo resist. As a result, we now are left with freestanding cobalt structures, while the glass around the structure is untouched, and has only been in contact with the photo resist.

Figure 3.15 shows microscope images of typical three-pole structures produced in this way. The poles were relatively thin (4 µm), and therefore show the cup features discussed earlier. The poles show very well defined shapes and are very reproducible.

The ‘delayed lift-off’ methods allows for more freedom in creating micro structures than traditional electroplating methods. Because the electro plating current is fed by a temporary seed-layer, structures can be made that are completely free-standing, devoid of current supply lines. Figure 3.16 illustrates the versatility of the method by electroplating the name of our institute in micron scale structures. The characters are cobalt structures of 4 µm height, free standing on a glass substrate. The lines composing the characters are only 11 µm wide.

Figure 3.16 Light microscopy image (in reflection), showing the versatility of the described delayed lift-off method. The electroplated cobalt structures shown are composed of lines of 11µm width, and have a thickness of 6 µm. The area surrounding the structures is bare glass. For very small enclosed structures, it can be difficult to remove the resist and seed layer. This can be seen in the letter 'B' where the platinum seed layer is still present, which creates the strong reflection.

With the increased flexibility offered by 'delayed electroplating' procedure, it was also possible to produce an array of free standing three-poles, as discussed in section 2.6.5.
Figure 3.17 shows a pole array produced using 'delayed electroplating'. The total array spans an area of 2 cm by 1.7 cm, consisting of thousand of poles. The overview clearly illustrates the high reproducibility of the poles. Figure 3.18 is a detail of the previous image, showing the resolution and uniformity of the individual poles in the array.

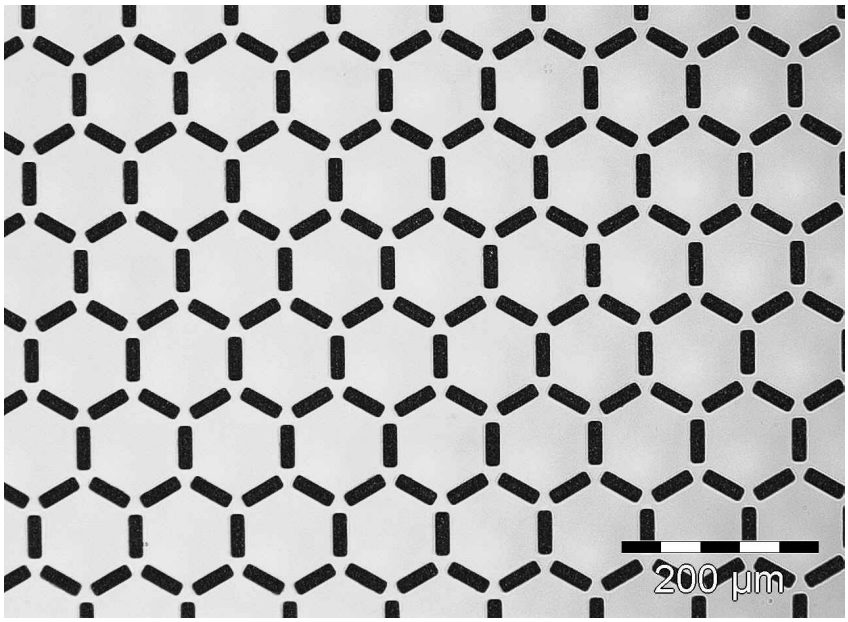

Figure 3.17 array of three-poles; overview

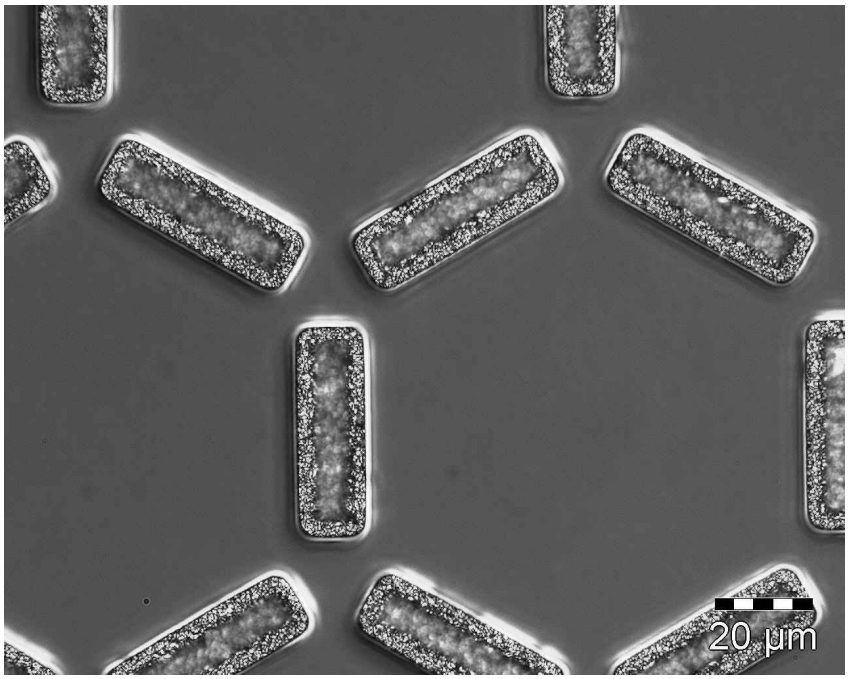

Figure 3.18 Detail from array of three-poles. The individual bars are 14x42 µm

3.2.8. Biological Aspects

One of the methods of bringing a cell between the magnetic poles is to culture cells directly on the substrate, and then using the cell that happens to be in the centre of the pole structure. While the pole structures were designed to be as biocompatible as possible, growing cells directly on the pole substrates turned out to be unsatisfactory (Figure 3.28a). The cobalt has a negative influence on cell growth, but also cells adhere less to processed glass substrate, apparently due to slight changes in the surface properties

Therefore the substrates need to be modified. This was accomplished by coating the poles with a biocompatible polymer. Poly(glycolic)acid (PGA) and poly(D,L-lactide) (PLA) and their associated copolymers are perhaps the most common biodegradable synthetic polymers known and have been used in drug delivery,

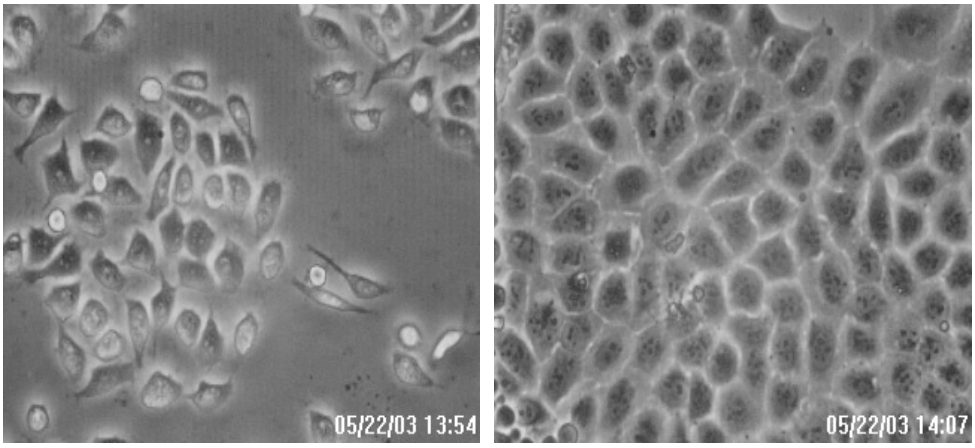

Figure 3.19 Culturing cells directly on the magnetic tweezers substrate (a) and using a poly(D,L-lactide) coating (b).

bone osteosynthesis and tissue engineering of skin[7]. For our substrate poly(D,L-lactide) was used. It is in-home synthesized; giving well defined physical and chemical properties. PLA is amorphous, with a T_g of approximately 55-60°C, thus transparent and able to withstand cell culturing conditions (37°C). It is sterilisable (ethanol 70%) and hydrophobic, and easy to process either by solving (spin-coating) or thermal melting. Because it has a high molecular weight, low concentrations can be used in spin-coating, making very thin layers possible.

The polymer is dissolved in acetone and deposited using spin coating. The thickness of the deposited layer is controlled by choosing the proper polymer

concentration in the solution and the rotation speed during spinning. After the surface is coated with PLA, there is no need for any post treatment for culturing cells. Using a spin speed of 4000 rpm, a 1% solution of PLA in acetone produced a 100 nm to 150 nm layer thicknesses, while a 2.5% solution yielded layers between 200 and 300 nm.

Figure 3.19 shows the results of a cell culturing experiment of a non-treated (a) and a PLA coated (b) substrate. HeLa-Histone2B-GFP cells were grown on both substrates in a 5% CO_2 atmosphere in DMEM with 0.35 g/l G418, 4.5 g/l glucose, 2 mM L-glutamine, 3.7 g/l sodium bicarbonate and phenol red, supplemented with 10% fetal calf serum and 100 units/ml of penicillin, 100 µg/ml of streptomycin and 0.25 µg/ml of amphotericin B. Clearly the coated substrate shows good cell viability in contrast with the non-treated control.

At this stage the developed poles satisfy all the design criteria as given in section 2.3.1. The experiments described in chapters 3.7 and 4.5 have been performed using poles fabricated with the 'delayed lift-off' procedure. Next, aspects of the experimental setup required to use the micron scale magnetic poles are described.

3.3. Optics

3.3.1. Introduction

In the previous chapters, it has been explained that a magnetic tweezers is not a stable trap, and will therefore need an active feedback system to control the movement of the probe. This means the tweezers setup needs to include a way to track the position of the probe, and use that as an input signal for the feedback system.

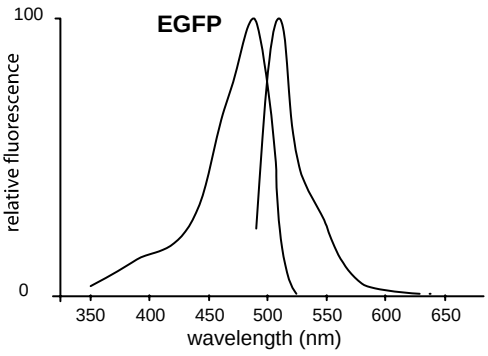

Figure 3.20 The excitation and emission spectra of EGFP

3.3.2. Setup

The optical setup consists of two pathways. A white light and fluorescence path is used for visualizing the labelled cell components, and an optional laser interference pathway used for bead tracking in case video tracking is unsatisfactory.

Criteria fluorescence pathway:

- Filters optimized for EGFP and possible second fluorophore
- Emission pathway transmission as high as possible

Criteria laser tracking

- Two high-NA objectives in transmission
- Movement of sample relative to laser focus

3.3.3. Fluorescence pathway

In comparison to other dyes, EGFP has excitation (488 nm) and emission (507 nm) maxima relatively close to each other (Figure 3.20). This means that the dichroic mirror that separates the fluorescence light from the illumination light needs a steep transition from transmission to reflection. The Q495 LP (Chroma Technology corp, Brattleboro USA) with a transmission of 8 % at 488 nm and 90 % at 507 nm and higher wavelengths is selected for this component (Figure 3.21, mirror: DM2).

An argon laser (Ion Laser Technology) tuned to the 488 nm Ar laser line is used for illumination. To remove the plasma lines from the argon laser a laser line filter is used: 488 NB3 (Omega Optical Inc., Brattleboro, USA) with a centre wavelength of 488 nm, FWHM 3 nm, Transmission > 80 %. The beam from the laser is expanded, and then it is focused on the backplane of the objective to produce a homogenous illumination at the sample plane.

To couple the light into and out of the objective, dichroic mirror DM1 (Figure 3.21) is used, which separates the fluorescence and laser interference tracking pathways.
This dichroic mirror is a long pass filter with an experimentally determined transmission of around 65 % at high wavelengths, starting from 520 nm. This is sufficient for current purposes, but a higher cut-off wavelength is needed when broader bandwidths and/or more colours are introduced.

The emission filter is chosen as a band pass filter instead of a long pass filter, so that a possible extra fluorescence colour can be added in the future. Considering the emission spectrum of eGFP a filter with a transmission range between 500-550 nm is used. The selected filter is the HQ525/50m (Chroma Technology corp., Brattleboro, USA). It has a specified transmission of 10^{-5} at 488 nm. A second fluorescence colour can be introduced in the set-up by replacing the emission filter with one that transmits the range 550-600 nm, provided that the dichroic mirror DM1 that couples light into and out of the objective is also replaced with a long-pass filter with higher cut-off frequency.

The fluorescence detector is an image intensified CCD camera (Hamamatsu C2400-77 camera with Hamamatsu C2400-80 image intensifier).

Due to the limited detection angle, the objective with N.A. 1.2 collects 28% of the emitted fluorescence light based. The total transmission through the objective and other optical components is 29.5%, giving a total detection efficiency of 8%, which is typical for this kind of setup [8].

3.3.4. Laser interference tracking pathway

The laser tracking pathway was based upon an existing optical trap bead tracking setup. It includes water-immersion (100 ×, NA 1.2-0.45, Planachromat, Leica) for projecting the laser focus and an oil-immersion (100 ×, NA 1.25, Leica) objective lens to collect the beam. The sample in between the objective is mounted on a piezo tube that can move in three directions relative to the objectives.
The set-up incorporated a 200 mW IR laser diode (830 nm) and a 10 mW HeNe laser (633 nm) as light sources for the optical trap. The laser diode produces a divergent elliptical beam, with strong astigmatism, which needs a set of prisms and a lens at an angle to the optical axis to produce a somewhat reasonable beam. Compared to this beam, the HeNe laser gives a nearly perfect parallel beam that only needs a simple beam expander to match the entrance of the objective.

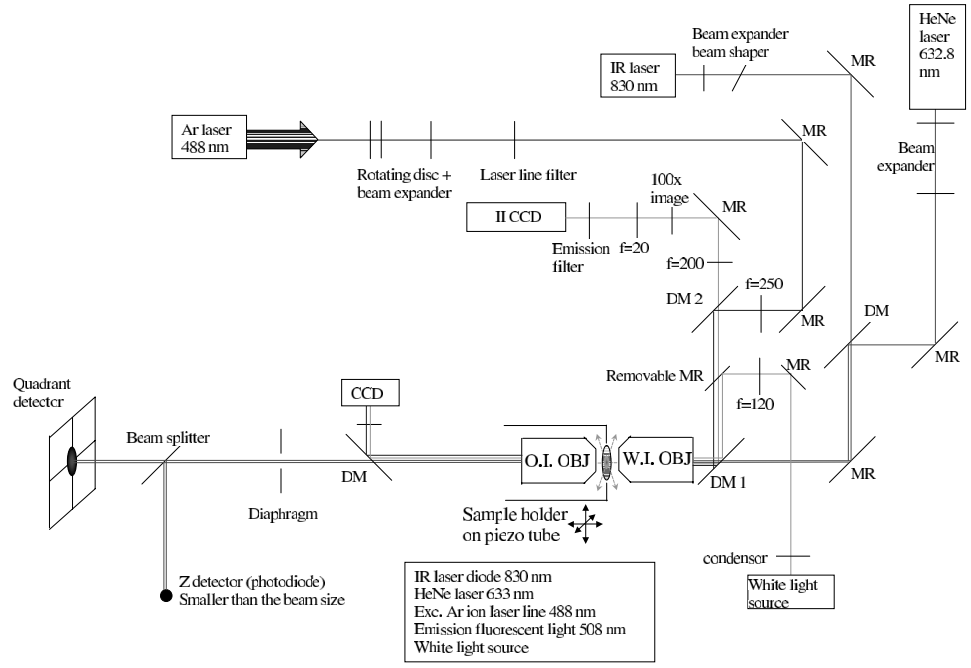

Figure 3.21 Magnetic tweezers optical pathway. The setup includes an epi-fluorescence pathway (Ar laser and II-CCD) for selectively visualizing features of the cell environment, and a laser interference bead tracking pathway (IR or HeNe laser, and quadrant detector+photodiode)

Therefore the HeNe laser is far better suited for tracking purposes, while the IR laser diode would only be used when higher wavelength and/or power is called for (i.e. in an optical tweezers experiment).
Both lasers are combined using a dichroic mirror with 645 nm cut-off wavelength. The mirror are IR optimized 10D10BD2 (Chroma Technology corp, Brattleboro USA) with a reflectivity of >99% between 700 and 950 nm, and including a high reflectance for the 633 nm HeNe laser line.
The lasers are transmitted through the DM1 beam splitter, and focused by the water immersion objective onto the probe. The resulting beam is collected by the oil immersion objective. A 50/50 cube beam splitter transfers the light towards a quadrant detector and photodiode for lateral and axial detection.
An optional white light source can be included into the setup, in place of the fluorescence light source using a removable mirror. The transmitted light is coupled out of the laser tracking pathway by an extra dichroic mirror, and imaged on a CCD camera.

3.3.5. Discussion

A major difference between fluorescence and white light microscopy on the one side, and the laser interference tracking on the other side, is speed. The timescale estimate indicated that the feedback system needs a kHz bandwidth. Clearly, only laser interference tracking can supply that speed. Unfortunately, the laser tracking is also by far the most complicated system. Not only does it need an extra optical pathway, it also requires an extra feedback to keep the laser focus on the probe. Both other methods only require that a video camera be added to the microscope. Although the current setup has both options available, for the experiments described in this thesis only video microscopy is used for particle tracking.

3.4. Macroscopic yoke

The flux needed for the magnetic tweezers is produced by macroscopic electromagnets that are located relatively far away from the pole tips. A magnet circuit is needed to guide flux to and from the pole tips and electromagnets. In the following sections, the theory of magnetic circuits will be recalled, and then used to describe the various models used to calculate the required flux generated at the electromagnets. This is then used to design the coils and electronics needed to drive the magnetic tweezers.

3.4.1. Magnetic circuits

Magnetic flux lines form closed loops. If the magnetic flux in a system is confined to a well-defined path, we can describe it as a magnetic circuit that is very similar to an electric circuit.
From the application of Ampere's circuital law to a path *l* following the magnetic circuit we get [9]:

$$\oint H\, dl = N I \tag{3.2}$$

With a coil in the circuit of *N* windings carrying a current *I*.
Substituting $B = \mu H$ and $\Phi = BA$, with μ the magnetic permeability and *A* the cross-sectional area of the circuit at the point of consideration, produces the basic magnetic circuit equation:

$$\Phi \oint \frac{dl}{\mu A} = N I \tag{3.3}$$

Dealing with a circuit, the flux is essentially constant at all points of the circuit, which allowed taking Φ outside the integral.
Defining the magnetomotive force $\mathscr{F}$ as:

$$\mathscr{F} = N I \tag{3.4}$$

And the reluctance $\mathscr{R}$:

$$\mathscr{R} = \oint \frac{dl}{\mu A} \tag{3.5}$$

We can write (3.3) as:

$$\mathscr{F} = \Phi\, \mathscr{R} \tag{3.6}$$

Which is similar to Ohm's law for electrical circuits:

$$V = I\ R \tag{3.7}$$

The electrical basic quantities of potential *V*, current *I* and resistance *R* are thus equivalent to the magnetomotive force $\mathscr{F}$, magnetic flux Φ and reluctance $\mathscr{R}$. (Table 3.1)

Reluctances can also be added in the same way as electrical resistance. There is however a difference in the order of magnitude of the variables. In an electric circuit the surrounding air around the conductors can generally be neglected. In a magnetic case, this is not often the case.

Table 3.1 Corresponding electrical and magnetic basic quantities.

Electrical circuits			Magnetic circuits		
Potential	V	volt (V)	Magnetomotive force	$\mathscr{F}$	ampere turn (A)
Current	I	ampere (A)	Flux	Φ	weber (Wb)
Resistance	R	Ohm (Ω)	Reluctance	$\mathscr{R}$	(A/Wb)
Spec. resist.	ρ	(Ω·m)	permeability	μ	(Wb/A·m)

3.4.2. First order approximation

In the first order approximation, the total magnetic circuit can be described as a macro scale magnetic yoke ending in micron scale pole tips, with a small air gap between the tips. Ignoring flux leakage, the reluctance of the circuit is simply the sum of the reluctances of the yoke $_{(y)}$, pole tips $_{(p)}$ and the air gap $_{(a)}$ between the poles.

$$\mathscr{R} = \sum_j \mathscr{R}_j = \frac{l_y}{\mu_y A_y} + \frac{l_p}{\mu_p A_p} + \frac{l_a}{\mu_a A_a} \tag{3.8}$$

Because the permeability and average cross-section of the yoke and pole tips are several orders of magnitude higher than that of the air gap, the total reluctance of the magnetic circuit is determined only by the air gap. Together with the required magnetic flux, the reluctance is entered in equation (3.6):

$$\mathscr{F} = \Phi \mathscr{R} = BA \cdot \frac{l_a}{\mu_a A_a} \tag{3.9}$$

Giving the total ampere-turns to be produced by the magnetic coils:

$$N\,I = B\frac{l_a}{\mu_o} = 1.8\frac{20\times10^{6}}{4\pi\times10^{-7}} \approx 28 \text{ A} \tag{3.10}$$

Where the flux leakage out of the yoke is neglected.

3.4.3. Model including saturation and flux leakage

To calculate the flux leakage the complete yoke geometry was simulated in Femlab exactly to scale (Figure 3.22). Flux can now flow over from a given position on the yoke to another, without reaching the end of the tips. The model for the material of the pole tips includes saturation as described in section 2.6.2.
The flux density at the coil area was varied until the tips reached saturation. Then the flux in the coil area and the end of the pole tip can be compared, giving an estimation of the flux leakage of the system. In a 2D simulation as shown in Figure 3.22, where only the width of the different parts of the magnetic structure is considered, the flux reaching the tips is 8% of the flux generated by the coils,

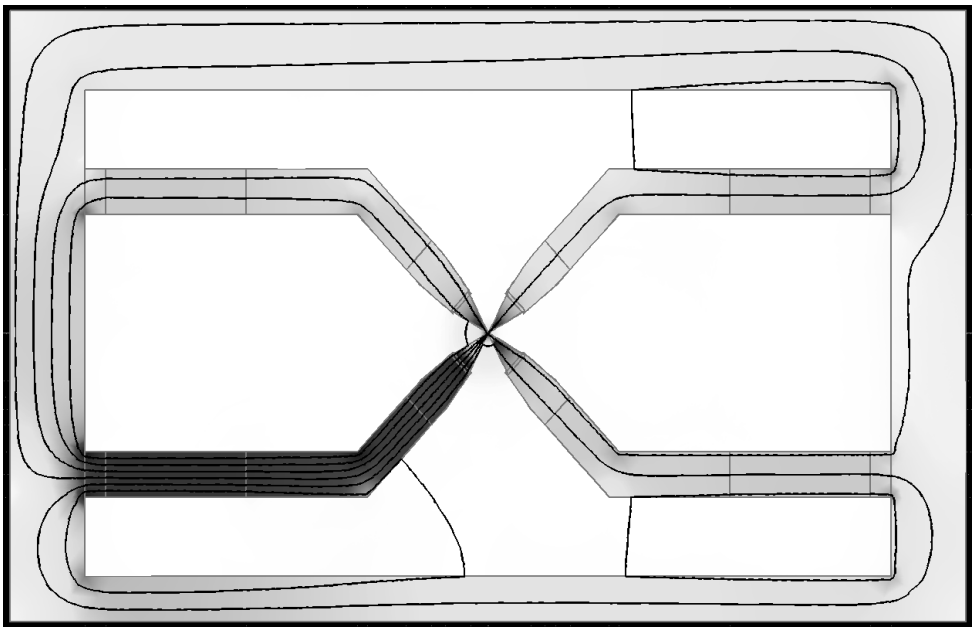

Figure 3.22 Complete magnetic yoke simulated in Femlab to scale, to predict the flux leakage in the magnetic circuit. The flux density in the poles is indicated by color intensity and field line density.

meaning that there is a 92% flux leakage. This means that the total ampere turn required for the yoke is 350 ampere turns distributed over 4 coils.

A 3D simulation of the complete system was not possible mainly due to the large scale difference between the features (from microns to centimetres). A pseudo 3D simulation has been performed, where the permeability of the air and yoke had been modified to model the third dimension (Figure 3.23). The yoke is thicker than the pole tips, which has been simulated by increasing the permeability of the yoke, as well as the air around it. The resulting flux density has to be calculated back again, to produce correct flux values. These simulations suggest that only 1% of the generated flux does actually reach the pole tips. This means that the four coils together need to produce 2800 ampere-turns. In a four-pole configuration with equal coil currents, this means 700 ampere-turns per coil, where a three-pole configuration needs 930 ampere-turns per coil.

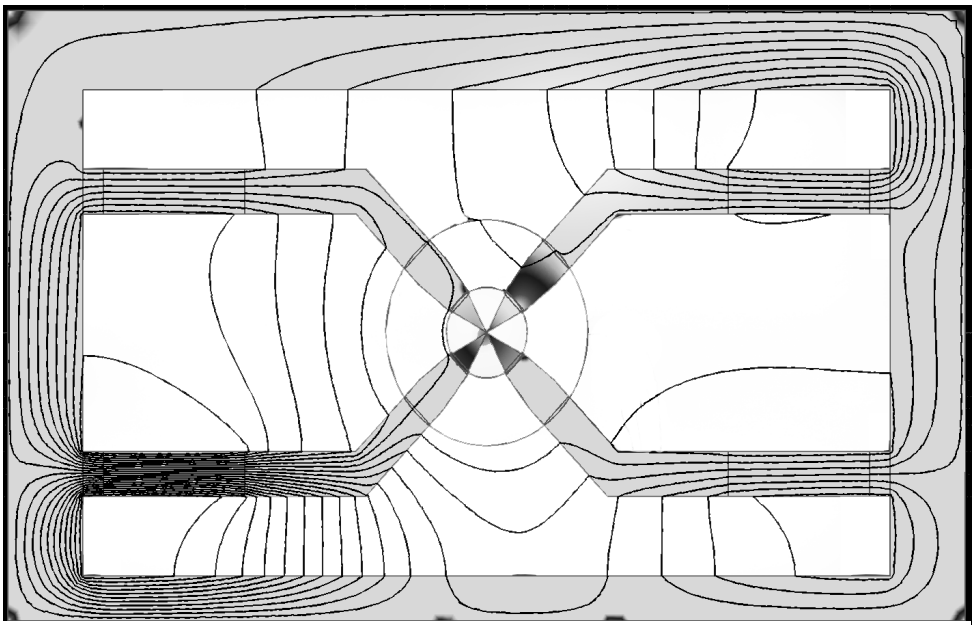

Figure 3.23 Pseudo 3D simulation where the third dimension was modelled by varying the permeability of yoke and surrounding air.

3.5. Electronics

3.5.1. Coils

In the previous section the number of ampere turns required for the electromagnet coils have been calculated. For the amount of flux, it does not matter if this is achieved by coils with few windings and high current, or many windings at low current. This choice is then dependent on other factors, such as self-induction, heat production, and coil size, safety and amplifier availability.

Comparing the maximum current rating for various diameters of coil wire, it turns out that the size of the coil remains constant for different wire diameters. The current density is therefore also a constant for the coil, meaning that heat production from Ohmic resistance is constant as well.

The self-induction however is strongly dependent on the number of coils. For a long solenoid, the self-induction is given by:

$$L = \mu \frac{N^2 A}{l} \tag{3.11}$$

Meaning that the maximum frequency at which the magnetic tweezers can operate is inversely dependent on the number of turns squared.

For safety it is preferable to work with low voltages, especially because the coils are close to the aqueous environment needed for the cells. Also the choice of amplifiers is largest for currents in the order of a few ampere's, at relatively low voltage. Combined with the need for low self-induction, this means that the coils are composed of few windings, but with thick wire capable of high current.

Two sets of coils were manufactured. One set of coils was designed with 80 windings rated at 3 A yielding a maximum of 240 ampere-turns per coil, for a total of 960 ampere-turns over the complete system. Connected to a suitable amplifier, this set can reach very high frequencies; due to the low self-induction (see section 3.5.2).
A second set of significant larger coils was produced, with 1000 windings rated at 0.75A, producing a maximum of 3000 ampere-turns. This set is used in low-frequency experiments, probing the maximum force the system is capable to exert.

3.5.2. Amplifier

The required amplifier for driving the coils at the given currents was custom build. Given the 3A maximum rating of the coil sets, four PA39 power amplifiers (Apex Microtechnology Corp.) are used for driving the coils. With a maximum voltage of ±35 V the bandwidth of the amplifier using the 80 windings coils was experimentally determined at 40 kHz with a phase shift of 120 degrees.

3.6. Conclusion

Several methods for manufacturing the desired pole tips for the magnetic tweezers have been investigated. A new micromachining method 'Delayed Lift-Off Electroplating' had to be devised for producing magnetic pole tips on the glass substrate, to satisfy all design criteria. In addition, a PLA coating was added as a final step, for the circumstance that cells are cultured directly on the pole substrates.

We have described the design of a yoke and amplifier that enables to saturate the cobalt pole tips. Expected flux leakage of 99% is taken into account in the design. A macroscopic yoke, electromagnets and amplifier were produced to drive magnetic tweezers, as well as an optical setup required for bead detection.

3.7. References

1 W. Rythooren, K. Attenborough, S. Beerten, P. Merken, J. Fransaer, E. Beyne, C. van Hoof, J. De Boeck, J.P. Celis. 2000. **Electrodeposition For The Synthesis Of Microsystems**, *Journal of Micromechanical Engineering*, 10: 101-107.

2 P.C. Andricacos, C. Uzoh, J.O. Dukovic, J. Horkans, H. Deligianni. 1998. **Damascene Copper Electroplating For Chip Interconnections**, *IBM J. Res. Dev.* 42: 567-74.

3 M. Datta, D. Landolt. 2000. **Fundamental Aspects And Applications Of Electrochemical Microfabrication**, *Electrochimica Acta*, 45: 2535-2558

4 F.A. Lowenheim, 1974. *Modern Electroplating*, 3rd ed, Wiley New York. ISBN 0-471-54968-1

5 S. Armyanov, 2000. **Crystallographic Structure And Magnetic Properties Of Electrodeposited Cobalt And Cobalt Alloys**, *Electrochimica Acta*, 45:3323-3335

6 N. M. Franklin, J.L. Stauber, S.C. Apte, R.P. Lim. 2001. **Effect of Initial Cell Density on the Bioavailability and Toxicity of Copper in Microalgal Bioassays**. *Environmental Toxicology and Chemistry*, 21:742–751.

7 P.A. Gunatillake, R. Adhikari. 2003. **Biodegradable Synthetic Polymers for Tissue Engineering**. *European Cells and Materials*. 5:1-16

8 U. Kubitscheck, O. Kückmann, T. Kues, and R. Peters. 2000**. Imaging and Tracking of Single GFP Molecules in Solution,** *Biophysical Journal***,** 78:2170-2179**.**

9 J.R. Reitz, F.J. Milford, R.W. Christy, 1980, **Foundations of electromagnetic theory**, *Addison-Wesley Publishing Comp. Inc.* 3rd ed. p.211

4. Experimental results

4.1. Introduction

In this chapter the magnetic tweezers are characterized. First the magnetic properties of the cobalt layers that make up the tweezers are investigated. Ideally the layers should have high magnetisation allowing high force, and low remanence, allowing quick changes in force amplitude and direction.
Subsequently, possible calibration techniques for characterizing the magnetic tweezers are discussed, followed by measurements showing the direction and amplitude control of the magnetic force that the tweezers can exert.
Using these calibrations, predictions are made about the achievable force on particles of different size and composition. Furthermore it is indicated which improvements can be made to further increase the maximum achievable magnetic force.

4.2. Characterization of magnetic materials

4.2.1. Vibrating Sample Magnetometer

The magnetic materials used were characterised using a Vibrating Sample Magnetometer (see Figure 4.1). In a VSM a sample is placed in a magnetic field inducing a magnetic moment in the sample. Vibrating the sample causes a flux change through the pick-up coils, producing an induction voltage proportional to the magnetic moment of the sample. Knowing the volume of the sample, material properties like the magnetisation saturation can be measured. The volume of the samples was determined both by measuring the height of the layers, as well as measuring the mass.

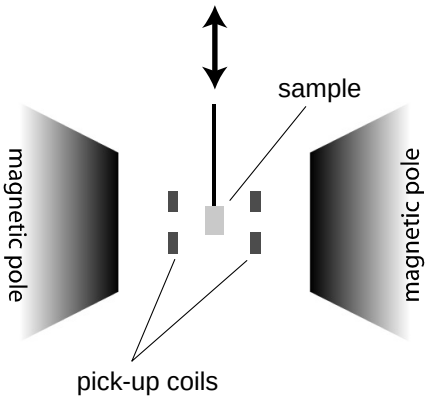

Figure 4.1 schematic of a Vibrating Sample Magnetometer. A sample is placed in a magnetic field. It is vibrated close to a set of pick-up coils, to measure the magnetic moment of the sample.

4.2.2. Characterisation of the cobalt layers

Figure 4.2 and Figure 4.3 show a typical ferromagnetic hysteresis curve measured for the electroplated cobalt layers. All the cobalt poles measured showed a saturation magnetisation of 1100 kA/m (~ 1.38 T). This is at 77% of the

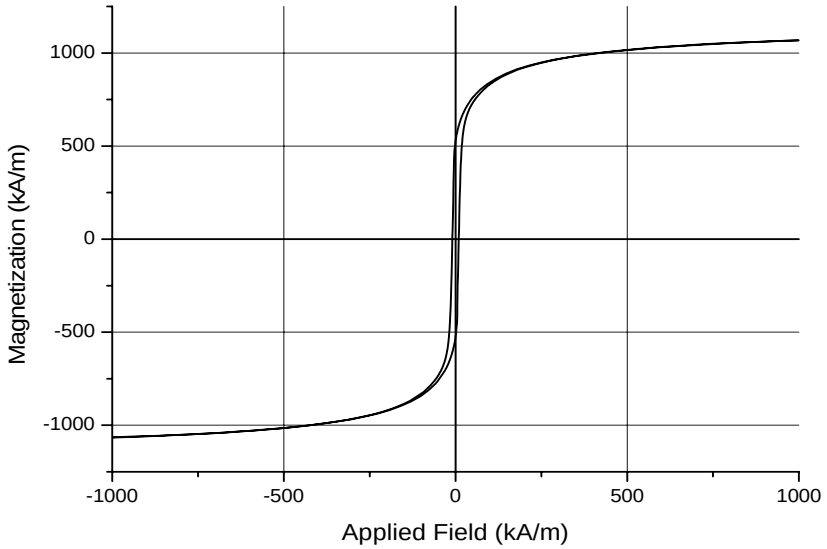

Figure 4.2 Hysteris curve M vs. H for the electroplated cobalt layer measured with a Vibrating Sample Magnetometer. The magnetisation is measured parallel to the surface of the sample, and reaches a saturation magnetisation of 1100 kA/m.

maximum bulk cobalt saturation [1].The saturation magnetisation is directly proportional to the maximum force the magnetic tweezers can exert.

Different magnetic properties of electrodeposited materials, as compared to bulk properties are common in electroplating. Improvements are generally possible, since material characteristics such as grain size or preferred crystal orientation can be steered through the electrodeposition process parameters [2].

The shape of the hysteresis curve can be influenced by changing the plating conditions, which influences the crystal structure of the deposited cobalt and as a result also the magnetic properties of the cobalt layer. Electroplated cobalt layers are composed of two crystallographic modifications, αCo (hexagonal close packed) and βCo (face-centred cubic) [3]. The two phases are very different in their ferromagnetic properties. βCo has more axis of easy magnetisation, lowering the coercive force. The plating parameters affect both the phase composition of

the electroplated layer, as well as the grain size and texture perfection, all of which have their influence on the magnetic properties.

We were able to make the hysteresis loop narrower and higher, i.e. decrease the coercive force, and increase the remanence, by adding boric acid and increasing the electroplating bath temperature (Table 4.1). Higher temperatures were not tested due to the high evaporation rate of the aqueous electroplating bath close to its boiling temperature. The saturation magnetisation remained the same at 1100 kA/m. The change in crystal structure is also illustrated by SEM images of the corresponding poles (Figure 4.4).

Table 4.1 Magnetic properties at different plating conditions

	Electroplating bath		Coercive force	Remanence
	Temperature (°C)	Composition	(kA/m)	(% of saturation)
A	58°	$CoCl_2$/SDS	16,9	26%
B	56°	$CoCl_2$/SDS/H_3BO_3	9,37	48%
C	68°	$CoCl_2$/SDS/H_3BO_3	4,27	61%

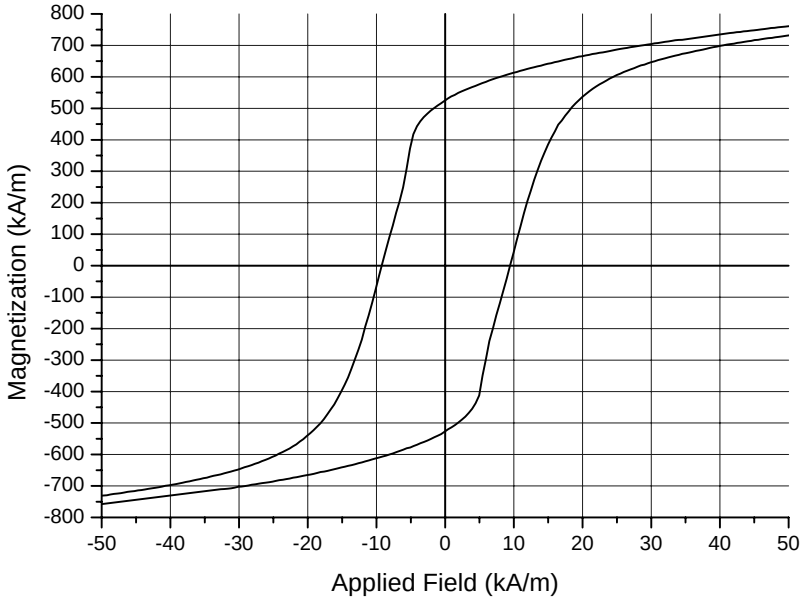

Figure 4.3 Detail of the hysteresis curve of the electroplated cobalt layer. The cobalt poles show a coercive force of 9 kA/m and a remanence of 525 kA/m

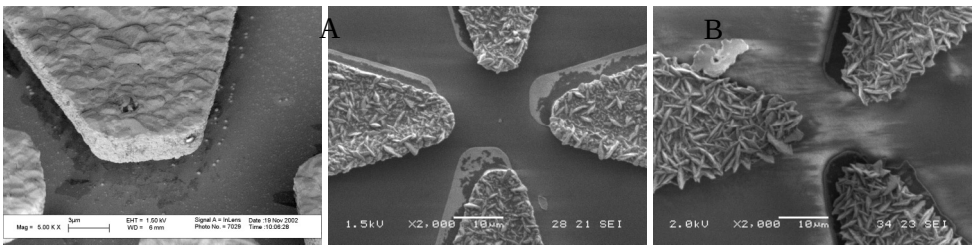

Figure 4.4 Crystal structures corresponding to ever narrower hysteresis curves of the electroplated cobalt poles.

A narrower and higher hysteresis loop means that the poles can be quicker brought to saturation, and that it is are easier to reverse the magnetisation. Therefore, electroplating condition 'C' was used for producing the magnetic poles. However, it does also imply that the poles will stay highly magnetized when the coils are switched off. Demagnetizing the poles will require a degaussing procedure looping the hysteresis multiple times while gradually lowering the applied field.

4.3. Force calibration

4.3.1. Calibration techniques:

Finding a good method to calibrate the setup proved to be a very difficult task. The small size excluded options like a Hall probe to directly measure the magnetic field. Therefore the field had to be measured indirectly, by determining the magnetic force exerted on a particle with known magnetic moment. The different techniques that can be used to measure force include:

- Particle tracking in a viscous medium
- Atomic/magnetic force microscopy
- Optical tweezers
- Bead embedded in elastic sheet
- Micro pipette

Particle tracking in a viscous medium

Typically magnetic tweezers are calibrated by pulling a magnetic bead with known diameter through a viscous medium with known viscosity η, and recording the speed of the particle. This method is difficult to use on our multi-pole magnetic tweezers due to the combination of high force and a very small work area between the poles. In a macroscopic or single pole magnetic tweezers, the magnetic field extends to a large area. In our case, the relevant field gradient only

exists within the area between the poles (20 μm across). This means that the beads would have to be injected and followed within this area. However, even using glycerol with a relatively high viscosity of 1.5 Pa·s, typical magnetic calibration beads (e.g. Dynal MyOne 1 μm diameter) will move at 30 μm/s velocity (see 2.3.1). Clearly, this is not an applicable method for calibration of our magnetic tweezers.

Atomic/Magnetic Force Microscope

The Atomic Force Microscope is a very sensitive system for measuring force, and can accommodate a large spectrum of forces (pN to nN) by using cantilevers of different stiffness. The AFM however is primarily designed to measure deflection (and thus force) perpendicular to the surface. The magnetic tweezers however produce force parallel to the surface. The AFM can be made sensitive to these forces by putting the cantilever at an angle to the surface. In addition also torsion of the cantilever, caused by the bead glued to the underside of the cantilever, can be measured. Combining the torsion and deflection can then reveal amplitude and direction of the magnetic force.

Optical Tweezers

Because most commercial magnetic beads are polystyrene spheres with magnetic material dispersed through the bead, they can be trapped by optical tweezers (force range 0.1~50 pN). The forces produced by our magnetic tweezers however far exceed those that optical tweezers can produce. Even the micron sized bead with the lowest amount of magnetic material (Mercks 1.12 μm 12% ferrite) will experience a force of 250 pN in a gradient of 30 kT/m.
A solution would be to use a non-magnetic polystyrene bead attached to a far smaller magnetic bead, thereby adjusting the magnetic force to the optical force, but it is difficult to assure only one magnetic bead is attached to the polystyrene bead.

Beads embedded in elastic sheet

Beads can be encased in an elastic polyacrylamide sheet as described in [4]. Knowing the exact elastic properties of the sheet, measurement of the displacement of a magnetic bead in such a sheet yields the force on that bead. Assuming a sheet with the right size, elasticity and distribution of beads can be constructed, so that beads can be positioned within the sample area (both lateral and axial), it could be used for calibrating the magnetic tweezers. However, the quoted reference cautions that the calculation is extremely difficult, and they therefore restricted it only to qualitative measurements.

Micro pipette

Micro pipettes can be pulled in a wide spectrum of shape and size, depending on the application they are meant for. As a result, also a broad range of pipette stiffnesses can be made ranging from 3×10^4 nN/μm to 0.1 nN/μm. Such micropipettes have been used as a force sensor with a resolution of 10 pN [5]. By gluing a magnetic bead to the end of the pipette, and recording the displacement of this bead due to a magnetic field, the magnetic force on the bead can be determined. This setup is perfectly suited for measuring lateral forces, while at the same time it is insensitive to axial forces.

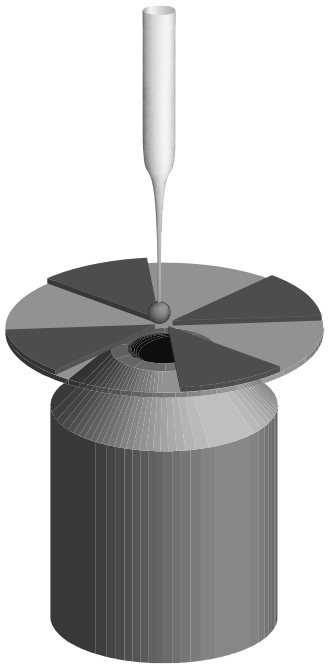

Figure 4.5 Calibrating the setup using a bead attached to a micro pipette, and recording the displacement.

Discussion

Comparing the characteristics of the different techniques, only the AFM and micro-pipette based techniques are viable to calibrate the magnetic tweezers. The AFM has a major disadvantage that it is most sensitive in the wrong direction, complicating measurements. The micropipette based method proved to be very flexible and effective. It is can be adapted to the required force range, is sensitive in the proper direction, and the (lateral) stiffness is isotropic. Therefore the force calibration was performed using the micropipette based technique.

4.3.2. Force calibration using a micropipette

Method

A micropipette is pulled with the desired shape and stiffness. A magnetic bead is attached to the end of the pipette, and this construct is suspended perpendicular to the poles as shown in Figure 4.5. The bead displacement $\Delta\vec{r}$ due to the applied magnetic force $\vec{F}_m$ is recorded using video microscopy. The video is analyzed off-line using home written Labview software that tracks the position of the bead with subpixel accuracy.

Having calibrated both the magnetic moment $\vec{m}_b$ of the bead and the spring constant of the pipette k_p, we can directly calculate the force on the bead and the magnetic field gradient:

$$\vec{F}_m = k_p \Delta\vec{r}$$
$$\nabla\left|\vec{B}\right| = \frac{\vec{F}_m}{\left|\vec{m}_b\right|} \tag{4.1}$$

Pipette pulling

Considering the accuracy of video microscopy (~10 nm), and the expected force (~ nN) the micropipettes need a stiffness in the order of 1 nN/μm. In this way the force range is 1nN to 10 pN while having a spatial resolution of 1 μm. Borosilicate pipettes of 1.2 mm outer diameter and 0.94 mm inner diameter (Harvard apparatus GC120TF-15) were pulled using a Sutter P-87 micropipette puller. The stiffness of these pipettes was calibrated against an AFM cantilever with know spring constant.
The two types of cantilever used for the calibration (TM Microscopes Veeco Microlevers tip B and C) have a spring constant of 10 resp. 20 nN/μm. Before use, these cantilevers are recalibrated in an AFM to improve on the accuracy of the spring constant supplied by the manufacturer.

Pipettes could be pulled in one step, producing a long tapering (10 mm) ending in a diameter of less than a micron. These pipettes have a spring constant between 0.3 and 2 nN/μm. However, they proved to be very sensitive to disturbances, especially air flow, due to the long taper. Pipettes of this type, with a spring constant of less than 1nN/μm were too unstable to be used in calibration experiments.

This is solved by pulling the pipettes in multiple steps (see Figure 4.6). In the first two pulls, the pipette is reduced to a small diameter (100 μm) before the final pull that shapes the end of the pipette. This method gives more freedom in setting the parameters that produce the end of the tip, which is the only part significant for the stiffness. A three step procedure allowed producing a very short end tip with the right elasticity modulus, enhancing stability to a point well below the accuracy of the detection method.

Table 4.2 lists the settings used for pulling the three-stage pipettes on the Sutter P-87 pipette puller. These numbers should be interpreted only as a guide for setting the pipette puller, as they may vary due to different heating filament shape and placement, and environmental conditions.

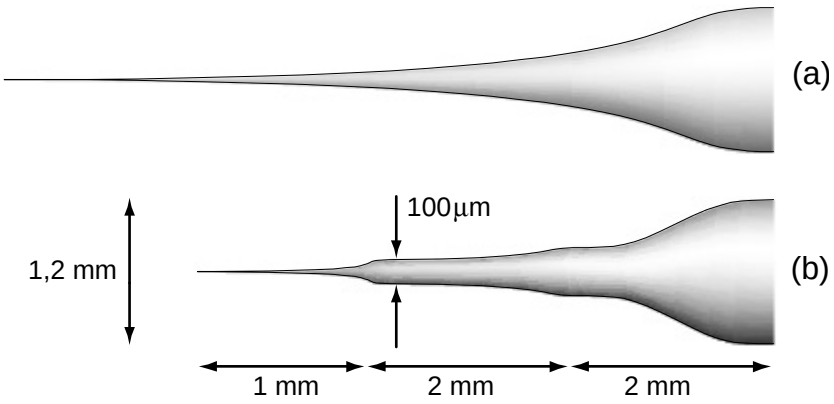

Figure 4.6 Difference in the shape of the micro pipette pulled in one or three steps

The heat setting is set to standard value (5 units above ramp). Time is set low to start with, and is initially only increased to remove flimsy ends. Pull and velocity have to be varied to achieve the desired diameter and stiffness. The pull setting needs to be kept low to produce short tapers. The time setting can finally be adjusted for further shortening of the end of the pipette.

Table 4.2 Settings for pulling a three-stage micropipette of 1 nN/µm spring constant.

Step	Heat	Pull	Velocity	Time	Pressure
1	390	0	10	200	400
2	390	0	5	200	400
3	390	60	120	120	400

Calibration of the micropipette system

The pipette used for the calibration had a tip diameter of approximately 800 nm. The final taper is only 1 mm long. The micropipette has been calibrated against both AFM cantilevers, yielding a spring constant of 0.8 ± 0.1 nN/µm. The relatively large error is due to the low accuracy of spring constants of the AFM cantilevers, even after recalibration of these cantilevers on the AFM instrumentation. Still, this error is small compared to the 30% accuracy that was achieved using different methods [5]. Calibrating the pipette itself by pushing against the AFM cantilever can be done very quickly. This allowed averaging of multiple experiments, so that a *relative* accuracy of 5% between the pipettes was easily reached.

The pipette proved to be extremely stable, being very insensitive to air flow. The accuracy of the force measurement therefore is primarily dependent on the accuracy of the bead tracking algorithm. During the measurements, the video microscopy method achieved an accuracy of 0.1 pixels, corresponding to an accuracy of 14 nm. Therefore, with the current stiffness the micropipette system can achieve a force resolution of 11 pN.

A Dynal M-280 magnetic bead was glued to the micropipette using two-component epoxy glue (Bison Combi). The bead has a reported volume magnetisation of 11.5 kA/m with an accuracy of 5%.

4.3.3. Force direction

The micropipette with magnetic bead was placed in between the poles of a three-pole configuration by means of a micromanipulator. A square current with 33% duty cycle was supplied to the coils, so that the bead was pulled towards each one of the poles in succession. As a result the bead attached to the micropipette describes a triangular movement, as show in Figure 4.7. The time trace shown is recorded at relatively low setting of 250 ampere turns per coil. It is obvious that the force is acting in three distinct directions, towards the three poles of the

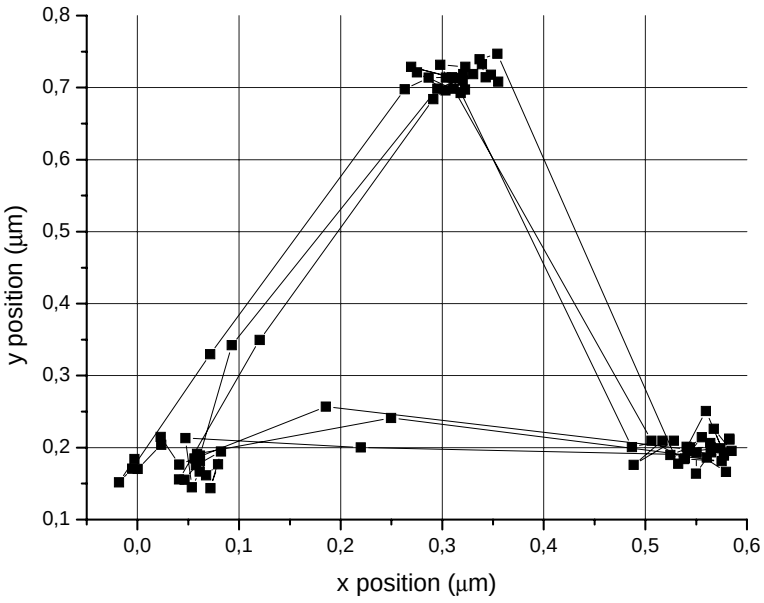

Figure 4.7 Time trace of a magnetic bead attached to a micropipette in a three-pole configuration where the bead is pulled towards each of the poles in succession. (250 ampere turns per coil)

magnetic tweezers. The movement of the bead from one corner to the next proved to be too fast to be observed with the 25 Hz frame rate of the video camera used.

This experiment clearly demonstrates the possibility of moving a bead in different directions. Driving the coils with e.g. sinusoidal currents it was possible to have the bead move in circles. More complex steering of the bead is also possible by providing the proper time varying currents. The centre of the triangle is the resting position of the micro pipette when there is no force acting on the bead. The distance from this centre towards the corners of the triangle is proportional to the magnetic force acting on the bead, and the stiffness of the micro pipette. This has been used to determine the magnetic force as described in the next section.

4.3.4. Force amplitude

The force calibration has been performed on the same three-pole structure that was later used for the biological experiment. These poles have a 6 μm thickness, and were electroplated using condition C as described in section 4.2.2. The coil set with 1080 windings per coil was used.
The coils were supplied with an alternating block current at 1 Hz with 33% duty cycle, producing a triangle time trace similar to the example in section 4.3.3. Time traces were collected ranging from the lowest measurable force, up to the highest current density the coil and amplifier combination can deliver.

For each setting of the current density, at least 30 cycles of the triangle trajectory were recorded on video. Image analysis software calculates the position of the bead for each frame, producing eight data points per triangle corner. The force is calculated for a selection of these triangles, and from this the average force and the standard deviation is obtained. The result is show in Figure 4.8.
The magnetic tweezers were able to exert a maximum force of 1000 pN on the M-280 magnetic bead, corresponding to a gradient in the flux density of 7.5 kT/m. It proved to be possible to control the force amplitude by simply lowering the current through the coils. At low force, the accuracy is limited by the detection method, yielding an accuracy of 11 pN. Above 1000 ampere turns per coil, the system starts to experience a significant amount of drift during the time span of the measurement. At the same time, the deflection become so large, that it is no longer assured that the magnetic flux gradient is homogeneous over the area that is ‘probed’ by the bead. These effects results in a larger error in the measurements, as indicated in the graph.

In order to compare the results with those expected from theory, the pole thickness and lower saturation magnetisation need to be accounted for. Theory predicts a gradient of 30 kT/m for the ideal three-pole configuration, producing a

force of 3963 pN on an M-280 magnetic bead (Table 2.7). The saturation magnetisation is directly related to the magnetic force, thus introducing a factor 0.77 into the theoretical predictions. The 6 µm pole thickness is responsible for an extra factor 0.32 to the simulations (see Figure 2.19). Accounting for both these factors, the maximum force predicted for an M-280 bead in the used pole set is 976 pN. This is in remarkable agreement with the calibration experiment which produced a maximum force of 1040 ± 270 pN

The solid line in Figure 4.8 shows the predicted magnetic force, based on the actual measured hysteresis curves of the cobalt poles and the M-280 magnetic bead, and including the diminished field product by poles of 6 µm height. To be able to use the *M* vs. *H* hysteresis loop of the cobalt poles as measured in section 4.2.2 as input for a Femlab simulation, the magnetic permeability $\mu_r = {}^{M}/_{H}$ has to be expressed in terms of the magnetic flux density *B*. An expression in *H* would lead

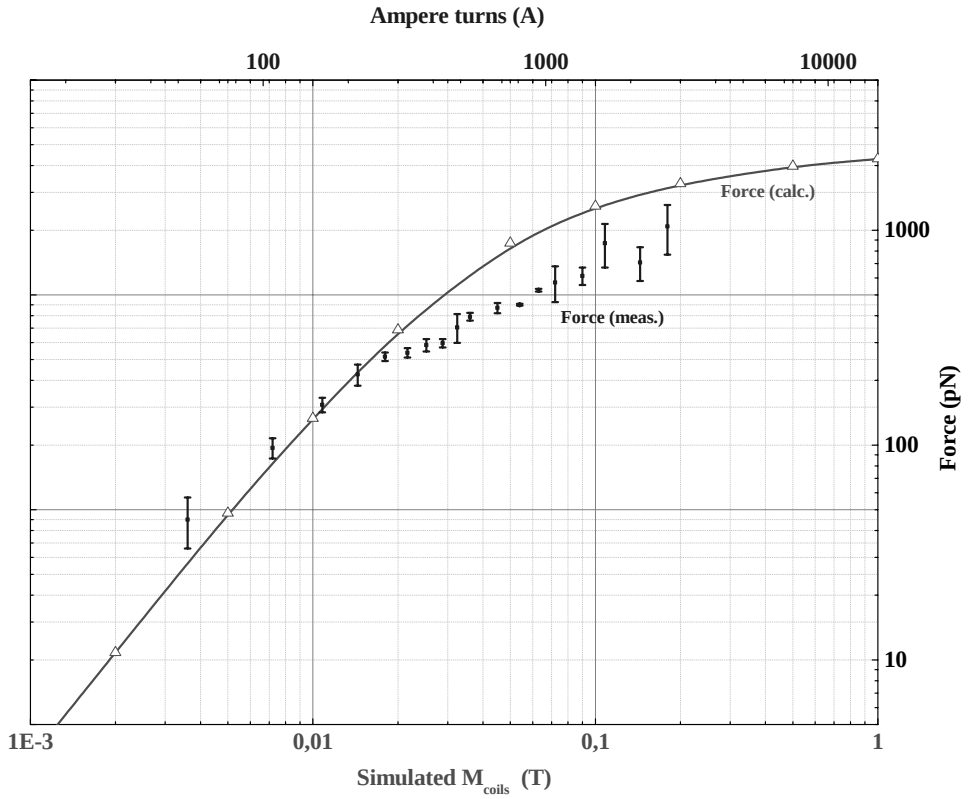

Figure 4.8 Force vs. current in the three-pole magnetic tweezers configuration using a Dynal M-280 magnetic bead (plotted measurement point, top axis). The line indicates a prediction of the force (bottom axis).

to a circular relationship of μ and H in the simulation, making it impossible to solve. The relative permeability of the cobalt can be written in terms of B as:

$$\mu_r = \frac{1}{1 - \frac{\mu_0 M(B)}{B}} \tag{4.2}$$

The magnetisation $M(B)$ is derived from the measured M vs. H data (Figure 4.2). It was found that the data $M(B)$ could be described by the following equation:

$$M(B) = \left(1 - 2\left(\frac{0.5}{1+10^{B+0.6}} + \frac{0.5}{1+10^{B-0.6}}\right)\right) \cdot 1{,}067 \times 10^6 \tag{4.3}$$

Combining equation (4.2) and (4.3) gives an analytical expression of μ_r as a function of B. This is the input required for the Femlab model. Figure 4.9 shows the measured and fitted permeability of the cobalt poles. The fit looks ill-suited for flux densities between −1 and +1 tesla. However, this region of the permeability has neglectable influence on the simulation. It is sufficient that the μ_r >>1. The important region is the part μ<10 which is responsible for the correct magnetic saturation behaviour.

The simulation predicting the force does not take into account the complete setup of the magnetic tweezers. The electromagnetic and macroscopic yoke are not simulated due to limitation of computing power, but are taken into account by applying a magnetic flux density (see section 2.6.2). The x-axis of the simulation thus labels flux density, while the calibration measurement uses the current through the electromagnets. Although this relation is expected to be linear, the precise correlation between flux density and current is difficult to be estimated precisely, since it strongly depends on the flux leakage (see section 3.4.3). Therefore, the predicted and measured curves were shifted horizontally to overlay them,

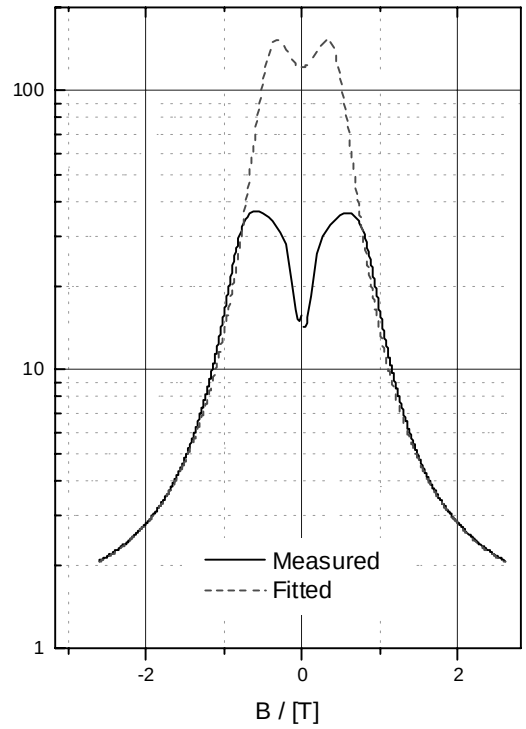

Figure 4.9 Measured and fitted permeability of the cobalt pole structures.

thereby setting the conversion between flux density and current.

Approximation of the force behaviour

To be able to control the force acting on a bead by changing the current through the coils, it is necessary to find an expression that describes the tweezers' behaviour as it has been measured. The theoretical line plotted in Figure 4.8 cannot be used, as this is not produced by a single equation, but constructed from a large number of complex 2D simulations. Furthermore, it does not relate to current, but to applied field in the simulation. It thus ignores flux generation and flux leakage. Therefore, it is necessary to generate a new equation that approximates the measured characteristics of the tweezers.

As noted before, two different saturation effects are observed when increasing the current: First from the magnetic bead and then from the cobalt poles. This behaviour has been approximated by the double exponentially decaying function:

$$y = y_0 + A_1 e^{-x/t_1} + A_2 e^{-x/t_2} \tag{4.4}$$

This function was fitted to the data points using a Levenberg-Marquardt procedure that included the error bars for weighting. Due to the large errors in the high flux region, the saturation parameter y_0 had to be fixed to achieve a meaningful solution. The parameters A_1 and t_1 describe the behaviour of the poles, while A_2 and t_2 can be attributed to the saturation of the magnetic bead. The result is plotted together with the collected data points in Figure 4.10. The fitted curve describes the tweezers behaviour remarkably well. Therefore, it can be used to relate magnetic force to applied current. The curve is obviously only a description of empirical data, and should only be used in that way.

Table 4.3 Parameters for the double exponentially decaying function used to fit the experiemtal data in Figure 4.10

y_0	A_1	t_1	A_2	t_2
1000	-928 ± 90	1346 ± 207	77 ± 86	150 ± 22

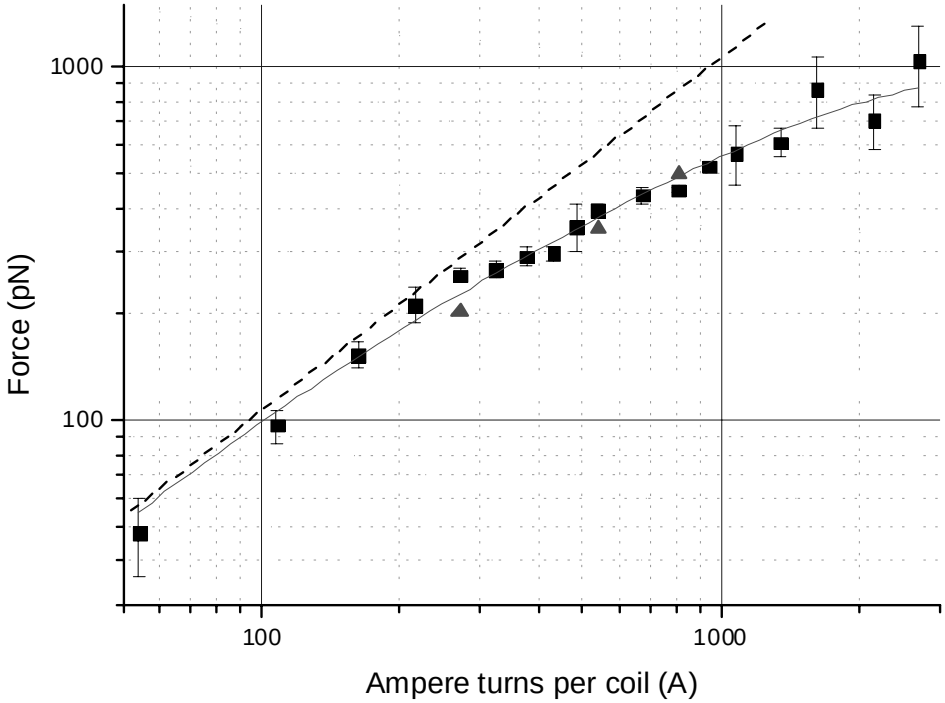

Figure 4.10 Force calibration of the three-pole configuration using an M-280 magnetic bead attached to a 0.8 nN/μm pipette place at the centre between the pole tips. The triangles indicate data points achieved with a 0.3 nN/μm micro pipette. The behaviour can be described very well by a double exponentially decaying function, which is indicated by the line through the data.

4.4. Discussion and conclusions

In this chapter, the magnetic tweezers were characterised. The material properties of the magnetic tweezers were determined, and the magnetic force on small magnetic beads was measured

The magnetic tweezers have demonstrated to be able to exert very high forces, up to 1000 pN on M-280 beads, corresponding to a magnetic gradient of 7.5 kT/m. This makes them more than 35 times more powerful than current multi-directional magnetic manipulators, that only achieved magnetic gradients of 200 T/m [6] resp. 20 T/m [7].
The gradient of the magnetic tweezers even equals that of uni-directional magnetic ‘tweezers’ that achieve gradients of 6.5 kT/m [8] resp. 9.1 kT/m [9]. However, as these ‘tweezers’ can only produce force in one direction, they can only produce a disturbance, but not truly manipulate magnetic beads. This makes

the developed magnetic tweezers the only magnetic manipulator that can perform real intracellular manipulation!

Figure 4.11 shows a prediction of the forces that are achievable with the current magnetic tweezers, in relation to the bead material and diameter. For comparison the forces exerted by optical tweezers are included.
Using the proper materials, the biological relevant forces in the pN range can be achieved with beads that are small enough to be used in intracellular applications.

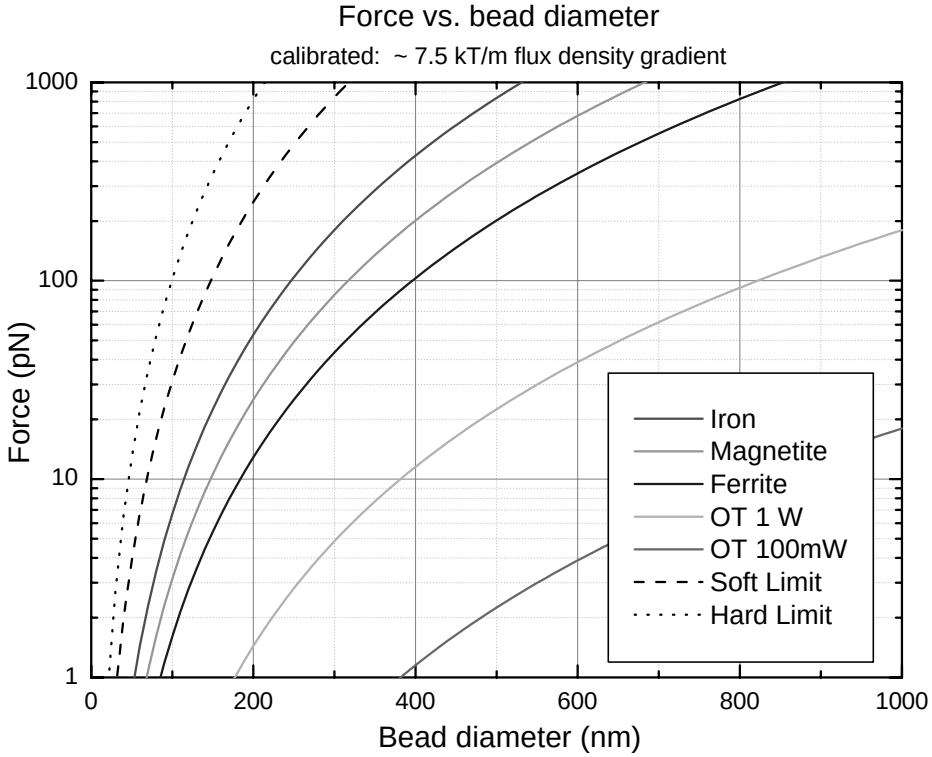

Figure 4.11 Prediction of forces that are achievable with the *current* magnetic tweezers. The two dotted lines indicated the possible improvement range for a tweezers that has 20 micrometre separation between the poles.

Even higher field gradients and forces are possible, as the current magnetic tweezers have not been optimized yet. The dotted lines in Figure 4.11 indicate the possibilities for improvement. Increasing the pole height, and saturation magnetisation of the poles, will improve the achieved flux gradient. The 'soft limit' indicates the force on an iron bead that can realistically be achieved with the improvements described below.

The cobalt layers forming the poles exhibited a saturation of 1.38 T. The electroplating plating process was shown to have great influence on the magnetic properties. We have prioritized on getting functional poles, and not determined the influences of all the parameters individually. Optimizing the plating process with respect to the magnetic properties is advisable. This should also include looking into the possibility of plating cobalt iron based alloys, as these materials exhibit the largest magnetic saturation (2.3 T).
Considering these differences in saturation, potentially the maximum achievable magnetic force can be increased by 65%, compared to the current magnetic tweezers, by optimizing the pole material.

Currently the poles have a thickness of 6 μm, incurring a 68% penalty to the achievable magnetic field. Increasing the thickness of the poles reduces this penalty drastically. For example, poles of 12μm thickness will double the current magnetic gradient, and thus magnetic force.

It is also possible to predict the maximum flux gradient that can be achieved with this type of magnetic tweezers. Knowing that 2.3 T is the highest saturation achievable in *any* magnetic material, the best gradient any design can ever achieve, is a linear decay of this 2.3T over the 20 μm spacing between the poles, yielding a 115 kT/m gradient in the flux density. This is the 'hard limit' shown in the graph.

Magnetic tweezers cannot produce higher gradients in the flux density, unless the poles are placed close together, or the flux is generated directly at the pole tips, removing the restriction of flux guiding poles.

4.5. References

1 **Cobalt**, *Metals Handbook* 9th ed. 2:725:726, compiled by D.J. Maykuth, Metals and Ceramics Information Center, Battelle Memorial Institute.

2 W. Rythooren, K. Attenborough, S. Beerten, P. Merken, J. Fransaer, E. Beyne, C. van Hoof, J. De Boeck, J.P. Celis. 2000. **Electrodeposition For The Synthesis Of Microsystems**, *Journal of Micromechanical Engineering*, 10: 101-107.

3 S. Armyanov, 2000, **Crystallographic structure and magnetic properties of electrodeposited cobalt and cobalt alloys**., *Electrochimica Acta* 45:3323-3335

4 R. J. Pelham Jr., Y. Wang, 1999, **High Resolution Detection of Mechanical Forces Exerted by Locomoting Fibroblasts on the Substrate**, *Molecular Biology of the Cell*, 10:935-945.

5 M. Poirier, S. Eroglu, D. Chatenay, J.F. Marko, 2000, **Reversible and irreversible unfolding of mitotic newt chromosomes by applied force**, *Molecular Biology of the Cell*, 11:269-276.

6 H. Huang, C.Y. Dong, H-S. Kwon, J.D. Sutin, R.D. Kamm, P.T.C. So, 2002, **Three dimensional cellular deformation analysis with a two-photon magnetic manipulator workstation**, *Biophysical Journal*, 82:2211-2223

7 C. Gosse, V. Croquette, 2002, **Magnetic Tweezers: Micromanipulation and Force Measurements at the molecular level**, *Biophysical Journal*, 82:3314-3329

8 B.G. Hosu, K. Jakab, P. Bánki, F.I. Tóth, G. Forgacs, 2003, **Magnetic Tweezers for intracellular applications**, *Review of scientific instruments*, 74:4158-4163

9 A.R. Bausch, F. Ziemann, A.A. Boulbitch, K. Jacobsen, E. Sackmann. 1998. **Local measurements of viscoelastic parameters of adherent cell surfaces by magnetic bead microrheometry**. *Biophys. J.* 75:2038-2049.

5. Application to Living Cells

5.1. Introduction

To demonstrate the viability and possibilities of the developed magnetic tweezers, experiments with bead manipulation in *living* cells were performed. In this chapter we will describe how to get a single magnetic bead inside a living cell, and how to get a specific cell in between the magnetic poles. It will be shown that magnetic beads can be manipulated (both over short and long distances) in the cell using the magnetic tweezers. The exerted force and resulting movement of the magnetic beads could be used to measure the viscoelastic properties of the cell in more detail than before.

The inside of the cell is an extremely complex environment. It is heterogeneous, consisting of cytoskeleton, organelles, etc embedded in the cytoplasm. As a first approximation, the behaviour of a moving magnetic bead through such a medium is typically described using a viscoelastic model where the main parameters are the apparent cell viscosity and elasticity. A lot of research has already been done trying to measure the viscoelastic properties of the cell. Table 5.1 lists the reported values of measured apparent cell viscosity η_0 and elasticity μ. The reported results vary considerably, spanning 4 orders of magnitude for both viscosity and elasticity. These properties have been measured using very different cells, and different techniques. Part of the spread in values may thus be explained by the different types of cells being used. For example, the macrophage experiments all give values between 10 and 10^3 for elasticity and viscosity, while results on fibroblasts lie between 10^3 and 10^5. However, also when the same cell types are being used, quite large variations exist, which must either be contributed to the measuring technique, or the model used.

From the table it can be seen that most measurements have been performed on whole cells, where the cell is deformed, for example by sucking it into a pipette, or tapping on it with an AFM. Also large probes have been positioned on the cell membrane, and moved or rotated to cause a deformation. Only a few experiments have been performed inside cells using magnetic beads that are twisted, or pulled through the cytoplasm, giving a more direct approach to determining the viscoelastic properties of the cytoplasm.

Table 5.1 Reported values for cell viscosity and elasticity compiled from Bausch et al. [1] and Yamada et al. [2].

Method	Technique	Cell type	Elasticity (Pa)	Viscosity (Pa s)	Cit.
Extracellular or whole cell					
Magnetic twist	Shear Force	Endothelial	2.0	5 – 10	[3]
Micropipette	Forced Flow	Leukocyte	0.75, 23.8	33	[4]
Micropipette	Forced Flow	Neutrophil		10^2	[5]
Cell poker	Force	Neutrophil	1.18×10^2		[6]
AFM	Force	Platelet	$1\text{-}50 \times 10^2$		[7]
Microplates	Shear Force	Fibroblast	$\sim 10^3$	$10^2\text{-}10^4$	[8]
Spont. Retraction		Fibroblast	1.7×10^3	4×10^5	[9]
Magnetic tweezers	Shear Force	Fibroblast	3×10^4	2×10^3	[10]
		Squid axoplasm		10^4 - 10^5	[11]
		Sea urchin egg		10	[12,13]
Intracellular					
Magnetic twist	Torque	Macrophage	15	2×10^3	[14]
Magnetic twist	Torque	Macrophage		250	[15]
Magnetic twist	Torque	Macrophage		2.8×10^3	[16]
Magnetic tweezers	Force	Macrophage	20-735	2.1×10^2	[1]
Magnetic tweezers	Force	Macrophage	10-100	10-350	[17]

In principle, all these methods can yield correct results, if the applied model is valid. However, it is debatable if such a complex environment can be sufficiently

described with such a simple viscoelastic model. First, the cell is very heterogeneous, and it is probable that the viscosity and elasticity, that are a result of the combination of cytoskeleton and organelles, also vary with position in/on the cell.

There are also indications that the viscoelastic model itself is lacking, for some experiments indicate that the measured viscosity is not a constant property, but is dependent on force [17] and shear rate [15,16]. The origin of this behaviour of the apparent cell viscosity may lie in the filaments forming the cytoskeleton. If these filaments are very strongly entangled like spaghetti, then moving a bead through it would be very dependent on the speed of the bead, stiffening when moving at high speeds, because the filaments can't disentangle quickly enough.
Besides being entangled, the filaments may also be interconnected by molecular cross links. Moving a bead through the cytoskeleton possibly involves breaking these molecular bonds, which is easier when using higher force.

5.2. Viscoelastic behaviour of the cytoplasm

The behaviour of a moving magnetic bead through the cytoplasm is typically described using a viscoelastic model. The mechanic behaviour of the viscoelastic medium is then characterized by a spring with spring constant *k* and two dashpots with viscous drag γ_0 and γ_1 (Figure 5.1). [17]

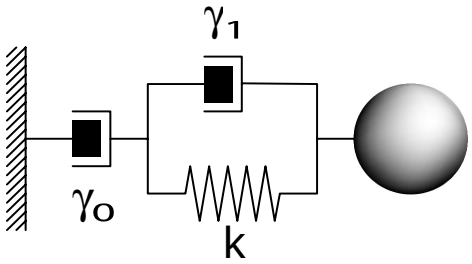

Figure 5.1 Model describing viscoelastic behaviour

Virtually all models in literature use these three parameters to describe the viscoelastic behaviour of the cytoplasm. The model above shows the one-dimensional situation. It can be extended into three dimensions by applying this 1D model to each axis.

Solving the equation of motion for this model gives the following expression for the movement of the bead following a step in force *F* at time t = 0:

$$\frac{x(t)}{F} = \frac{1}{k}\left(1 - e^{\left(-\frac{t}{\tau}\right)}\right) + \frac{t}{\gamma_0} \quad with \quad \tau = \qquad \kappa \tag{5.1}$$

With *x(t)* the displacement of the bead in the direction of the force, *F* the magnetic force on the bead and τ the time constant of the system.

The parameters k and γ are dependent on the size of the bead. Using a geometry factor g [1] these can be converted to the size independent viscosity η and elasticity μ:

$$\eta = \frac{\gamma}{g} \qquad \mu = \frac{k}{g} \qquad with: \quad g = 3\pi d_{bead} \tag{5.2}$$

Where d_{bead} is the diameter of the bead.

As can be seen from Table 5.1 , when modelling the viscoelastic behaviour of the cytoplasm, it is generally assumed that the viscoelastic parameters are homogeneous and isotropic enough that they can be described with a single value. This will partly be due to the simple fact that most of the used measurement methods are not capable of measuring homogeneity or isotropism. Our measurements will show that generally, the viscoelastic properties are actually highly dependent on place and direction!

5.3. Materials and methods

5.3.1. Magnetic tweezers

Magnetic tweezers with the three-pole configuration were used for the experiments, because of the homogeneity of the magnetic force over a large area (<2.5% deviation within an area of 4×4 μm^2, <20% deviation within an area of 8×8 μm^2; see section 2.6.2). The cell containing the magnetic probe was always positioned in such a way, that the magnetic probe was located as good as possible at the center of poles. The pole height is 6 μm, resulting in a maximum magnetic gradient of 7.5 kT/m.

5.3.2. Magnetic probes

Dynal ‘MyOne’ magnetic beads were chosen as manipulation probes. These beads have a very narrow distribution of their diameter and magnetic moment (5%), and are large enough (1μm) to be clearly visible in white light microscopy. The beads have a relatively low volume magnetisation (28.4 kA/m). The magnetic

tweezers can therefore exert only up to120 pN maximum force on them. This proved to be already much more than required. All experiments were performed at lower amplifier settings yielding 65 pN of magnetic force, unless noted otherwise.
For investigation of bead size dependence of the viscoelastic properties of the cells, also Bangs MC04F/5060 beads with a diameter of 0.35 μm and 47% ferrite content were used. Having a slightly higher volume magnetisation (65 kA/m) forces up to 10pN can be exerted on these beads

5.3.3. Inserting beads into cells

In order to introduce magnetic beads into a living cell we made use of the process of phagocytosis. Granulocytes were isolated from fresh human blood, using a standard density centrifugation protocol from CLB (Central Laboratory Blood transfusion service) at Amsterdam. The magnetic beads are opsonized using blood serum from the same donor in order to promote the phagocytotic process. Beads and cell suspension are then mixed at a 20:1 concentration ratio and incubated for 30 minutes at 37º Celsius. The final solution contains 0.5×10^6 cells/ml PBS-AC buffer. Under these conditions, a large fraction of the cells have just one magnetic bead inside them, as illustrated in Figure 5.2.

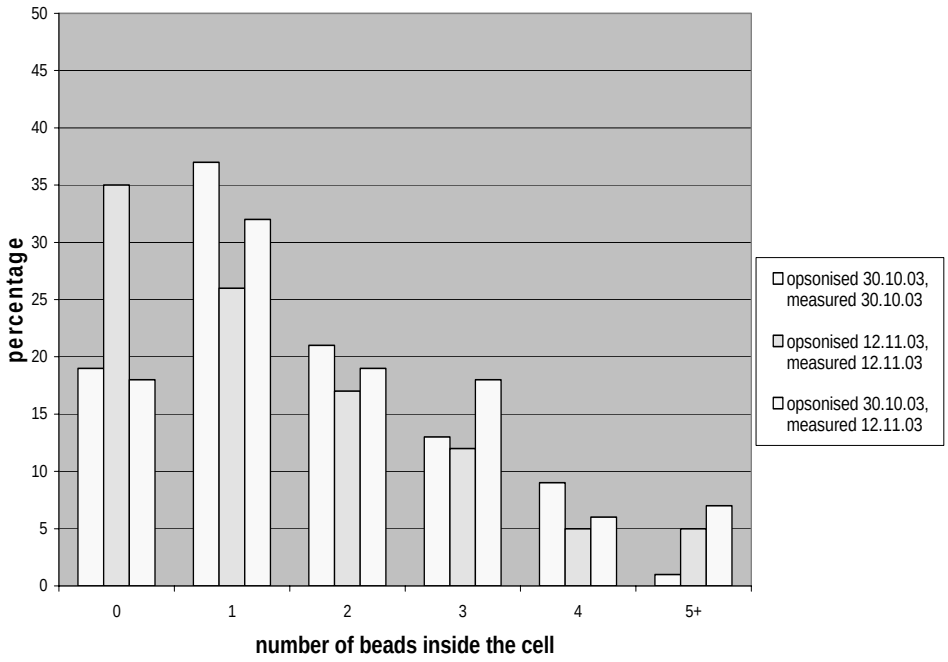

Figure 5.2 Number of Dynal MyOne 1 μm SA coated beads phagocytosed by granulocytes.

A 50 µl droplet of the cell suspension is deposited on glass slides treated with poly-L-lysine, and left to attach for 30 minutes for proper adhesion of the cells to the glass slides. Prior to use, these slides are rinsed with PBS buffer to remove any non-attached cells and beads.

For cells that do not phagocytose, or for measurements done inside the nucleus, the magnetic beads have to be micro injected. Successful microinjection is highly dependent on the combination of bead size and inner diameter of the micro pipette. Obviously a too small inner diameter doesn't work, but also too large a diameter clogs the pipette with multiple beads getting stuck in the opening. For the 0.35 µm beads, micro pipettes with an inner diameter of 0.4 µm (World Precision Instruments, Inc. TIP04TW1F micropipette) were found to give the best results.

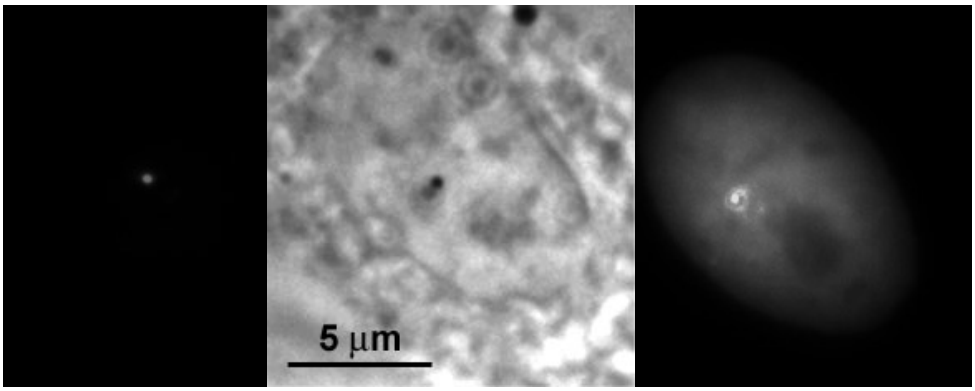

Figure 5.3 Single magnetic bead (0.35 µm) microinjected into the nucleus of a HeLa cell. Images shown are respectively: red fluorescence of the bead, complete cell phase contrast, and green fluorescence of the cell nucleus. (micro injection performed by Dr. B.E. Krenn, Swammerdam Institute for Life Sciences, University of Amsterdam.)

Unfortunately there was no time left to perform manipulation experiments with bead injected into the nucleus of cells. All experiments discussed in the next sections are performed using granulocytes and phagocytosed beads.

5.3.4. Positioning cells between poles

A drop of PBS buffer medium is placed on the substrate containing the magnetic poles. The substrate with the granulocytes is then positioned face-down on top of the magnetic poles, floating on the water layer in between. A sandwich is thus formed, with magnetic poles and cells in between the two glass plates (Figure 5.4). The cell carrying substrate is attached to a micromanipulator, which allows selecting a cell containing a single magnetic probe, and positioning the cell between the magnetic poles. The two glass plates are gently moved towards each

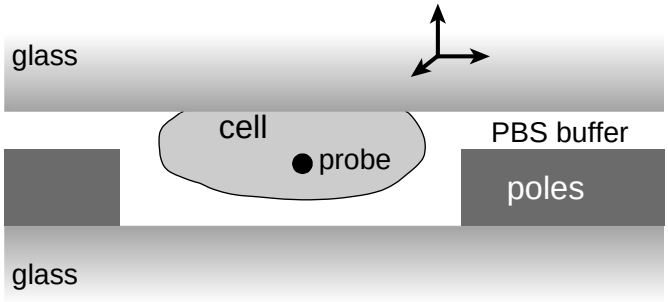

Figure 5.4 Positioning the cell between the poles. Using a micromanipulator, the top substrate can be moved, positioning a cell between the magnetic poles.

other, either by applying pressure, or by using a tissue to remove excess buffer at the edge of the glass substrates.

5.4. Results

In the following sections, intracellular magnetic manipulation experiments within living granulocytes are described. First, it is demonstrated that a bead can be moved and positioned through a cell over long distances. Then, small local movements are used to measure the viscoelastic properties of the cytoplasm. Some cell experiments showed isotropic properties as shown in section 5.4.2, but most experiments actually showed highly anisotropic behaviour, which is discussed in the section afterwards.
We then proceeded into further investigation of the viscoelastic properties, by applying different amounts of force, and decreasing the size of the probe. These experiments are discussed in the final two sections.

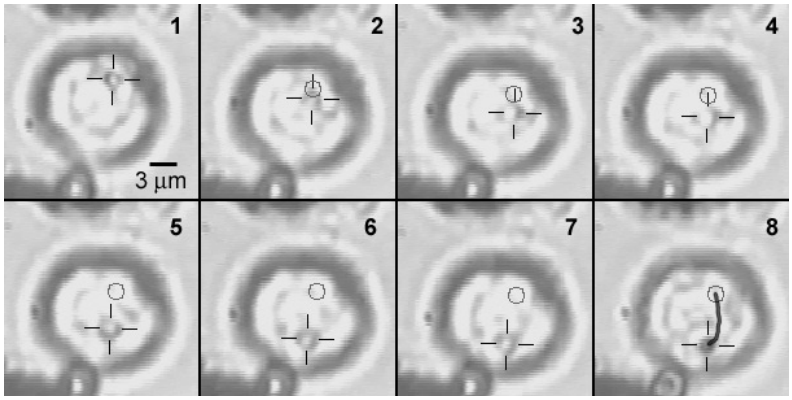

Figure 5.5 Long range movement of a magnetic bead (1µm) through the cell. The bead moved over 6 µm during 20 seconds.

5.4.1. Long range movement

For the first manipulation experiments, it was attempted to simply move the magnetic bead inside the cell. It was found to be possible to move the bead from one side of a granulocyte towards the other side, and back, as shown in the sequence of images in Figure 5.5. During these movements the bead moved over distances of more than 6 μm in the time span of 20 seconds as the result of an exerted force of 60pN. These exercises clearly demonstrate that the magnetic tweezers are able to position beads in arbitrary locations in a cell.

It was also found, that the image analysis algorithm that it used to track the movement of the bead functions best when the bead shows a distinguishing feature. In some cases, when the image is slightly out of focus, the bead looks like a bright spot surrounded by a dark ring, which made it easier for the algorithm to follow. The microscope image is thus not as bad as would appear on the screenshots.

5.4.2. Isotropic viscoelastic properties

To measure the viscoelastic properties of the cytoplasm, the phagocytosed magnetic probe was subjected to an alternating force in the three directions of the

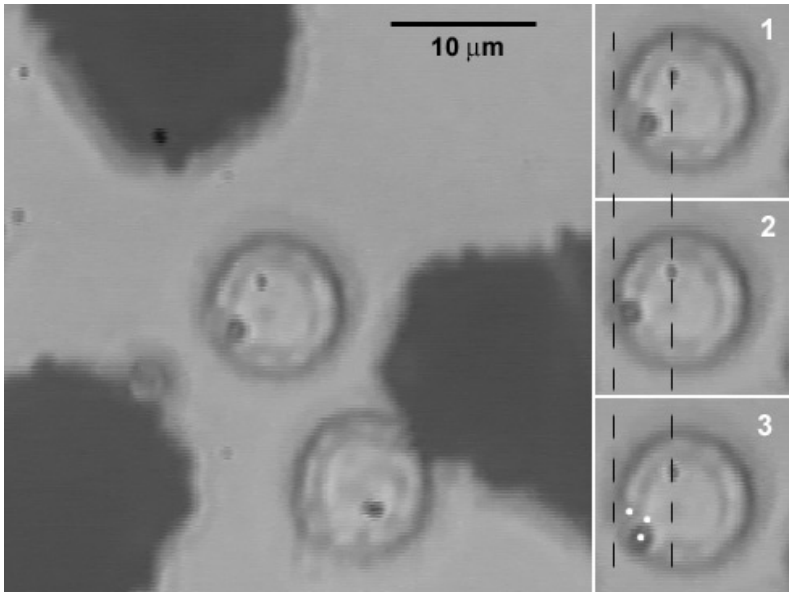

Figure 5.6 Manipulation of a bead (1μm) in a cell. A cell is positioned between the three poles of the mangetic tweezers. Applying a magnetic force displaces the bead with respect to the cell. The pictures to the right show the position corresponding to a force in the direction of the rightmost pole (1), to the top left pole (2) and bottom left pole (3). Guidelines are drawn, showing that the cell is stationary, while the bead moves.

magnetic poles. This magnetic force is produced using a square alternating current of 33% duty cycle at 0.2 Hz. As a result of this exerted force, the bead will start to move in a triangle. The force changes amplitude and direction within one frame of the CCD camera.

Figure 5.6 shows the microscope image collected by the CCD camera. From the images, it can be seen that the bead is moving though the cell, while the cell itself is stationary. The bead movement is analysed off-line using Labview image analysis software.
This viscoelastic behaviour of the cytoplasm becomes clear if the position of the bead is plotted against time. In Figure 5.7 this is shown directly after applying a force.

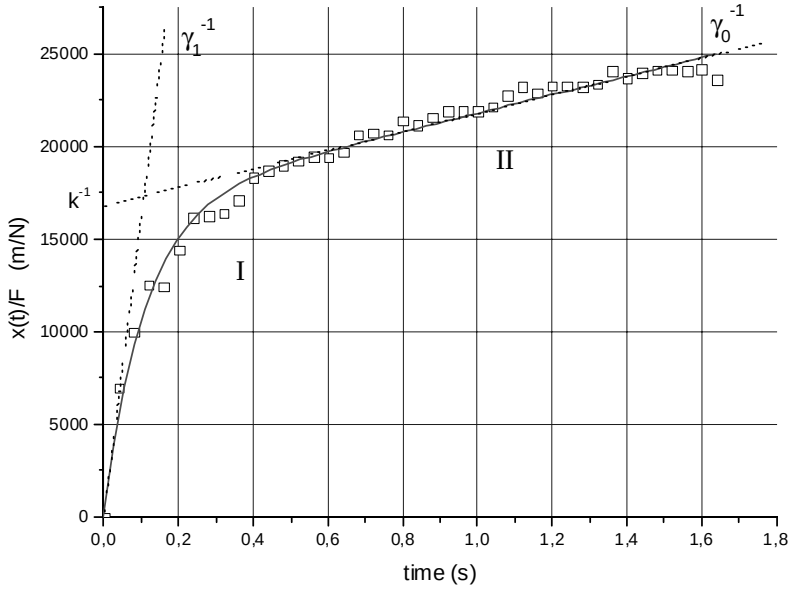

Figure 5.7 Time trace showing the step response of a bead reacting to a change in the magnetic force. The y-axis shows displacement of the bead divided by the force acting on the bead.

The time trace could be described very well by the viscoelastic model as described in section 5.2 . The response of the bead to a step in force can be divided into two regions: (I) The elastic regime, which is governed by the first part of the equation and is described mainly by the elastic properties (k and γ_1) and (II) the viscous regime, for $t > k/\gamma_1$, where the force of the spring equals the magnetic force, and the motion is dictated by the apparent viscosity of the cytoplasm (γ_0).

A curve fit with equation (5.1) yields the corresponding parameters (k, γ_0 and γ_1). The trajectory is characterised by the two tangents with slopes of $^1/\gamma_1$ and $^1/\gamma_0$ and shows a time constant τ of 0.2 seconds.

By exerting an alternating force in three directions, the bead moves along a triangular path. The resulting bead trajectory is shown in Figure 5.8. The magnetic bead is progressing along the triangle anti-clockwise. Being collected by a video camera running at 25Hz, every data point is 0.04 seconds apart. At the corners, the magnetic force changes direction. The result of this experiment clearly shows the performance of the current magnetic tweezers. The bead can be moved in each of the three directions defined by the position of the three magnetic poles enabling 2D manipulation of the bead within the cytoplasm of the cell.

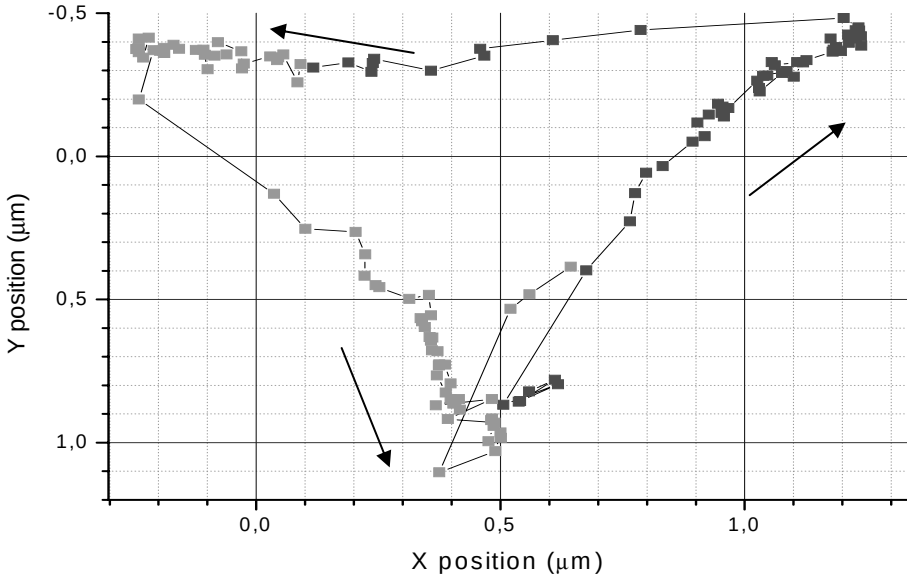

Figure 5.8 trajectory of a bead moving in the cytoplasm of a granulocyte

From Figure 5.8 it is also noticed that the velocity of the bead is not constant over time. Immediately after the force changes direction (at the corners of the triangle), the bead moves relatively fast, primarily as a result of the elastic response from the cytoplasm. Eventually the bead is subjected only to the apparent viscosity of the cytoplasm, and moves linearly towards the attracting pole. Then the force changes again in direction, and the movement is repeated.

The equilateral triangle is evidence that the viscoelastic properties of the cytoplasm are isotropic at the location of the magnetic bead. In Figure 5.9 time traces from 3 consecutive triangles of the bead in the cell are plotted. The three

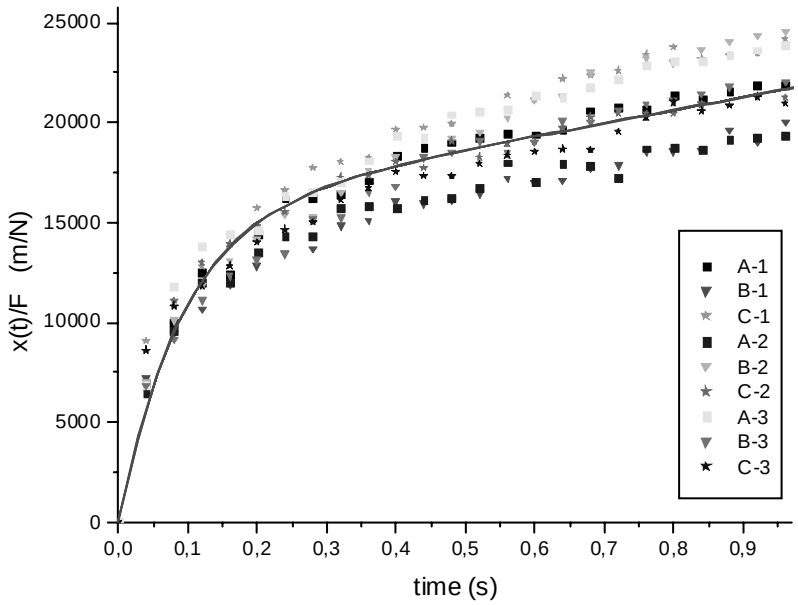

Figure 5.9 Time traces derived from three triangular movements of the magnetic bead in the cell, fitted to the viscoelastic model.

directions in the triangle are denoted by the characters A, B and C, and the triangles counted by numbers. These traces confirm that the viscoelastic properties are probably not place or direction dependent over a distance of 1.5 μm in the measurement area.

The viscoelastic model was fitted to these nine traces, giving average values for the model parameters, and allowing calculation of the viscosities η_0 and η_1.

Table 5.2 Summary of the viscoelastic properties obtained by curve-fitting the nine experimental traces as shown in Figure 5.9

γ_0	γ_1	k	τ	η_0	η_1	μ
$\times 10^{-6}$ Pa·s·m	$\times 10^{-6}$ Pa·s·m	$\times 10^{-6}$ Pa·m	s	Pa·s	Pa·s	Pa
152 ± 6	5.9 ± 0.3	65 ± 1	0.91 ± 0.02	16.1 ± 0.6	0.63 ± 0.03	6.9 ± 0.1

Using the parameters of Table 5.2, it is possible to reconstruct the 2D movement of the bead in the cytoplasm. Figure 5.10 compares this calculated trajectory using the viscoelastic model with the actual measured movement. The calculated trajectory is in very good agreement with the measured data (especially the observed “knee” in the legs of the triangles are very well described), confirming

the validity of the model which assumes isotropic viscoelastic properties in the region where the bead is moving.
In contrast with these observations, also bead trajectories were observed that moved in different ways. In those cases, the movement seemed to be restricted by internal cellular structures. These results are described next.

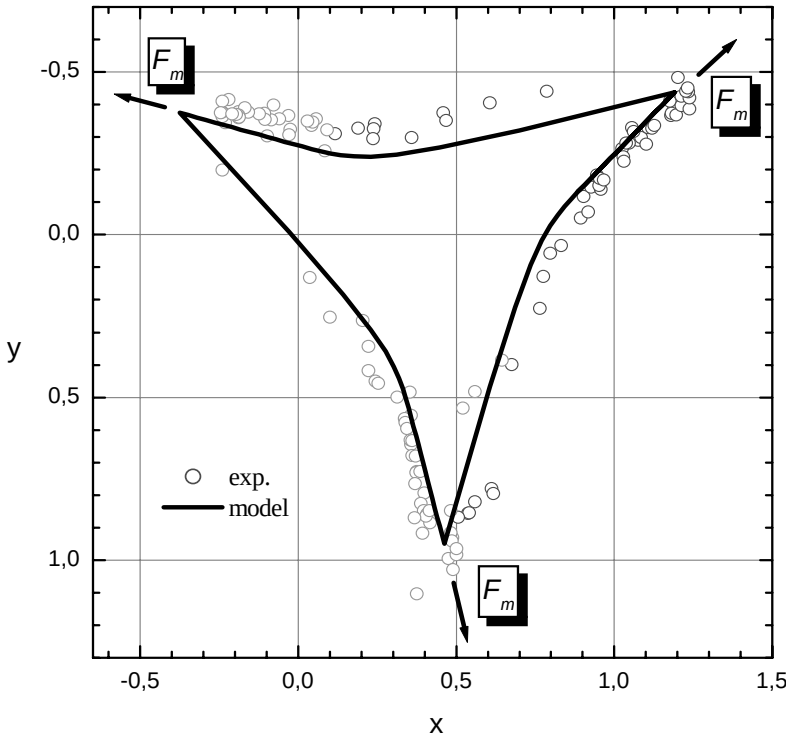

Figure 5.10 Measured bead trajectory, compared to the trajectory calculated via the viscoelastic model. Arrows indicate the direction of the force

5.4.3. Anisotropic viscoelastic properties

The magnetic tweezers are able to measure local properties, including directional dependence. A magnetic bead was manoeuvred further into the cell, in the direction of the cell nucleus. An alternating force in three directions (33% duty cycle, 0.5 Hz) was exerted on the probe. In this region inside the cell, the viscoelastic properties of the environment are clearly no longer isotropic, which results in a deformed triangle (Figure 5.11).

The cell nucleus was located at the top right corner of this graph. Movement in this direction is clearly restricted, while movement along the edge of the nucleus is allowed. This difference can also be seen looking at the time traces for each leg

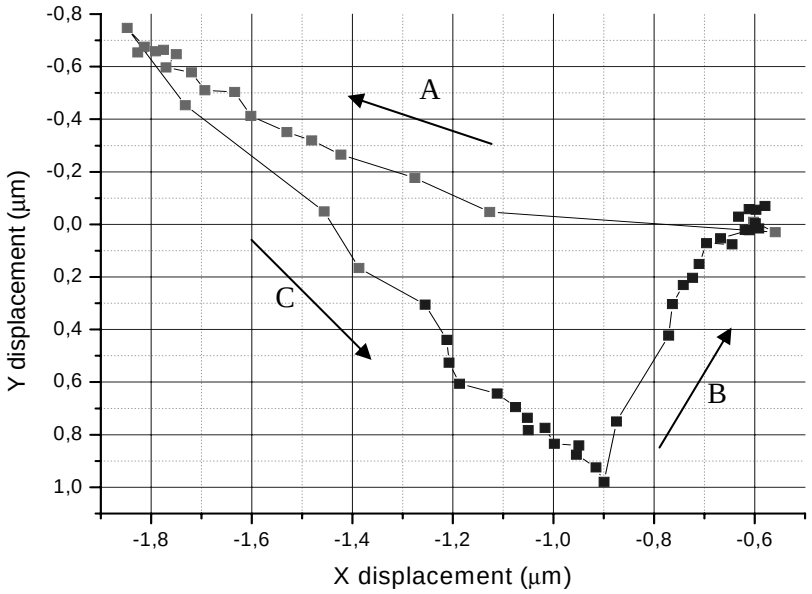

Figure 5.11 bead trajectory near the cell nucleus.

of the triangle (Figure 5.12). Again the results of three consecutive triangular movements are shown, where the characters indicate direction corresponding to Figure 5.11.

Clearly three distinct groups of time traces can be distinguished: one for each leg of the triangular movement. Traces **B** correspond to movement directly towards the nucleus. Traces **A** correspond to movement away and along the edge of the nucleus, and traces **C** correspond to movement farthest away from the nucleus.

Table 5.3 Summary of the viscoelastic model parameters obtained by curve fitting of experimental results from Figure 5.12

	A	**B**	**C**	
γ_0	55 ± 4	167 ± 39	55 ± 4	$\times 10^{-6}$ Pa·s·m
γ_1	6.5 ± 0.3	3.6 ± 0.3	5.6 ± 0.3	$\times 10^{-6}$ Pa·s·m
k	68 ± 3	69 ± 3	42 ± 3	$\times 10^{-6}$ Pa·m
τ	96 ± 8	52 ± 7	133 ± 17	$\times 10^{-3}$ s
η_0	5.8 ± 0.4	17.7 ± 4.1	5.8 ± 0.4	Pa·s
η_1	0.69 ± 0.03	0.38 ± 0.03	0.59 ± 0.03	Pa·s
μ	7.2 ± 0.3	7.3 ± 0.3	4.5 ± 0.3	Pa

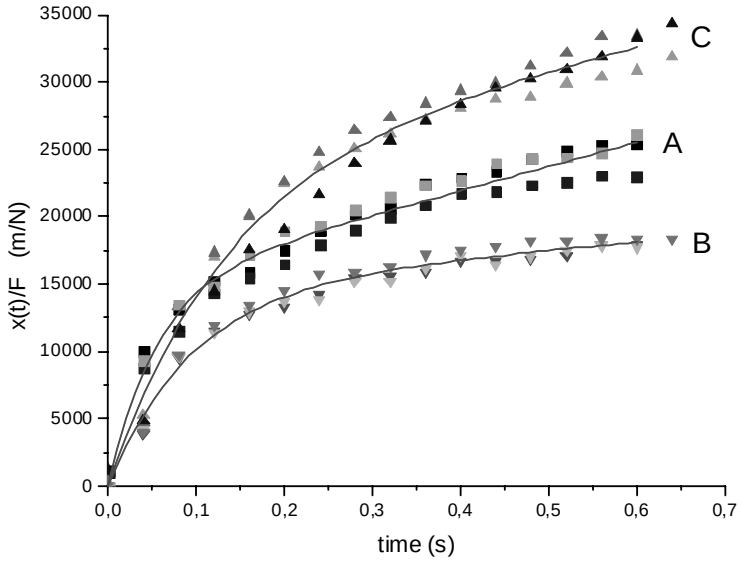

Figure 5.12 time traces of a bead near the cell nucleus

When comparing the properties for the different directions, it is noticed that the apparent viscosity η_0 is higher when approaching the nucleus (trace B). This is consistent with the bead moving into a more dense structure. Also, the elasticity in this region is higher. Because the first part of the time trace is dominated by elastic effects, trace A also shows influence of this higher elasticity. Also visible is that the triangular trajectory is independent of the time, as consecutive time traces can be overlaid.

5.4.4. Force dependence of the viscosity

To investigate the possible force dependence of the apparent viscosity, the viscosity measurements performed earlier have been repeated using various levels of force to move the bead, by varying the current through the coils. Each experiment was started by moving the bead at low force. After enough triangular cycles had been recorded, the force on the bead was increased in steps until the maximum force was achieved. The frequency of the direction changes in force was lowered, so that a complete triangular trajectory took 10 seconds, producing time traces with longer viscous regions. Figure 5.13 shows the results of the force measurements for three cells from the same donor. For each force regime, three viscosities are plotted, corresponding to the three directions of movement. Each point is the result of an average over several time traces.

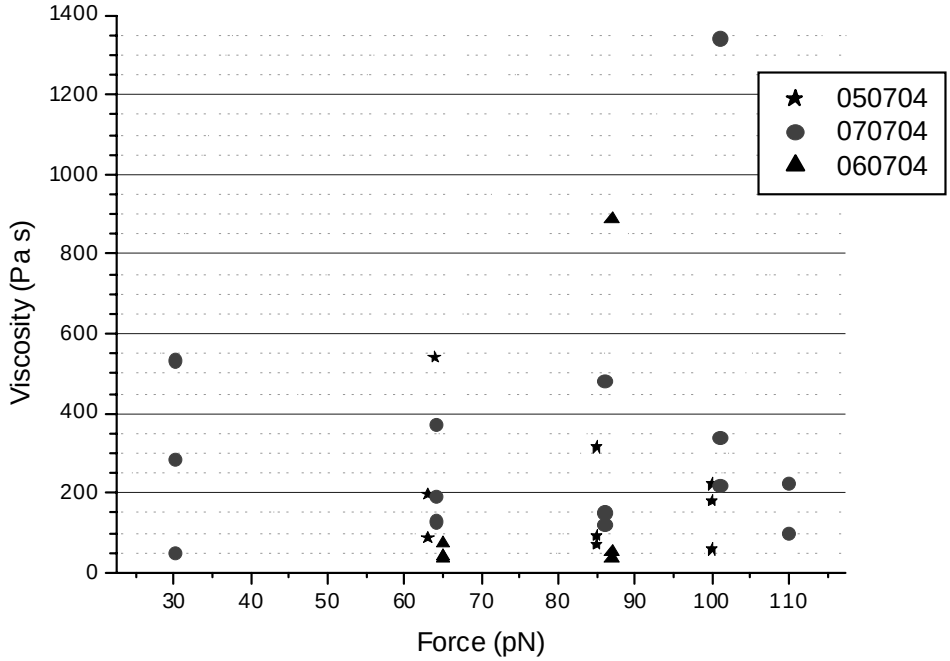

Figure 5.13 Dependence of the apparent cell viscosity on the applied force on the bead. The three series indicate three different cells. For each of them viscoelastic properties along the three paths of movement were measured under various forces.

Most cells showed highly anisotropic viscoelastic properties, producing trajectories like those described in section 5.4.3. Therefore, the three directions of movement resulted in three different apparent cell viscosities. As can be seen in Figure 5.13 in some cases the bead was predominantly moving along one axis, producing two low values for the apparent viscosity, and one high value.
What is not seen however is a strong influence of the force on the magnetic bead on the measured apparent viscosity. A possible explanation of these results is presented in section 5.5.

5.4.5. Manipulation using smaller beads

Finally also measurements have been performed using smaller beads of 0.35 μm diameter. Because of the smaller magnetic moment of these beads, the applied force was only 5.4 pN. Due to the size of the beads, these were less easy to follow when using bright field microscopy. The few complete traces that could be analysed by the Labview image analyses program showed anisotropic movements similar to those described in section 5.4.3. From these traces the following parameters were measured:

Table 5.4 Summary of the viscoelastic properties of the cytoplasm measured using beads of 0.35 μm pulled through the cell at 5.4 pN magnetic force.

	A	B	C	
γ_0	39 ± 7	184 ± 98	21 ± 2	$\times 10^{-6}$ Pa·s·m
γ_1	3.4 ± 0.2	7.2 ± 1.4	2.6 ± 0.3	$\times 10^{-6}$ Pa·s·m
k	14 ± 1	39 ± 5	17 ± 1	$\times 10^{-6}$ Pa·m
τ	0.24 ± 0.03	0.19 ± 0.06	0.15 ± 0.03	S
η_0	12 ± 2	56 ± 30	6.4 ± 0.7	Pa·s
η_1	1.0 ± 0.1	2.2 ± 0.4	0.8 ± 0.1	Pa·s
μ	4.2 ± 0.3	12 ± 2	5.0 ± 0.4	Pa

From these values it is concluded that the viscoelastic properties found using these small beads do not seem to differ significantly from the results with large beads. However, most experiments with these small beads showed a much greater bead velocity. Unfortunately, no complete triangular trajectories could be found, as the image analysis algorithm continuously lost track of the bead. Yet single complete time traces could be found, examples of which are shown in Figure 5.14.

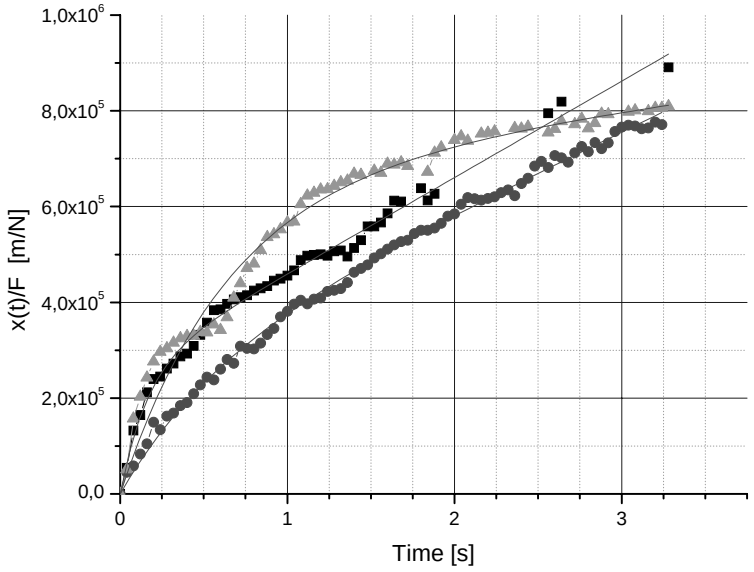

Figure 5.14 individual time traces for a 0.35μm bead in a cell

From these traces the viscoelastic properties of the cytoplasm could be determined. However, one should take into mind that these values, and their

errors, are determined from individual time traces, and not the average from a sequence of consecutive triangular trajectories.

Table 5.5 viscoelastic properties derived from individual time traces of a 0.35μm bead in a cell

	γ_0	γ_1	k	η_0	η_1	μ
	$\times 10^{-6}$ Pa·s·m	$\times 10^{-6}$ Pa·s·m	$\times 10^{-6}$ Pa·m	Pa·s	Pa·s	Pa
1	5.0 ± 0.2	0.62 ± 0.06	3.9 ± 0.1	1.5 ± 0.1	0.19 ± 0.02	1.2 ± 0.1
2	5.9 ± 0.3	2.3 ± 0.2	4.0 ± 0.4	1.8 ± 0.1	0.69 ± 0.05	1.2 ± 0.1
3	21 ± 5	0.98 ± 0.02	1.5 ± 7.8	6.3 ± 1.5	0.3 ± 0.01	0.46 ± 0.02

It is seen that the apparent cell viscosity η_0 and the elasticity μ are considerably lower for smaller beads than for bigger beads. However, the viscosity η_1 does not deviate significantly from the values found for larger beads. That the apparent cell viscosity η_0 and elasticity are bead size dependent is no surprise. They are probably strongly influenced by the cytoskeleton, which has a finite mesh size. Beads that are smaller than the mesh will pass almost unhindered through the skeleton. Apparently beads of 0.35 μm are small enough that the mesh size starts to influence the apparent viscosity.

5.5. Discussion and Conclusions

The experiments that have been performed show the possibility of manipulating particles in living cells using magnetic tweezers. Magnetic probes could be inserted into cells both using phagocytosis and microinjection. Magnetic probes of 1 μm diameter could be moved to any location in the cell cytoplasm, moving over distances of over 6μm with a force of 60pN reaching speeds up to 0.4 μm/s. Most importantly, it was shown that a bead with a diameter of 0.35 μm could be moved easily through the cell at a velocity of 1 μm/s by as little as 5 pN applied force.

Quantitative data about the viscoelastic properties of the cytoplasm has been measured. The measured apparent cell viscosity η_0 and elasticity μ fall in the range of reported values in literature for cells that are comparable to granulocytes, like macrophages, leukocytes and neutrophils (Table 5.1). Subsequent entry of the measured properties into the model, allowed to reproduce the recorded bead trajectories for the isotropic regions of the cell.

Due to the possibility to manoeuvre the magnetic probe to different locations inside the cell, the viscoelastic properties could be determined both in relatively isotropic regions, as well as close to the nucleus. This allowed investigating the homogeneity of the cytoplasm. Because the tweezers form a multi-directional manipulator, the *(an)isotropy* of the cytoplasm close to the cell nucleus could also be investigated. This is impossible with any of the other techniques used to measure cell viscosity. The heterogeneity and especially the anisotropy of the cytoplasm were found to have enormous influence on the measured viscoelastic properties, and are probably responsible for the large spread in reported values for viscoelastic properties in literature.

The influence of force and bead size on the apparent viscosity has been studied. From the data collected, no force dependence could be found within the force regime of 30 to 110pN. Future experiments should further investigate the influence of force by extending the range over which is measured. In addition, drugs that selectively disrupt specific parts of the cytoskeleton can be added to distinguish between the contribution of different parts of the cytoskeleton to the viscoelastic properties.
The bead size (1.0 – 0.35μm) did influence the apparent viscosity in a number of experiments, but more experiments are necessary to draw definite conclusions. To better follow these small beads, an image should be produced that makes it easier to separate the bead from the environment, and thus follow it automatically using image analysis software. This could for example be done using fluorescence or phase contrast microscopy.

There may be a number of explanations for the absence of force dependence in the apparent cell viscosity. First of all, it is of course possible that different types of cells or different positions inside the cells show different behaviour in this aspect of the viscosity. The values reported in literature for force dependence were measured in macrophages, while our experiments were performed on granulocytes.
Secondly, while entanglement would predict a stiffening of the cytoskeleton for higher force, the cross-link argument predicts a weakening of the cytoskeleton. These two effects might thus cancel each other in the force regime that was used. It is interesting to try to estimate the influences of these two effects, to see if this explanation can hold any ground.

The force dependence for the cross links can be estimated using the Arrhenius-Kramer equation. This equation describes the probability *p* of breaking molecular bonds:

$$p(F) = p_0 \exp\left[-\frac{\Delta g - W}{k_B T}\right] \quad with \quad W = F\xi \tag{5.3}$$

which can be rewritten to

$$p(F) = C_1 \exp\left[\frac{F\xi}{k_B T}\right] \quad with \quad C_1 = p_0 \exp\left[\frac{\Delta g}{k_B T}\right] \tag{5.4}$$

where k_B is the Boltzmann constant, T the temperature, and C_1 a constant describing the energy profile of the molecule, which is unknown. The parameter W is indicative of the amount of work necessary to break the bond, which can be split into the multiplication of: F the force acting on the bond, and a distance ξ, which is sometimes interpreted as the distance over which this force works.
Assuming that the velocity at which the bead moves is proportional to the probability of breaking of crosslinks, $k(F)$ can than be inserted into the equation relating speed to viscosity:

$$v = \frac{F}{3\pi\eta d} \tag{5.5}$$

with η the viscosity, d the diameter of the bead (1μm) and v the speed of the bead. Rewriting and combining the constants yields an equation that describes how the viscosity is dependent on the force in case the breaking of molecular bonds is the main contributor:

$$\eta = C \frac{F}{\exp\left[\frac{F\xi}{k_B T}\right]} \tag{5.6}$$

Although there are very many unknown parameters in de the derivation, almost all of them only influence the constant C. The only remaining unknown parameter is ξ. For molecular bonds this is typically in the order of 10^{-10} metre. The curve shown in Figure 5.15 was constructed using $\xi = 1.0\times10^{-10}$ and $C = 2\times10^{12}$.

No model exists to describe the effect of entanglement. However, the data collected by [17] is suggestive of a linear dependence of viscosity on force. Lacking any real model, such a linear dependence is also plotted in Figure 5.15.

The two curves describing the possible different force dependences of the viscosity can then be added to derive a model for the total force dependence of the viscosity. This approach seems to be able to qualitatively describe the measured effect where at higher forces a strong dependence on force is found, while at the lower forces we have used, a plateau is formed, and no dependence can be seen.

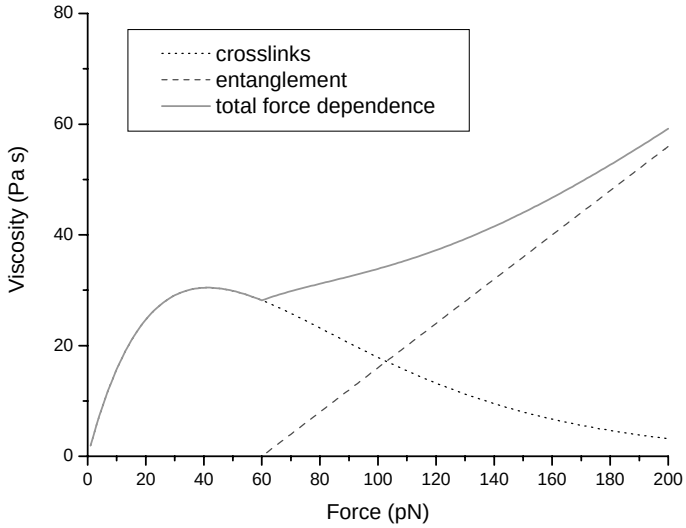

Figure 5.15 Possible explanation of the apparent absence of force dependence in the measured force regime, where the effects of entanglement and crosslink breakage cancel out.

Of course, there are far too many unknowns in this approach to give any definite answers. However, with this possible explanation in mind, one can devise new experiments, that might validate it. Drugs that selectively disrupt specific parts of the cytoskeleton, for example the cross-links between actin filaments, can be added. In this way, a distinction between the contributions of different parts of the cytoskeleton to the viscoelastic properties can be made.

5.6. References

1 A.R. Bausch, W. Möller, E. Sackmann, 1999, **Measurement of local viscosity and forces in living cells by magnetic tweezers**, *Biophysical Journal*, 76:573-579

2 S. Yamada, D. Wirtz, S.C. Kuo, 2000, **Mechanics of living cells measured by laser tracking microrheology**, *Biophysical Journal*, 78:1736-1747

3 N. Wang, J.P. Butler, D.E. Ingber. 1993.**Mechanotransduction across the cell surface and through the cytoskeleton**. *Science*. 260:1124-1127.

4 K.-L. P. Sung, C. Dong, G.W. Schmid-Schönbein, S. Chien, R. Skalak. 1988. **Leukocyte relaxation properties**, *Biophys. J*. 54:331-336

5 M.A. Tsai, R.S. Frank, R.E. Waugh, 1994. **Passive mechanical behavior of human neutrophils: effect of cytochalasin B**. *Biophys. J.* 66:2166-2172

6 G.I. Zahalak, W.B. McConnaughey, E.L. Elson. 1990. **Determination of cellular mechanical properties by cell poking, with an application to leukocytes**. *J. Biomech. Eng*, 112:283-294.

7 M. Radmacher, M. Fritz, C.M. Kacher, J.P. Cleveland, P.K. Hansma, 1996. **Measuring the viscoelastic properties of human platelets with the atomic force microscope**. *Biophys J*. 70:556-567

8 O. Thoumine, A. Ott, 1997. **Time scale dependent viscoelastic and contractile regimes in fibroblasts probed by microplate manipulation**. *J. Cell. Sci*. 110:2109-2116

9 G. K. Ragsdale, J. Phelps, K. Luby-Phelps. 1997. **Viscoelastic response of fibroblasts to tension transmitted through adherens junctions**. *Biophys. J*. 73:2798-2808

10 A.R. Bausch, F. Ziemann, A.A. Boulbitch, K. Jacobsen, E. Sackmann. 1998. **Local measurements of viscoelastic parameters of adherent cell surfaces by magnetic bead microrheometry**. *Biophys. J.* 75:2038-2049.

11 M. Sato, T.Z. Wong, D.T. Brown, R.D. Allen. 1984. **Rheological properties of living cytoplasm: Preliminary investigation of squid axoplasm (Loligo pealei)**. *Cell Motil*. 4:7-23

12 Y. Hiramato. 1969 **Mechanical properties of the protoplasm of the sea urchin egg. I. Unfertilized egg**. *Exp. Cell Res*. 56:201-208

13 Y. Hiramato. 1969 **Mechanical properties of the protoplasm of the sea urchin egg. II. Fertilized egg**. *Exp. Cell Res*. 56:209-218

14 P.A. Valberg, D.F. Albertini. 1985. **Cytoplasmic motions, rheology, and structure probed by a novel magnetic particle method.** *J. Cell. Biology*. 101:130-140

15 P.A. Valberg, J.P. Butler. 1987. **Magnetic particle motions within living cells. Physical Theory and techniques**. *Biophys J*. 52:537-550

16 P.A. Valberg, H.A. Feldman, 1987. **Magnetic particle motions within living cells. Measurement of cytoplasmic viscosity and motile assay**. *Biophys. J.* 52:551-69

17 W. Feneberg, M. Westphal, E. Sackmann. 2001 **Dictyostelium cells' cytoplasm as an active viscoplastic body** *European Biophysics Journal with Biophysics letters*. 30:284-294

6. Preliminary results inside the cell nucleus

6.1. Introduction

After the thesis concept was written, some more cell experiments were performed. A magnetic bead was inserted into the nucleus of a HeLa cell and subsequently this bead was moved in several directions using the magnetic tweezers. The resulting data was used to determine the viscoelastic properties of the chromatin interior inside the cell nucleus. To the best of our knowledge, this is the first report on in vivo nano-manipulation experiments performed inside the nucleus of a living cell! Therefore, although the results are preliminary, it was found prudent to include these experiments.

6.2. Materials and Methods

6.2.1. Magnetic tweezers and probes

Magnetic tweezers with the three-pole configuration were used for the experiments, because of the homogeneity of the magnetic force over a large area (<2.5% deviation within an area of 4×4 μm^2, <20% deviation within an area of 8×8 μm^2; see section 2.6.2). The cell containing the magnetic probe was always positioned in such a way, that the magnetic probe was located as good as possible at the centre of poles. The pole height is 6 μm, resulting in a maximum magnetic gradient of 7.5 kT/m.

Dynal ‘MyOne’ magnetic beads were chosen as manipulation probes. These beads have a very narrow distribution of their diameter and magnetic moment (5%), and are large enough (1μm) to be clearly visible in bright field microscopy. The beads have a relatively low volume magnetisation (28.4 kA/m) corresponding to a maximum achievable force of 120 pN.

6.2.2. Cell preparation

HeLa cells were used for these experiments, because of the large and easy to identify nucleus. The HeLa cell line used is genetically modified with a H2B-GFP vector, so that the location of the chromatin can be visualised using a fluorescence microscope.
Cells are deposited on 12 mm diameter round glass coverslips (Eppendorf Cellocate) and left for two hours to attach and spread. These Cellocate are sterile cover slips, with a micro grid design (55 μm grid size) that allows for quick location of individual microinjected cells.

6.2.3. Bead Injection into the nucleus

Bead injection is performed using micropipettes with an inner diameter of 0.4 µm (World Precision Instruments, Inc. TIP04TW1F micropipette), connected to an Eppendorf FemtoJet microinjector to control the pressure. The micropipettes are attached to a micromanipulator allowing 3D movement of the pipette tip.

A cover slip containing HeLa cells is placed into a Petri dish of 3 cm diameter. The dish is then filled with medium to approximately 3 mm height. A small droplet of magnetic beads (10^6 beads/ml) is dropped on the location of the cover slip, such that only a few beads are located close to the cells.
Because the magnetic beads are larger than the micropipette, a single magnetic bead can be sucked onto the tip of a micropipette. By varying the 'compensation pressure' (~ 50 to 150 hPa) an influx of medium into the pipette is realized, allowing to capture a bead onto the tip. Next, the bead is pushed into the nucleus of a selected HeLa cell using the micromanipulator. Once the bead is in the nucleus, the compensation pressure is increased to normal pressure (~300 hPa) releasing the bead. Optionally an additional small injection pulse (~600hPa, 0.1s) is given, to release the bead from the pipette tip.

The cover slip is then removed from the Petri dish, and placed up-side down onto the magnetic poles. Using the micro grid, the injected cell is relocated and the cell of interest is manoeuvred between the magnetic poles by moving the cover slip using a micromanipulator.

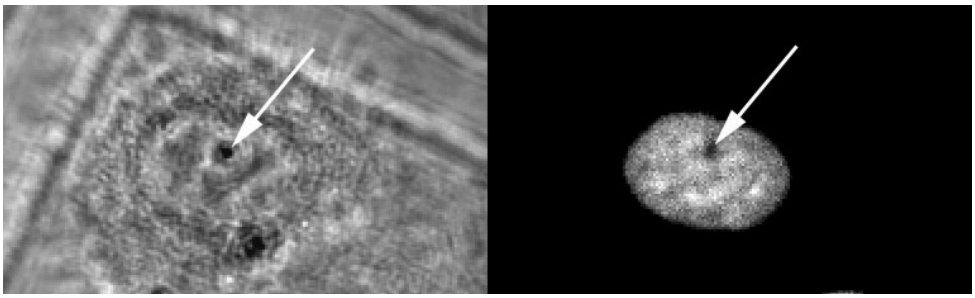

Figure 6.1 Confocal Microscopy images of a magnetic bead injected into the nucleus of a Hela H2B-GFP cell. Shown left is the transmitted light image, while the image on the right shows the GFP (green fluorescent protein) fluorescence signal from the DNA in the nucleus. (exc. 488 nm) Clearly visible in both images is the dark spot, indicated with the arrows, which shows the position of the magnetic bead.

6.3. Results

Magnetic beads were successfully injected into the nucleus of HeLa cells using the method described above. The location of the bead with respect to the nucleus was determined in a Zeiss LSM 510 confocal microscope. A confocal slice of a bead inside the nucleus of a HeLa cell is shown in Figure 6.1.

The magnetic probe was subjected to an alternating force in the three directions of the magnetic poles. This magnetic force of 110 pN is produced using a square alternating current of 33% duty cycle at 0.1 Hz. This results in movements in three directions, producing a triangular trajectory every ten seconds.

Out of the four measured cells, two showed bead movement when the magnetic force was applied. However, even with the high magnetic force (110 pN) applied on it, the total displacement of the bead was very small (~ 0.2 μm). Because of this, drift was a significant factor determining the displacement of the bead. To compensate for the drift, the movement of the cell itself was also measured by following a recognizable region of it, and subtracted from the measured bead displacement. This procedure results in the movement of the bead relative to the cell, an example of which is shown in Figure 6.2.

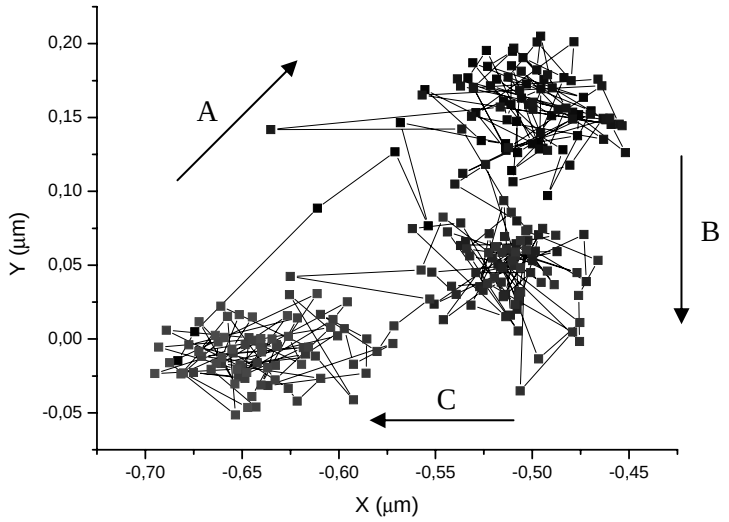

Figure 6.2 Induced movement of a magnetic bead in the nucleus of a Hela cell. The bead describes a triangular trajectory in the direction of the arrows. One complete triangle (corresponding to 10 seconds measuring time) is shown.

The movement of the bead within the nucleus of the cell was very stable, allowing measuring times of several minutes, corresponding to twenty cycles. No change in the movement of the bead relative to the cell was observed during the measurement.

It is clear that the movement in the nucleus is completely different from the movement seen in the cytoplasm of cell, as discussed in the previous chapter. While in the cytoplasm the bead showed viscous movement through the medium, in the nucleus the bead seems to be stuck, and only shows elastic movement. This behaviour can be better analysed by looking at the time traces corresponding to the movement.

The corresponding time traces for the movement along the leg of the triangular trajectory are shown in Figure 6.3.

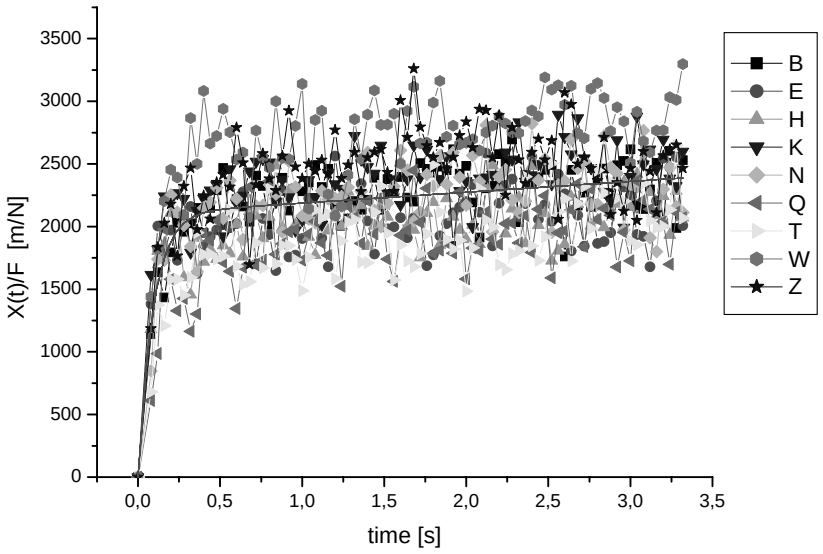

Figure 6.3 Time traces of the induced movement of a magnetic bead in the nucleus of a Hela cell. Traces are shown for one leg of 9 consecutive triangular trajectories. All traces are in the direction 'A' as indicated in Figure 6.2.

Using the same viscoelastic model as used to describe the behaviour in the cytoplasm (see chapter 5), both elasticity and viscosity can be derived. The results are shown in Table 6.1.

Table 6.1 Viscoelastic properties of the nucleus of HeLa cells calculated for the three directions of movement of the magnetic bead

	A	B	C	
γ_0	12 ± 2	5.7 ± 0.6	29 ± 9	$\times 10^{-3}$ Pa·s·m
γ_1	26 ± 2	45 ± 8	55 ± 7	$\times 10^{-6}$ Pa·s·m
k	280 ± 4	492 ± 15	624 ± 14	$\times 10^{-6}$ Pa·m
τ	91 ± 9	92 ± 18	89 ± 13	$\times 10^{-3}$ s
η_0	1.2 ± 0.2	0.58 ± 0.01	3.0 ± 0.9	$\times 10^{3}$ Pa·s
η_1	2.6 ± 0.2	4.6 ± 0.8	5.6 ± 0.7	Pa·s
μ	28.3 ± 0.4	45 ± 2	63 ± 2	Pa

The elasticity μ and corresponding viscosity η_1 are roughly one order of magnitude higher than that measured in the cytoplasm of granulocytes in chapter 5. The apparent viscosity η_0 is between two and three orders of magnitude higher than in the cytoplasm!

6.4. Discussion and conclusions

These experiments show that the developed magnetic tweezers technology is not only able to perform nano-manipulation inside the cytoplasm of living cells, but can also be used inside the *nucleus* of a living cell. Magnetic beads were successfully inserted into the nucleus of HeLa cells, and subsequently manipulated using the magnetic tweezers. To the best of our knowledge, this is the first in vivo nano-manipulation experiment performed inside the nucleus of a living cell!

Although yet only few cells have been measured with this system, even from these preliminary experiments it is already clear that the contents of the cell nucleus exhibit very different viscoelastic properties than the cytoplasm. For the bead size used (1μm diameter), it is much stiffer, and has such a high apparent viscosity that beads hardly move at all.

It is difficult to relate these results to literature because until now no instrumentation existed to measure the mechanical properties of interphase chromosomes in vivo. Work has been done on *mitotic* chromosomes, which were either reconstituted [1] or extracted from cells during (pro)metaphase [2,3,4]. These references calculated a Young's Modulus for the mitotic chromosome between 10^2 and 10^3 Pa, resulting from the entropic elasticity of the DNA fibres.

To relate these numbers to our own experiments, we can try to calculate the Young's Modules *Y* of the interphase DNA structures.

The meaning of the Young's Modules *Y* comes from the force needed to stretch a uniform elastic rod of length *L* by a distance ΔL [5]:

$$F = \pi r^2 Y \frac{\Delta L}{L} \tag{6.1}$$

where *F* is the force, πr^2 the cross section of the rod and *Y* the Young's Modulus. This can be rewritten to:

$$Y = \frac{Lk}{\pi r^2} \tag{6.2}$$

Where *k* is the measured spring constant.

Assuming that the diameter of the inserted magnetic bead determines the cross section of the compressed DNA (thus an effective cross section of 1 μm diameter) and taking the length *L* as 4 μm (approximate radius of the nucleus) yields a Young's Modulus of $2.4 \pm 0.8 \times 10^3$ Pa. This is quite high, considering that the structure of interphase DNA is supposed to be more open than in the mitotic state, and thus one would expect a lower stiffness. However, one might well argue that the bead is not only pushing to one side, but also pulling from the other, effectively halving the calculated Young's Modulus. In addition, the cross section of the chromatin affected by the bead could be considerably larger due to cross linkages and other higher order structures.

6.5. References

1 B. Houchmandzadeh, S. Dimitrov, 1999, **Elasticity measurements show the existence of this rigid cores inside mitotic chromosomes**. *Journal of Cell Biology*, 145:215-233

2 B. Houchmandzadeh, J.F. Marko, D. Chatenay, A. Libchaber, 1997, **Elasticity and structure of eukaryote chromosomes studied by micro-manipulation and micropipette aspiration**. *Journal of Cell Biology*, 139:1-12

3 M.G. Porrier, S. Eroglu, D. Chatenay, J.F. Marko, 2000, **Reversible and irreversible unfolding of mitotic chromosomes by applied force**. *Mol. Biol. Cell*, 11:269-276

4 M.G. Porrier, J.F. Marko, 2002, **Bending rigidity of Mitotic chromosomes**. *Mol. Biol. Cell*. 13:2170-2179

5 L.D. Landau, I.M. Lifshitz, 1986, **Theory of Elasticity**, *Pergamon, New York.*

7. Conclusions & Outlook

7.1. Conclusions

In this thesis, magnetic tweezers technology that enables the possibility for nano-manipulation inside living cells has been developed. A working prototype of an intracellular manipulator was built that provided proof-of-principle for doing in vivo intracellular nano-manipulation. It is evident that this is a viable approach for doing new kinds of experiments; position and force controlled measurements of molecular interactions are now within reach.

Micrometre scale magnetic poles turned out to be essential to produce the required magnetic gradient, and a pole configuration consisting of three poles was found to be optimal for producing a homogeneous force over a large area.
Producing these magnetic poles yielded a number of challenges and in the end required the development of a new micromachining technique to electroplate thick magnetic structures on glass substrates. Cobalt was used for the magnetic poles, because of the good combination of magnetic and mechanical properties as well as its biocompatibility compared to other ferromagnetic materials. Biocompatibility could be further enhanced by optionally applying a PLA coating, even allowing to culture cells directly on the substrates containing the magnetic poles.

The resulting magnetic tweezers were found to produce a gradient of 7.5 kT/m, which confirmed the predictions from the theoretical calculations. Currently the photoresist mask is limiting the maximum pole height, lowering the achievable magnetic gradient. From the theoretical calculations, it is predicted that gradients as high as 30 kT/m should be attainable, by increasing the height of the poles, and optimizing magnetic properties of the electroplated cobalt.
The currently achieved gradient already allows forces of 10 pN on commercially available magnetic Fe_3O_4 beads of 150 nm diameter. With the predicted gradient 30kT/m for improved poles, such a force would be achieved with an iron bead of 70 nm diameter.

The magnetic tweezers have been tested by manipulating magnetic beads inside living granulocytes. The 1μm sized beads had low magnetic moment, allowing to exert up to 120 pN of force, and were brought into the cell by phagocytosis. Not only has force exertion resulting in bead movement been demonstrated, but the magnetic tweezers were also successfully used to measure the viscoelastic properties of the cytoplasm under much more controlled circumstances than was

possible before. Using the unique capabilities of the instruments, it was shown that the viscoelastic properties of the cytoplasm are not only very inhomogeneous, but also extremely anisotropic. This anisotropy resulted in variations for the viscoelastic properties of an order of magnitude and more. The apparent viscosity could vary from 50 to 550 Pa·s, in a measurement area of less than a micrometre diameter, only due to the difference in the direction of the exerted force.
The use of smaller beads (350nm) indicated that intracellular manipulation in the cytoplasm was easily possible with forces as low as 5 pN. Because of time limits, we could not yet start using the magnetic tweezers for manipulating beads inside the nucleus of living cells.

7.2. Improvements to the instrument

The magnetic tweezers instrument that was developed is by no means finished. While it is already a very valuable piece of equipment as it is, it can be improved in many ways. The most important improvement is to reach even higher magnetic force, as this allows using smaller beads.
However, as during the experiments with 350nm beads, the bead detection was already severely lacking, using even smaller probes will also require considerable improvement to the bead detection, to still be able to follow the bead.

7.2.1. Higher force

The achieved magnetic gradient can be increased significantly. At this moment, the gradient is primarily limited by the thickness of the poles. At the current 6 µm thickness, the magnetic tweezers produces only one third of the maximum gradient that would be achieved when using 25 µm thick poles. The photo resist used to produce the current magnetic poles does not allow for such a height. However, very recently a new type of photo resist was introduced which, according to the specification, can be used for layers up to 24 µm thickness. Replacing the second resist layer in the delayed lift-off electroplating procedure by this new type should not require significant changes to the procedure. It would however allow electroplating up to the 25µm thickness that is required for the maximum magnetic gradient. Because the current electroplating conditions produce a layer that is free of stress, no problems are foreseen in plating such thick layers.

Other ways to increase the force will need to focus on the material of the poles. Using the ideal material for the poles would give a maximum improvement of 70% to the magnetic field and force. The current magnetic poles do not reach the maximum saturation magnetisation that is possible for bulk cobalt. Possible changes to the electroplating bath may improve on this. However, the highest

magnetisation possible would be reached using a cobalt-iron alloy. It is possible to plate mixtures of metals, but it is difficult because of the differences in the potentials of the metals.

At this moment, the magnetic beads are far from optimal. Typical magnetic beads that are monodisperse are composed of iron oxide dispersed through a polymer, and the resulting volume magnetisation is quite low, (~20 kA/m). The few commercially available beads that do have high volume magnetization (~ 800 kA/m) have a rather wide distribution in size and thus magnetic moment. This makes it difficult to determine the actual force the magnetic tweezers are exerting on them.
Ideally the magnetic beads would have a volume magnetization of up to 1800 kA/m combined with a small distribution in size and magnetic moment. Some companies have expressed their interest in making beads optimized for magnetic tweezers, so this problem might be solved in the future.

7.2.2. Bead detection

Developing the magnetic tweezers instrumentation we have focussed on how to exert magnetic force. Now that that has been accomplished, the bead position detection can be further improved. It was already seen that for 350nm beads the bright field detection in our present is unsatisfactory. Because the substrate containing the poles is 0.5 mm thick, the 100x objective could not be used on the inverted microscope. The best objective available for the microscope with enough working distance was a 40x objective. A long working distance objective with higher magnification would already improve the image quality considerably. However, imaging from the top might be a better solution, as the cover slip containing the cells, which is positioned on top of the magnetic poles, is thin enough that it would allow a 100x (oil immersion) objective.
Also better detection methods can be used. Bead detection techniques using fluorescence or lasertracking are more or less standard available, so implementing them should be relatively simple.

When the bead detection can be made real-time, then it is also possible to implement a feed-back system that allows the magnetic tweezers to actively hold a bead at a certain position. At that moment, the term tweezers will be genuine.

7.3. Future experiments with magnetic tweezers

The magnetic tweezers have been developed to a stage where manipulation experiments inside the nucleus of living cells can be performed. Typically the first

experiments would be to start investigating the rigidity of the chromatin, as almost nothing is known about it. Using many very small magnetic beads, one could trace the large pathways in the nucleus, by following streams of particles moving under influence of a magnetic force.
There are strong indications that chromatin condensation plays a major role in the (de)activation of genes. A more manipulative experiment could thus be to try to break apart the highly condensed inactive part of the chromatin to a more open structure, to see if genes can be activated this way. Histone lysine side chain acetylation is also associated with gene activity. One could functionalize the magnetic beads with enzymes that either acetylate or deacetylate chromatin. The probe could then be positioned at specific sites in the cell nucleus, and locally change the histone modification status.
It is also interesting to investigate the effect of compartmentalisation in the nucleus, by attaching actively transcribed DNA to a bead, and monitoring variation in transcription in different locations in the nucleus.
Our future goal is to experiment with single molecules like RNA polymerase in the nucleus of a living cell, where one measures for example the stall force of RNA polymerase. To do that however first the improvements to force and bead detection, that were previously described, should be implemented.

There are many other potential applications for the in vivo manipulation in living cells. Besides the described experiments in the nucleus, there are of course also numerous new experiments that can be performed in the cytoplasm and cell membrane. In stead of using phagocytosis as a means to insert a bead into a cell, also the process itself could be studied. It is known that the cell moves the phagosome further into the cell over time, and that the interior becomes acidic. What is not clear is whether this decrease in pH is dependent on the place of the phagosome, or the time that the bead has been in the cell. This could be investigated, by monitoring the acidity using a fluorescent marker, while using the magnetic tweezers to either move the phagosome towards the centre of the cell, or keep it next to the outer membrane.
Other possibilities could be studying the transport mechanism of the cell in all its facets, or studying so called lipid rafts inside the cell membrane. One could use the magnetic tweezers to study site specific processes in the cell by for example moving selected proteins to a specific site. One could also use a magnetic probe to spatially determine the position and volume of an organelle, by probing the free space around it.

These ideas still focus on exerting force on, and/or moving organelles. There are different ways of applying the tweezers. One could use the magnetic tweezers solely for the purpose of finding the probe. For extremely small probes, even advanced bead detection schemes like laser tracking can become insufficient.

Using the magnetic tweezers to apply a tiny vibration of a certain frequency, one could then use a lock-in amplifier tuned to that specific frequency to distinguish this vibrating particle from the background. The advantage of such a probe compared to for example single molecule fluorescence markers, is that such magnetic marker never bleaches, and thus allows for longer experiments.

If one can produce suitable probes, one can also think about site specific drug targeting, or specific biosensors. One can envision a drug containing shell around the magnetic probe, which could be photo-degradable for certain wavelengths.
Being able to move a probe around into the cell also opens the way for gold coated probes that facilitate spatially resolved enhanced optical microscopy using surface enhanced Raman or Surface Plasmon Resonance.

Summary

Living cells form a very interesting, but also very challenging research subject for biologists and biophysicists. We have come to the stage that better understanding of the functioning of the organism as a whole, requires detailed knowledge of the internal molecular processes of the cells that compose it.

The problem however, is that there are no suitable methods for doing spatially resolved measurements with molecular resolution that are fit to study these molecular interactions directly within a living cell. This thesis takes a first step towards the development of methods and instrumentation to start probing the inside of a single living cell, with the goal to eventually be able to perform single molecule experiments, inside the cell.

In chapter 1, the possible methods for applying force on a probe inside a cell are discussed. Magnetic tweezers were concluded to be optimal, because they can exert high forces, while at the same time being very selective to the probe. In the following chapters, a pair of magnetic tweezers was developed that is able to perform the required in vivo nano-manipulation.

Magnetic force on a magnetic probe is generated by a gradient in the magnetic flux density. In chapter 2, it is shown that producing such a gradient, suitable to be applied in biological experiments, requires a configuration with multiple micrometer scale poles. With such poles, the magnetic force is controllable in direction and amplitude. A maximum gradient of 30 kilo-tesla/metre should be achievable, corresponding to a magnetic force of 27 pN on an iron particle of 100nm diameter.

Such magnetic pole structure however, proved to be very difficult to produce. A novel micro machining technique ‘delayed lift-off electroplating’ had to be developed to allow production of the poles in the MESA+ clean room facility at the University of Twente. This technique, as well as the other parts of the setup, is described in chapter 3.

Characterization and calibration of the setup is described in chapter 4. A magnetic gradient of 7.5 kT/m was measured, which agrees well with the theory, when the limited height and saturation of the magnetic poles is takes into account.

This magnetic tweezers ability to perform in vivo nano-manipulation was demonstrated in chapter 5, by manipulating magnetic beads inside the cytoplasm of living cells. In this way, the viscoelastic properties of the cytoplasm of

granulocytes were measured. Because of the unique properties of the tweezers, it could be shown that the viscoelastic properties of the cell cytoplasm are not only inhomogeneous, but also highly anisotropic.

After the thesis concept was written, some additional cell experiments were performed, where a magnetic bead was injected and manipulated inside the nucleus of a HeLa cell. The resulting data was used to determine the viscoelastic properties of the chromatin interior inside the cell nucleus. To the best of our knowledge, this is the first report on in vivo nano-manipulation experiments performed *inside the nucleus of a living cell*! Therefore, although these results are preliminary, it was found prudent to include the results of these experiments in chapter 6.

Chapter 7 finished with the main conclusions and an outlook to the future.

Samenvatting

Levende cellen vormen een zeer interessant, maar ook uitdagend onderzoek onderwerp voor biologen en biofysici. We zijn in een stadium gekomen waar beter inzicht in het functioneren van het organsime als geheel, een detailleerde kennis vereist van de interne moleculaire processen van de cellen waaruit het is opgebouwd.

Het probleem is echter, dat er geen geschikte methodes zijn om direct binnen in een levende cel, metingen te doen met voldoende moleculaire resolutie. Dit proefschrift is een eerste stap tot the ontwikkeling van methoden en instrumentatie waarmee the binnenkant van een levende cel kan worden gemeten, met als uiteindelijk doel, het uitvoeren van experimenten op enkele moleculen binnen in een levende cel.

In hoofdstuk 1 worden de verschillende methoden voor het uitoefenen van een kracht op een deeltje in een cel besproken. Een magnetisch pincet(‘magnetic tweezers’) blijkt optimaal vanwege het vermogen tot het uitoefenen van een hoge kracht, terwijl deze kracht ook zeer selectief is voor dat deeltje. De volgende hoofdstukken bespreken de ontwikkeling van een magnetic pincet dat in staat is om de vereiste in vivo nanomanipulatie uit te voeren.

Een magnetische kracht op een deeltje wordt genegeert door een gradient in het magnetisch veld. Hoofdstuk 2 laat zien dat een dergelijke gradient, die ook nog geschikt is voor gebruik in biologische experimenten, een configuratie vereist van meerdere magnetische polen op micrometer schaal. Met zulke polen is de magnetische kracht controleerbaar in grootte en richting. Een maximale gradient van 30 kilo-tesla/meter zou mogelijk moeten zijn. Dit correspondeert met een magnetische kracht van 27 pN op een ijzer deeltje met een diameter van 100 nm.

Zo’n magnetische pool structuur bleek zeer moeilijk te produceren. Een nieuwe micro mechanica techniek genaamd ‘delayed lift-off electroplating’ moest worden ontwikkeld om the poles in de MESA+ cleanroom van de Universiteit Twente te produceren. Deze techniek en de overige delen van de opstelling worden beschreven in hoofdstuk 3.

Karakterisatie en calibratie van de opstelling is beschreven in hoofdstuk 4. Een magnetische gradient van 7,5 kT/m was gemeten. Dit komt overeen met de theorie wanneer de geringe hoogte en verzadigen van de polen wordt verdisconteerd.

De mogelijkheid van het magnetisch pincet om in vivo nano-manipulatie experimenten uit te voeren is gedemonstreerd in hoofdstuk 5 door magnetische bead, die zich in het cytoplasma van levende cellen bevonden, te bewegen. Op deze manier zijn de viscoelastische eigenschappen van het cytoplasma van granulocyten gemeten. Door de unieke eigenschappen van het magnetisch pincet, konden we laten zien dat the viscoelastische eigenschappen van het cel cytoplasma niet alleen inhomogeen zijn, maar ook zeer anisotroop.

Nadat het proefschrift was geschreven, zijn er nog extra cel experimenten uitgevoerd, waarbij een magnetische bolletjes geinjecteerd en gemanipuleerd zijn in de kern van een HeLa cel. De resulterende data is gebruikt om de viscoelastische eigenschappen van het chromatine binnenkant van de cel kern te bepalen. Voor zover wij weten, is dit het eerste gerapporteerde in vivo nanomanipulatie experiment *in de kern van een levende cel*. Daarom lijkt het ons terecht om deze voorlopige resultaten op te nemen in hoofdstuk 6.

Hoofdstuk 7 besluit met de algemene conclusies, en een vooruitblik naar de toekomst.

Nawoord.

Na ruim vier jaar ploeteren, is het er dan toch van gekomen. Er ligt een proefschrift met daarin de beschrijving van een bijzonder instrument en unieke resultaten.

Lange tijd zag het er niet naar uit dat we zover zouden komen. We hadden ons op volstrekt onbekend terrein begeven, en dat hebben we geweten! Zaken als calibratie, die normaal gesproken een fluitje van een cent zijn, bleken haast onneembare struikelblokken. En de eerste optimistische geluiden uit de cleanroom van: ‘Oh, dat is geen probleem, dat maak je zo!’ veranderden al snel in ‘Geen idee, laat het ons ook even weten als je het opgelost hebt…’
Na drie jaar zonder direct aanwijsbaar resultaat, was ikzelf waarschijnlijk de enige die er nog enigszins vertrouwen in had. Ik had het gevoel dat we er bijna waren, en bleef me vastklampen aan de gedachte dat dit instrument iets zou kunnen dat nergens anders op de wereld kon; namelijk binnen in kern van een levende cel metingen doen!

Gelukkig heeft mijn gevoel me niet bedrogen, want uiteindelijk bleken alle puzzel stukjes in één klap in elkaar te vallen en hadden we een werkend apparaat waarmee uiteindelijk in de laatste maanden van mijn aanstelling een paar hele mooie experimenten zijn uitgevoerd. Het is zelfs gelukt in de celkern te meten, en daar ben ik werkelijk ape trotst op!

Dat ik ondanks alle tegenslagen toch met plezier naar het werk bleef gaan, komt in het bijzonder door de prettige sfeer binnen BFT. Het voelt als een hechte familie waarbij iedereen voor een ander klaar staat, en altijd tijd voor je heeft. Jullie allemaal hebben op de een of andere manier een steentje bijgedragen aan dit proefschrift. Soms door advies, soms door iets te bouwen, maar ook gewoon door een vriendelijk woord of luisterend oor wanneer ik dat nodig had.

Ik kan jullie moeilijk allemaal opnoemen, dus ik zal het maar moeten samenvatten: Iedereen binnen BFT, heel hartelijk bedankt!!

Uiteraard zijn er ook enige personen die ik speciaal wil noemen. Allereerst natuurlijk mijn promoter Jan, en directe begeleider Hans, die zeer veel hebben bijgedragen aan het tot stand komen van die proefschrift. Daarnaast ook Vinod met zijn ongelooflijke enthousiasme, die nog die belangrijke extra maanden aanstelling heeft kunnen regelen waarin we nog zoveel extra cel experimenten konden doen.

Al die experimenten hadden echter niet kunnen plaatsvinden zonder de inspanningen van Yvonne en Kirsten. Het prepareren van de cellen en beads wordt in het proefschrift samengevat tot enkele zinnen. Daaruit maak je niet op dat tijdens de weken dat ik experimenteerde, iedere dag één van jullie de gehele ochtend full-time voor mij aan het werk was. Ondanks dat dat dikwijls op zeer ongelukkige momenten kwam, was het was nooit een probleem. Er werd altijd wel iets geregeld, zodat ik mijn cellen kreeg. Fantastisch!
Hierbij aansluitend natuurlijk ook een bedankje aan iedereen (en vooral Lili) die zijn/haar bloed heeft afgestaan, waaruit de cellen konden worden geisoleerd.

Verder nog even een speciaal bedankje aan:
Mijn afstudeer student Frans, die het fluorescentie gedeelte van de opstelling heeft ontworpen. Aufried, die zich heeft ingespannen om de ideale versterker voor mij te bouwen. En daarna minstens zo hard moest werken om het kreng te repareren wanneer er weer eens een opamp doorgebrand was. Huib van Vossen, die als vraagbaak fungeerde voor al mijn cleanroom problemen, Thijs Bolhuis voor ondersteuning en gebruik van de magnetometer van de leerstoel SMI, en Dirk Grijpma voor alle informatie en verstrekken van de biocompatibele polymeren.

En natuurlijk niet te vergeten, onze office manager Sylvia, die de spil is waar de leerstoel om draait. Zonder de ‘woman who has all the answers’ zou er niets voor elkaar komen.

Dit project was echter niet alleen een UT aangelegenheid. Het project werd in samenwerking met de Universiteit van Amsterdam uitgevoerd, waar Bea Krenn en Roel van Driel het biologische gedeelte van het project onder handen namen. We hebben een ongelooflijk plezierige samenwerking gehad, die uiterst leerzaam was. (We zijn er alleen nog nooit uitgekomen of je de grootte van eiwitten nu in nanometers of Daltons moet uitdrukken.) Jullie beiden ook heel erg bedankt!

Als laatste wil ik mijn familie bedanken voor alles wat zij al die jaren voor mij gedaan hebben. Dat is niet te omschrijven, maar ik denk dat een ieder weet wat ik bedoel. In mijn geval heeft het echter ook rechtstreeks betrekking op mijn onderzoek, aangezien ik ook op wetenschappelijk niveau goed met hen kan praten. Enige referenties komen regelrecht uit de boekenkast van mijn vader, alsmede een handig klein geel boekje, dat zijn weg langs de meeste magnetisme gebruikers in de leerstoel heeft gevonden, omdat er kort en bondig de details van de (ferro)magnetostatica werden behandeld.

Jullie allemaal, Heel hartelijk bedankt!

Anthony.